UNIVERSITÀ DEGLI STUDI DI PADOVA
Dipartimento di Fisica e Astronomia “Galileo Galilei”
PhD in Physics - XXXVI cycle

Mode-matching sensing through RF Higher-Order Modulation for Gravitational Wave detectors

Supervisor:
Prof. Giacomo Ciani
Co-Supervisor:
Prof. Marco Bazzan

Candidate:
Gabriella Chiarini

2024

Abstract

Gravitational waves (GW), predicted by Einstein's general relativity in 1916, can be described as "ripples" in space-time caused by accelerated masses. They manifest as fractional changes in spacetime geometry, known as strain h. The current generation of ground-based gravitational wave detectors, including LIGO, Virgo, and KAGRA, has achieved unprecedented sensitivity, detecting strains on the order of 10^{-21}. This remarkable precision enables the observation of extreme astrophysical events, such as the coalescence of binary systems composed of black holes and neutron stars. To further improve sensitivity and broaden the reach of gravitational wave astronomy, ongoing efforts focus on refining interferometric techniques, enhancing detector technologies, and developing innovative noise reduction strategies. In this context, it has become critical to develop new techniques for online percent-level sensing of mode-mismatch errors between the circulating laser beam and the many optical cavities constituting the interferometer; this thesis presents a proof-of-principle demonstration of a novel mode-matching sensing technique with reduced hardware requirements.

One of the primary challenges in achieving higher sensitivity is addressing quantum noise, which arises from fundamental limits imposed by quantum mechanics. This noise is due to the fluctuations in the vacuum states entering the interferometer output port and is made up of two contributions: shot noise dominating at high frequencies and radiation pressure noise at low frequencies. The first arises from the statistical fluctuations in the number of photons detected, introducing fluctuations in the phase of the light; the latter is associated with the momentum carried by photons which influences the amplitude of the light in the interferometer.

To mitigate the impact of quantum noise and improve the sensitivity of the instruments in current GW detectors the vacuum states are replaced with squeezed vacuum states. These states obey the Heisenberg Uncertainty Principle, for which reducing the phase fluctuations inevitably leads to an increase in the amplitude fluctuations, and vice versa. During the latest scientific run O3, Virgo and LIGO successfully implemented squeezing to reduce shot noise as it was the dominant noise source at high frequency. This technique is called Frequency Independent Squeezing (FIS). In the current upgrades, GW interferometers are also limited at low frequencies by radiation pressure noise. This necessitates a Frequency-Dependent Squeezing (FDS) technique, implemented using a 300m Filter Cavity (FC) slightly detuned with respect to the squeezed vacuum frequency. This detuning introduces a frequency-dependent phase shift in the squeezed vacuum state, which allows to obtain broadband reduction of quantum noise.

There are several degradation mechanisms that could lead to losses resulting in degradation of the squeezing level and, therefore, of the overall quantum noise reduction. One of the

primary factors contributing to the reduction in performance is the imperfection in mode-matching (mode-mismatch) between the fundamental mode of the optical cavity and that of the incident squeezed vacuum beam. This mismatch is characterized by differences in dimension and position of the waist, which can be represented in first-order approximation by an additional spurious higher-order mode (HOM), namely a Laguerre-Gaussian LG_{01} mode. When the cavity is locked on the fundamental mode, this HOM is reflected and carries important information on the origin of the mismatch.

To address this issue in the current and future GW detectors, like Advanced Virgo+, we introduce a novel method for sensing mode-mismatch through RF Higher Order Mode Modulation. This technique is based on a custom electro-optical lens (EOL) composed of a lithium-niobate crystal equipped with a suitable set of electrodes. The shape of the electrodes determines the ability of the object to act as a lens by exploiting the electro-optical effect. With the EOL, the laser beam is modulated generating sidebands on the LG_{01} mode. The modulation frequency is chosen to be twice the HOM spacing. In this way, when the cavity is locked, one of the sidebands resonates inside the cavity while the other is reflected together with the LG_{01} carrier. Thanks to this asymmetry, by measuring the beat signal between the carrier and sideband on a single-element photodiode, we can extract two error signals using I/Q demodulation at the sideband frequency. These signals are proportional to the real and imaginary parts of the LG_{01} mode which correspond to the waist size and waist position mismatch, respectively.

This method offers an effective approach for online sensing of mode-mismatch in the interferometer, enabling the implementation of closed-loop correction and enhancing the overall performance. The available techniques for mode-mismatch sensing are few and require a rather high number of sensors. On the other hand, this method requires minimal additional hardware, utilizing the single-element photodiode typically present for Pound-Drever-Hall (PDH) locking.

Contents

Chapter 1

Gravitational Waves: Theory and Detection

Gravitational waves (GWs) represent distortions in spacetime resulting from intense astrophysical phenomena. They can be described as “ripples” in the fabric of spacetime, carrying energy away from massive accelerating objects, such as merging black holes or neutron stars. They were initially proposed by Henri Poincaré in 1905 [1]; however, it was only in 1916 that a comprehensive understanding of GWs emerged with the formalization of Albert Einstein’s General Relativity (GR) theory [2][3].

It wasn’t until several decades later, in the 1960s, that physicists began to think about experimental methods for their detection. Pioneering work by scientists like Joseph Weber, who developed the first resonant bar detectors [4], marked the initial attempts to directly observe these elusive cosmic ripples. In the subsequent years, Rainer Weiss [5] and Robert Forward [6] played influential roles in promoting the use of interferometers as a viable method for detecting gravitational waves. Despite early optimism, the field faced numerous challenges, and it wasn’t until 1975 that the first indirect evidence for gravitational waves emerged through the precise timing of the binary pulsar PSR 1913+1, discovered by Russell Hulse and Joseph Taylor [7], for which they were awarded the Nobel Prize in 1993.

The turning point for gravitational wave astronomy occurred in 2015 with the groundbreaking detection of GW emitted by a coalescing binary black hole system by the Laser Interferometer Gravitational-Wave Observatory (LIGO) [8]. This monumental achievement, acknowledged with the 2017 Nobel Prize, not only confirmed a critical aspect of Einstein’s theory but also inaugurated a new era in astrophysics. Subsequent detections, resulting from the joint observations of LIGO and Virgo, have expanded our understanding of the cosmos, revealing insights into the nature of compact object mergers and opening new avenues for exploration.

In this chapter, an introduction to the theory of gravitational waves and their sources will be provided, followed by a discussion on interferometric detection. Additionally, an examination of the noise budget of GW interferometers, with particular emphasis on quantum noise, will form the contextual basis for this thesis work.

1.1 Introduction to Gravitational Waves

At the core of Einstein's General Theory of Relativity are the Einstein Field Equations (EFE) expressed as:

$$R_{\mu\nu} - \frac{1}{2} g_{\mu\nu} R = \frac{8\pi G}{c^4} T_{\mu\nu} \tag{1.1}$$

where $R_{\mu\nu}$ denotes the Ricci tensor, $g_{\mu\nu}$ the metric tensor, and $T_{\mu\nu}$ the energy-momentum tensor. These equations describe the fundamental relationship between the curvature of spacetime (on the left side) and the distribution of matter and energy within that spacetime (on the right side). GWs result from linearizing the EFE, revealing their properties of propagating at the speed of light and exhibiting two distinct polarization states. Moreover, as we will see in the next section, their interaction with matter allows for direct detection.

1.1.1 Linearized Theory

In the linearized theory, the metric $g_{\mu\nu}$ of the spacetime is expressed as the sum of the flat Minkowski metric $\eta_{\mu\nu}$ plus a perturbation $h_{\mu\nu}$:

$$g_{\mu\nu} = \eta_{\mu\nu} + h_{\mu\nu} \tag{1.2}$$

The magnitude of the perturbation $h_{\mu\nu}$ is assumed to be much less than unity ($|h_{\mu\nu}| \ll 1$), indicating a small deviation from the flat Minkowski metric.

By working with a slightly different description of the metric perturbation, defined as the trace-reversed perturbation, we obtain a more manageable form of the equations. We denoted it as $\bar{h}_{\mu\nu}$, which is defined as:

$$\bar{h}_{\mu\nu} = h_{\mu\nu} - \frac{1}{2} \eta_{\mu\nu} h \tag{1.3}$$

Here, h represents the trace of the metric perturbation, and $\eta_{\mu\nu}$ is the Minkowski metric.

By an appropriate choice of coordinates, we chose to work in the Lorentz gauge for which the divergence of the perturbation field is zero:

$$\partial^{\nu} \bar{h}_{\mu\nu} = 0 \tag{1.4}$$

The Einstein equations (1.1), then, can be written as:

$$\Box \bar{h}_{\mu\nu} = -\frac{16\pi G}{c^4} T_{\mu\nu} \tag{1.5}$$

where $\Box \equiv (-\frac{1}{c^2}\partial_0^2 + \nabla^2)$ is the flat spacetime wave operator (d'Alambertian operator). We want to study the solutions of the vacuum field equations, which can be achieved by setting $T_{\mu\nu} = 0$:

$$\Box \bar{h}_{\mu\nu} = 0 \tag{1.6}$$

This equation (1.6) is exactly a wave equation for the space-time perturbation $\bar{h}_{\mu\nu}$, whose solutions are a complete set of monochromatic plane waves propagating at the speed of light c:

$$\bar{h}_{\mu\nu} = \epsilon_{\mu\nu} e^{ik^\alpha x_\alpha} \tag{1.7}$$

where $\epsilon_{\mu\nu}$ is the polarization matrix and $k^\alpha = (\omega/c, \vec{k})$ is the wave vector of the plane wave. In vacuum we can simplify even more the form of the metric since the Lorentz gauge does not fix the gauge completely [9]. In particular, we can make a choice such that the trace of the perturbation $\bar{h} = 0$ and therefore $\bar{h}_{\mu\nu} = h_{\mu\nu}$. Usually, the choice is set to the transverse-traceless (TT) gauge, for which:

$$h_{0\mu} = h_{\mu 0} = 0 \qquad h_i^i = 0 \qquad \partial^j h_{ij} = 0 \tag{1.8}$$

For a plane wave which propagates along the z direction, we can write the perturbation metric as:

$$h_{\mu\nu}^{TT}(t, z) = (h_+ \epsilon_{\mu\nu}^+ + h_\times \epsilon_{\mu\nu}^\times) e^{i(\omega t + kz)} \tag{1.9}$$

where h_+ and $h_\times$ are the amplitudes of the plus ϵ^+ and cross $\epsilon^\times$ polarization of the wave, which are written as:

$$\epsilon^+ = \begin{pmatrix} 0 & 0 & 0 & 0 \\ 0 & 1 & 0 & 0 \\ 0 & 0 & -1 & 0 \\ 0 & 0 & 0 & 0 \end{pmatrix} \qquad \epsilon^\times = \begin{pmatrix} 0 & 0 & 0 & 0 \\ 0 & 0 & 1 & 0 \\ 0 & 1 & 0 & 0 \\ 0 & 0 & 0 & 0 \end{pmatrix} \tag{1.10}$$

Figure 1.1 illustrates how the plus- and cross-polarizations impact a ring of test masses in free falling, i.e. free from any force of non-gravitational origin. It demonstrates an alternating pattern of squeezing and stretching of the ring in orthogonal directions, with a 45-degree rotation between the two polarizations. If the proper diameter of the unperturbed ring is L, the GW strain h is linked to the deformation of the ring δL as[9]:

$$h = \frac{2\delta L}{L} \tag{1.11}$$

Ground-based interferometric GW detectors work by measuring this differential distortion between orthogonal directions.

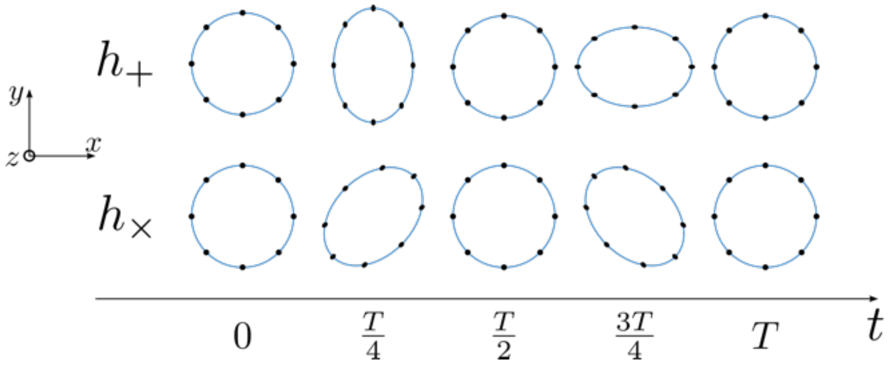

Figure 1.1: Test masses on a ring: response of free falling masses to the passage of a gravitational wave propagating perpendicularly to the ring. The upper part shows the “plus” polarization effect, while the lower panel shows the “cross” polarization effect.

1.1.2 Sources of GWs

Gravitational waves are generated by the acceleration of massive objects, as predicted by General Relativity. However, only mass distributions that change in a non-spherically symmetric way have the potential to generate gravitational waves. This is because GWs are generated by a change of the quadrupole moment in the mass distribution [9]. A spherically symmetric mass distribution possesses a zero quadrupole moment, resulting in the absence of net gravitational wave emission. The most detectable and significant GWs that we can measure are produced by extreme and violent astrophysical events. In general, the detection of GWs is a challenging task because these waves interact very weakly with matter, making their effects incredibly subtle. Consequently, events involving large masses and strong accelerations are required in order to produce waves with amplitudes that are detectable by current instruments.

Examples of extreme astrophysical events that can generate significant gravitational waves with a frequency range of a few tens of Hz to several kHz, detectable by ground-based interferometers, include:

Compact Binary Coalescences: This source consists of two compact and highly massive astrophysical objects orbiting around a common center of mass, creating a binary system. The orbital motion of the compact binary system results in the emission of GWs, which carry away energy and angular momentum, causing the binary to gradually spiral inward. The evolution of a compact binary system undergoing GW emission and eventual coalescence is generally described in three distinct phases: the inspiral, the merger and the ring-down. In the inspiral phase, the two compact objects orbit each other in a gradually tightening spiral. The emission of gravitational waves during this phase causes the binary system to lose energy, leading to a decrease in the orbital separation. As the inspiral continues, the separation between the compact objects diminishes until they eventually merge into a single, more massive object. The merger phase is marked by extreme gravitational forces and rapid changes in spacetime. After the merger ringdown,

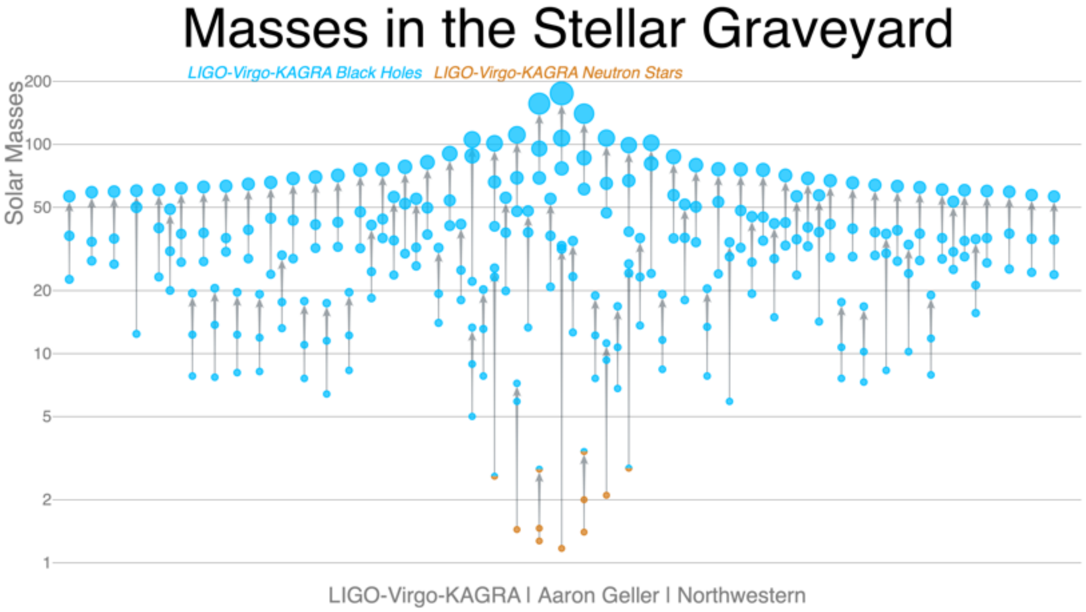

Figure 1.2: Binary systems detected with ground-based interferometric GW detectors. This version contains all events up to the third observing run (O3). (Credit: LIGO-Virgo / Aaron Geller / Northwestern University)

the remnant object undergoes oscillations and settles into a more stable configuration. These oscillations produce gravitational waves with a characteristic decay pattern [10]. Compact binaries detected so far are classified into three main categories based on the composition of the compact objects involved: Binary Black Holes (BBH), Binary Neutron Star (BNS) and Neutron Star-Black Hole Binary (NSBH).

Continuous Gravitational Waves: In contrast to the transient signals associated with compact binary coalescences, Continuous Gravitational Waves are persistent and nearly periodic signals. These kinds of GWs are generated by rotating massive objects, like neutron stars, with asymmetric mass distributions. These sources tend to produce weaker signals compared to transient events like binary mergers. However, the continuous nature of the signal allows for longer observation times, which can increase the signal-to-noise ratio (SNR) and improve the chances of detection [11]. In particular, rotating neutron stars, if they are pulsars (emitting electromagnetic radiation in addition to GWs), provide a unique opportunity for multi-messenger astronomy. Pulsars emit beams of radiation that are observable as periodic pulses when these beams cross our line of sight. If a pulsar is also emitting GWs due to its rotation, the combined use of GW detectors and telescopes observing the electromagnetic pulses can provide complementary information [12].

Burst Sources: These sources are usually unmodeled signals, for which we do not have a precise theoretical model predicting the waveform. Short-duration signals, such as those from supernovae or other cataclysmic events, fall into this category. These events involve the explosive collapse of a massive star, and the resulting gravitational wave signal can be a brief and intense burst [13]. However, modeling gravitational waves from supernovae is challenging due to the complex and non-linear nature of the process.

Up to now the GW detectors observed in three observation runs (O1-O2-O3) a total of 90 GW transients associated with binary systems of black holes and neutron stars. All of these detections with the corresponding initial and final masses are illustrated in Figure 1.2. Particularly relevant is the first detection, GW150914 [8], observed by the American interferometers LIGO on the 14th of September 2015. The signal was produced by the merger of two black holes, approximately 1.3 billion light-years away from Earth. The event involved black holes with masses around 29 and 36 times that of the Sun. Other significant events are GW170814 [14] and GW170817 [15]. The first one was the first joint detection with the European observatory Virgo, observed on the 14th August 2017 and it was a signal from a BBH system of initial masses of approximately 30.5 and 25 times the mass of the Sun. Due to the different antenna patterns of LIGO and Virgo, i.e. the sensitivity to GWs of different polarization coming from different directions in the sky, this detection allowed for the first time the study of the polarization of the detected GW. Moreover, the joint observation of the same event by multiple detectors allowed to triangulate the source position more accurately, narrowing down the region of the sky where the event occurred. These two reasons showcased the advantages of a network of detectors working together. The second one, observed on the 17th August 2017, marked the first detection of GWs from the merger of two neutron stars with the component masses being between 0.86 and 2.26 Solar masses and the first and only multimessenger observation to date. Unlike the previous detections involving black holes, this event had observable electromagnetic counterparts, including gamma-ray bursts and optical signals, allowing scientists to perform multi-messenger astronomy.

1.2 Gravitational Wave Detectors

Ground-based GW detectors use the principle of interferometry. Their design is based on a kilometer-scale Michelson interferometer, with an L-shaped configuration as shown in Figure 1.3. By operating in the dark fringe configuration, if the lengths of the arms remain unperturbed we observe destructive interference, that is the recombined beams cancel each other out at the photodiode. However, if a gravitational wave distorts spacetime, causing the arms to change in length, the interference condition at the detector changes. Currently, the network of ground-based GW observatories includes Virgo in Italy with 3km arms, GEO600 in Germany with 600m arms, LIGO Livingston and LIGO Hanford in the USA, each with 4km arms, and KAGRA with 3km arms, situated underground in Japan.

1.2.1 Michelson Interferometer

A Michelson interferometer is an optical instrument used to measure variations in the travel time of light within its arms. The basic configuration, shown in Figure 1.3, involves a laser beam directed to a beam splitter (BS), which divides the beam equally into two perpendicular paths known as arms. Mirrors positioned at the ends of these paths reflect the light back towards the BS, where the two beams recombine. A portion of the recombined beam is directed to a photodetector (PD), often labeled as the asymmetric or dark port, while the remaining part returns to the laser source, commonly referred to as the symmetric port. The amount of light allocated to each port, whether it is the asymmetric or symmetric one, varies with the interferometer's working point.

If L_x and L_y are the lengths of the arms, with x and y oriented as in Figure 1.3, then the electric field at the photodetector can be written as (see [9] for more details):

$$E_{out} = \frac{1}{2} E_{in} e^{-i\omega t} \left(e^{2ikL_y} - e^{2ikL_x} \right) \tag{1.12}$$

where E_{in} is the electric field amplitude of the laser input, ω is the frequency of the laser and $k = \omega/c$ is the wavenumber. We define the average arm length L and the average unperturbed arm length difference δL as:

$$L = \frac{L_x + L_y}{2} \tag{1.13}$$

$$\delta L = \frac{L_x - L_y}{2} \tag{1.14}$$

then we can rewrite equation (1.12) as:

$$E_{out} = -iE_{in} e^{-i\omega t + 2ikL} \sin\left(2k\delta L\right) \tag{1.15}$$

from which we obtain that the output power P_{out} at the PD of a Michelson interferometer can be written as:

$$P_{out} = P_{in} \left(\sin^2\left(\phi\right) \right) \tag{1.16}$$

where $\phi = 2k\delta L$ and $P_{in} = |E_{in}|^2$. Equation (1.16) reveals that changes in the differential length of the arms correspond to variations in the output power.

In the presence of a GW, the phase ϕ is the sum of a static phase ϕ_0 dependent only on the unperturbed difference length δL and a phase $\phi_{GW}(t)$ due to the perturbation induced by the GW. Suppose the signal coming from the z direction has a strain $h(t)$ and the ''+' polarization (the axes are as in Figure 1.3). Then, the arms will experience a length variation in phase opposition as:

$$\delta L_x(t) = -\delta L_y(t) = \frac{1}{2} L h(t) \tag{1.17}$$

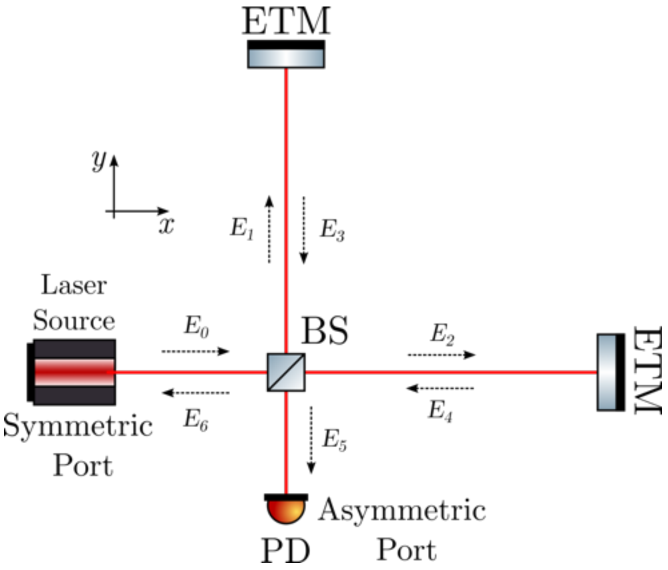

Figure 1.3: Schematic representation of a Michelson interferometer. The input beam is split by a BS into two orthogonal arms. The mirrors (end test mass, ETM) at the end of each arm reflect back the beams to recombine at the BS. The result from the recombination is read by a photodetector (PD) on the asymmetric port. In the figure, E_{in} corresponds to E_0 and E_{out} to E_5

Therefore, we can write the total phase experienced by the beam inside the interferometer as:

$$\phi(t) = \phi_0 + \phi_{GW} = 2k\delta L + kLh(t) \tag{1.18}$$

This means that the output power in equation (1.16) at the photodetector is modulated by the GW signal as:

$$P_{out} = P_{in} \left(\sin^2 \left(\phi_0 + \phi_{GW} \right) \right) \tag{1.19}$$

In practice, δL is set to be macroscopically different from zero for needs related to the control of the interferometer; at the same time, it is microscopically tuned to make the output power almost zero, working in an operating point slightly shifted off the so-called *dark fringe*. In this case, a certain portion of the light is directed to the asymmetric port and serves as a local oscillator. In this configuration, called DC-readout [16], and assuming that the variation in the arm lengths due to the GW is much smaller than the wavelength $h(t)L/\lambda \ll 1$, the output power is linear in $h(t)$ as:

$$P_{out}^{DC} \sim P_{in}\phi_0 kLh(t) \tag{1.20}$$

This last equation tells us that the signal read from the PD increases with the input power, the GW amplitude and the length of the arms of the interferometers.

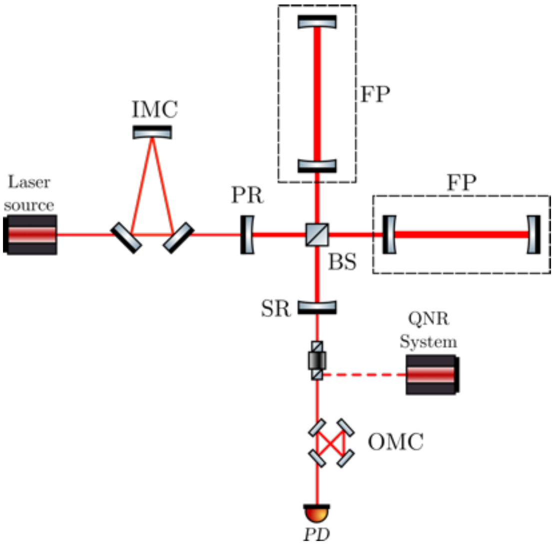

Figure 1.4: Optical scheme of an advanced GW detector. With respect to the simple Michelson interferometer, FP cavities are installed in the arms in order to increase the optical path length (in the black dashed boxes). Other expedients to improve the sensitivity of the instrument are the input and output mode cleaners (IMC, OMC), and the power and signal recycling mirrors (PR, SR). The acronym QNR stands for Quantum Noise Reduction, which we will see in the next sections.

1.2.2 Real GW Interferometers

As shown in equation (1.20), one of the parameters that can be changed to increase the output power, and therefore the detector sensitivity, is the length of the interferometer arms. To extend the arm length without physically extending the baseline of the interferometer which is already kilometric-scaled (3km for Virgo, and 4km for LIGO), GW detectors use Fabry-Pérot (FP) arm cavities. In these cavities, composed of two highly reflective mirrors, the laser beam bounces back and forth increasing the path length experienced by the light. More details on FP cavities are explained in section 2.2.

The other parameter that increases the detector sensitivity is the input power. Since the interferometer operates near the dark fringe condition, the light is directed back toward the laser source and does not reach the photodetector. By placing a mirror, called Power Recycling (PR) mirror, between the BS and the laser we are able to reinject it back inside the interferometer, increasing the power circulating in the arms and improving the sensitivity. In addition, by analogy to the PR, another mirror, called Signal Recycling (SR) mirror, is placed between the BS and the PD. The SR is placed at a specific location to modify the interferometer's response to gravitational wave signals at certain frequencies. When both the PR and the SR mirrors are used, the setup is referred to as a dual-recycling configuration.

Finally, two important optical elements used to improve the overall sensitivity of the detector, are the input and output mode cleaners (IMC, OMC), to improve the quality of the input and output beam, respectively.

The overall configuration is called Dual Recycled Fabry-Pérot Michelson interferometer and is presented in Figure 1.4.

1.3 Advanced Virgo Plus: Noise Budget

Despite the sophistication of modern large-scale laser interferometers, the detection of gravitational waves of typical amplitude of 10^{-21} or less is still a noise-dominated measurement at the limit of the instrument's sensitivity. Therefore it is of primary importance to have a detailed analysis and allocation of the various sources of noise that can affect the measurements. This is summarized in the noise budget of the interferometer, which specifies the final sensitivity of the instrument at different frequencies of the GW, in terms of the total noise amplitude spectral density h (i.e. the "fictitious" GW signal amplitude that would be needed to produce a signal equivalent to the measured noise). For Advanced Virgo Plus, which is the name for the Virgo upgrade in the current observation run O4, the predicted sensitivity is shown in Figure 1.5. This figure shows the different kinds of noises that form the sensitivity curve (black curve). In the following, we will give a brief explanation of the main contributions.

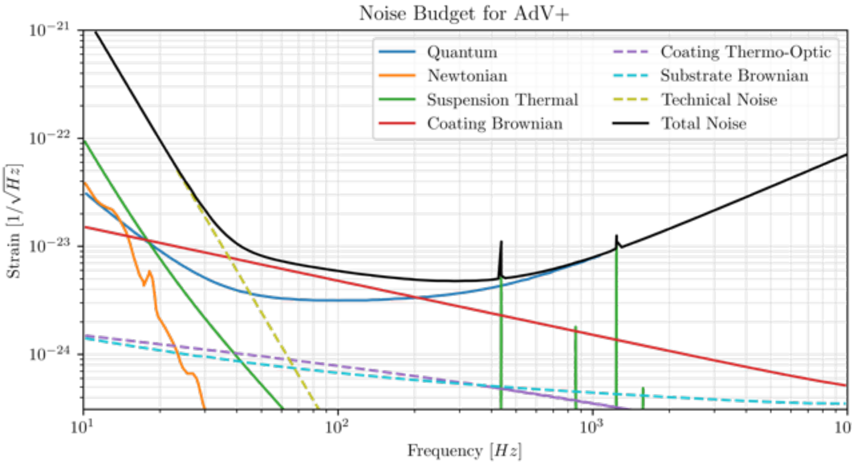

Figure 1.5: Noise Budget for AdV+ [17]. The black curve represents the predicted sensitivity during O4, while the other colored curves are the different noise contributions.

Quantum Noise: Quantum noise arises from the quantum nature of light. It is made up of two components, shot noise (SN) and radiation pressure noise (RPN). In particular, SN can be described as a photon counting noise. The arrival of photons at a photodetector is subject to statistical fluctuations, in particular, it is described by a Poissonian distribution. For a Michelson interferometer, the SN amplitude spectral density strain is inversely proportional to the length L of the interferometer and to the square root of the power P in the interferometer arms [18]:

$$h_{sn} = \frac{1}{L}\sqrt{\frac{\hbar c \lambda}{2\pi P}} \tag{1.21}$$

where $\hbar$ is the Planck's constant, c is the speed of light and λ is the laser wavelength. RPN, on the other hand, is a back-action noise caused by the random motion of the mirrors. The photons in the laser beam carry momentum, and when they strike the mirrors, they exert a force known as radiation pressure. Since the number of photons arriving at the mirrors is subject to statistical fluctuations, the force exerted by these photons and, consequently, the radiation pressure on the mirrors, experiences also random fluctuations, generating the RPN. Its spectrum is proportional to the square root of the power in the arms P and inversely proportional to the length L, the square of the frequency f and the mass M of the mirror:

$$h_{rpn} = \frac{1}{\pi M f^2 L}\sqrt{\frac{\hbar P}{2\pi c \lambda}} \tag{1.22}$$

Equations (1.21) and (1.22) hold only for a simple Michelson interferometer. In dual-recycling Fabry Pérot GW detectors, these equations have a more complex frequency response [19]. However, for what concerns this discussion, we can use the simplified version.

Quantum noise is defined as the sum of the shot noise and radiation pressure noise which, in terms of amplitude spectral densities, can be written as:

$$h_{qn} = \sqrt{h_{sn}^2 + h_{rpn}^2} \tag{1.23}$$

From equations (1.21) it is straightforward to notice that, once the length L is fixed, to reduce the SN we can increase the input power. However, from equation (1.22) we obtain that this would increase the RPN. This means that we cannot reduce both noises at the same time. At each frequency, it is possible to find for which power the sum of noises is minimized. The locus of points of this minima forms a theoretical curve called the *standard quantum limit* (SQL) shown in Figure 1.6 and defined as:

$$h_{sql} = \frac{1}{\pi L f}\sqrt{\frac{\hbar}{M}} \tag{1.24}$$

In current GW detectors, quantum noise is reduced through a technique called *quantum vacuum squeezing*. It is worth noting that the quantum noise level reported in Figure 1.5 includes a predicted 6 dB reduction of quantum noise over the entire interferometer bandwidth.

In the next section, we will provide an introduction to this technique, contextualizing the objective of this thesis work within the realm of gravitational wave interferometers.

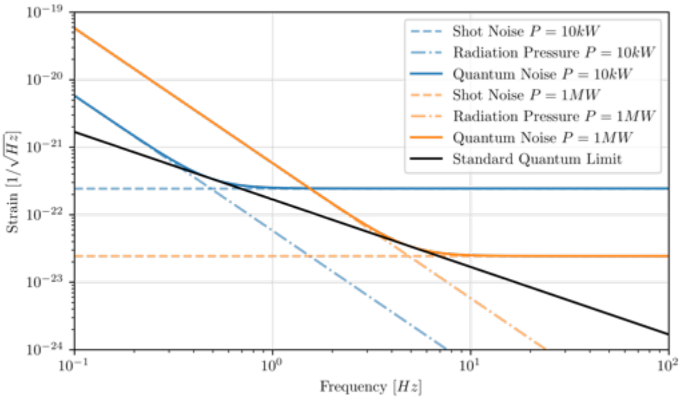

Figure 1.6: SQL (black) and quantum noise contribution for a simple Michelson interferometer, featuring 3km arm length and 42 kg test masses, for low (blue) and high (orange) circulating power.

Seismic Noise: This noise arises from ground vibrations and movements caused by seismic activity, human activities, or environmental factors. These contributions shake the suspension mechanisms and eventually the mirrors. The typical spectrum has the form of [20]:

$$h_{seis}(f) \simeq A \left(\frac{1Hz}{f}\right)^2 \tag{1.25}$$

where, for example in Virgo located in Italy (Cascina, Pi), $A \sim 10^{-7} m/\sqrt{Hz}$ in a range of 10mHz - 10kHz [21]. Therefore GW interferometers adopt multistage filters made by a chain of pendula to filter out the noise at the level of the mirrors.

Newtonian Noise: Newtonian noise, also known as gravity gradient noise, is a low-frequency noise due to time-varying gravitational forces caused by the motion of masses in the vicinity of the interferometer, such as micro-seismic noise or atmospheric turbulence. This noise cannot be attenuated since the gravitational force cannot be screened. It still doesn't limit the current GW detectors; however, for the third generation of interferometers, it will be more relevant [22].

Thermal Noise: As the fluctuations-dissipation theorem states, any system that experiences dissipation will also experience fluctuations in its position [23]. This means that thermal energy induces vibrations in both the mirrors and the suspensions which generate a noise called thermal noise [24][25].

Technical Noise: There are also other, less fundamental sources of noise that have to be kept under control. For example, the laser beam must travel in an ultra-high vacuum pipe in order to keep the noise induced by fluctuations in the index of refraction below the design sensitivity. Other examples are phase noise generated by diffuse light scattering from mirror defects, and control noise, which originates from the systems used to keep the interferometer aligned and on the correct working point.

1.4 Quantum Noise

In 1980 C. M. Caves demonstrated [26] that quantum noise has nothing to do with the input power fluctuations, and instead arises from the coupling between the circulating field and the vacuum fluctuations entering the asymmetric port of the interferometers. In another paper [27] he proposed a method to reduce SN while increasing RPN, and vice versa. This technique involves injecting *squeezed* vacuum state into the asymmetric port.

1.4.1 Squeezed States

From the quantization of the electromagnetic field, we can write the quantum electric field operator of a laser beam at frequency ω and propagating in the z direction, with the quadrature operators $\hat{X}_1$ and $\hat{X}_2$:

$$\hat{E}(z,t) = E_0 \sin(kz) \left(\hat{X}_1 \cos(\omega t) + \hat{X}_2 \sin(\omega t) \right) \tag{1.26}$$

where $E_0 = 1/2\hbar\omega$ is the energy of the vacuum state, which is the state with the lowest possible energy and corresponds to a zero mean number of photons. The operators correspond to the amplitude ($\hat{X}_1$) and phase ($\hat{X}_2$) quadratures and can be written in terms of annihilation $\hat{a}$ and creation $\hat{a}^\dagger$ operators as:

$$\hat{X}_1 = (\hat{a} + \hat{a}^\dagger) \qquad \hat{X}_2 = i(\hat{a}^\dagger - \hat{a}) \tag{1.27}$$

For the Heisenberg principle, their uncertainties follow:

$$(\Delta X_1)^2 (\Delta X_2)^2 \geq 1 \tag{1.28}$$

This means it is not possible to measure both quadratures with precision simultaneously. Those states that reach the minimum in equation (1.28) are the so-called minimum uncertainty states. Both coherent and squeezed states fall into this category. However, there is a distinction in how the uncertainties are distributed between the two quadratures: in coherent states, the uncertainty is equally distributed between the two quadratures, while in squeezed states, one quadrature has reduced uncertainty at the expense of increased uncertainty in the conjugate quadrature. This is shown using the quadrature picture in Figure 1.7. A squeezed state can be generated starting from a coherent state by applying the unity squeezing operator defined as

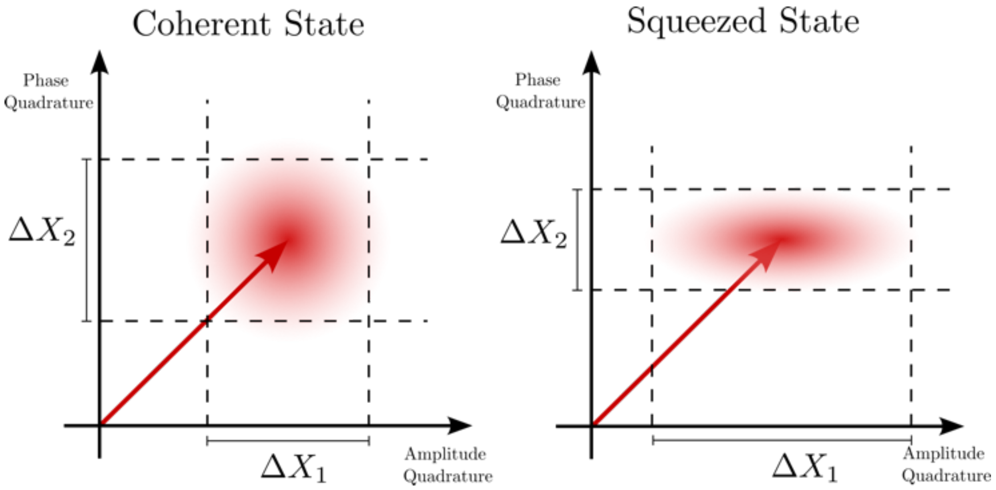

Figure 1.7: Quadrature picture of coherent states (left) and squeezed states (right). The red arrow indicates the average classical field, while the cloudy ball indicates the probability distribution of the amplitude and phase quadratures of the laser beam photons. The coherent state has the same uncertainty in the two quadratures therefore represented as a circle. In contrast, the squeezed state has different error values on the two axes, which generates in this representation the *squeezing ellipse*.

(see [28] for a more detailed analysis):

$$\hat{S}(\xi) = \exp\left\{\left[\frac{1}{2}(\xi^* \hat{a}^2 - \xi \hat{a}^{\dagger 2})\right]\right\} \tag{1.29}$$

where ξ is the *squeezing complex parameter* and is defined as:

$$\xi = re^{2i\theta} \tag{1.30}$$

with r being the squeezing amplitude and θ the squeezing phase. The effect of the squeezing operator on the two orthogonal quadratures $\hat{X}_1$ and $\hat{X}_1$, in the particular case in which one of them is aligned with the squeezing angle, for example with $\hat{X}_1$, yield the uncertainty values:

$$\Delta X_1 = V_- = e^{-2r} \qquad \Delta X_2 = V_+ = e^{2r} \tag{1.31}$$

From this equation, we see that the variance on the $\hat{X}_1$ quadrature is squeezed by a factor e^{-2r}, while the other is antisqueezed by a factor e^{2r}. Usually, the squeezing factor is expressed in decibels as:

$$R_\pm[dB] = 20 \log_{10}(R_\pm) \tag{1.32}$$

where $R_\pm$ are the *squeezing ratios* between the squeezed/antisqueezed quadrature uncertainty and the vacuums state uncertainty, defined as:

$$R_\pm = \sqrt{\frac{V_\pm}{V_{vac}}} = e^{\pm r} \tag{1.33}$$

As outlined at the start of the section, quantum noise stems from vacuum fluctuations entering the asymmetric port of interferometers. These fluctuations are described by vacuum states, the lowest energy states of the electric field, where the mean amplitude is zero, representing the absence of average photons but the variance in the two quadratures is different from zero and obeys equation (1.28). Therefore, it becomes crucial to focus on squeezing these vacuum states to manipulate quantum noise effectively. In the visual representation (see Figure 1.7), this corresponds to a cloudy ball centered at the origin.

In general, the most successful method to physically generate these states is based on a nonlinear process, called Optical Parametric Amplification [29]. This approach can generate phase-sensitive amplification, where the quantum state undergoes either de-amplification or amplification based on its phase. This leads to a decrease in fluctuation in one quadrature and an increase in the other, generating squeezed states.

1.4.2 Squeezing Effect On Sensitivity

The quantum noise amplitude spectral density for a Michelson interferometer in the presence of vacuum squeezing becomes [28]:

$$h_{sqz} = \frac{h_{sql}}{\sqrt{2}} \left(\frac{1}{K_{Mi}} + K_{Mi} \right)^{1/2} \cdot \left[\cosh(2r) - \cos(2\theta + 2\Phi) \sinh(2r) \right]^{1/2} \tag{1.34}$$

where $K_{Mi} = P/(Mc\lambda\pi f^2)$ represents the response of a Michelson to the quantum noise, with M being the mirror mass, λ the laser wavelength, and f the gravitational wave frequency, and the angle $\Phi = \text{arccot}(K_{Mi})$ [30]. In the top panel of Figure 1.8 the strain sensitivity of quantum noise is shown for a squeezing level of 10dB and different values of the squeezing angle θ. Injecting amplitude-squeezed states ($\theta = 0$) means reducing noise at low frequency (RPN) at the expense of the noise at high frequency (SN). The opposite happens with phase-squeezed states ($\theta = -\pi/2$). Moreover, it is possible to reach sensitivity below the SQL, however only in a narrow frequency region. For example, in Figure 1.8 this is shown for $\theta = -\pi/4$. This technique is called Frequency Independent Squeezing since the squeezing ellipse angle is fixed. It has been applied during O3 to both LIGO and Virgo to reduce SN in the upper half of the detection band, where it was the dominating noise; on the contrary, the increase in RPN at lower frequency was inconsequential, owing to other noise sources being dominant. Further reduction to other noise sources is making quantum noise more and more relevant in the whole detection band, therefore to mitigate quantum noise across the entire detection band a technique to generate frequency-dependent squeezing angles is required. This method is called Frequency Dependent Squeezing (FDS) and its effect on the strain sensitivity is shown in the bottom plot of Figure 1.8. From equation (1.34), we see that the optimal value for the angle θ as a function of the

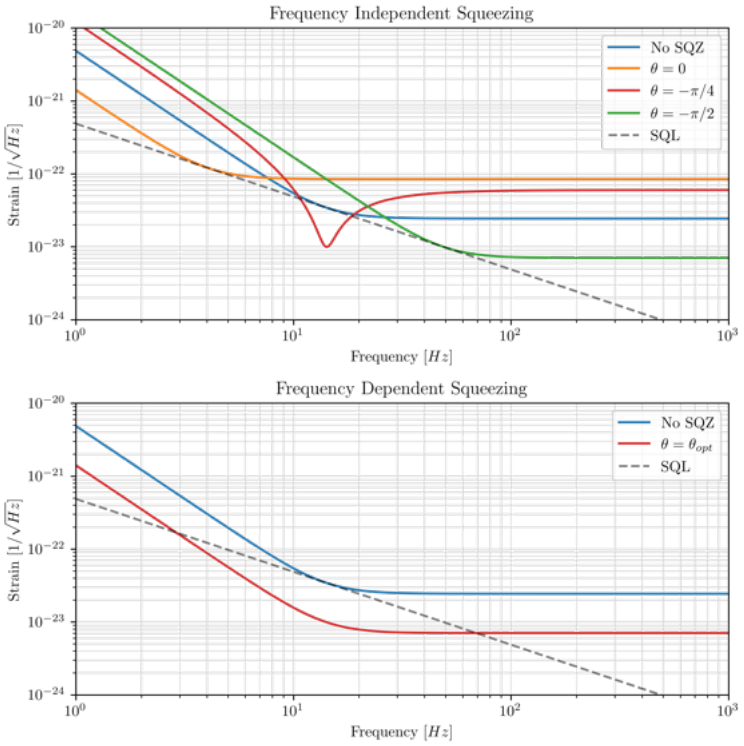

Figure 1.8: Sensitivity of a Michelson interferometer with 10dB injected squeezing at different values of θ. Top: Frequency Independent Squeezing, injecting an amplitude squeezed state ($\theta = 0$) reduces radiation pressure noise but increases shot noise. Conversely, injecting a phase squeezed state ($\theta = -\pi/2$) reduces shot noise at the expense of radiation pressure noise. Overcoming the Standard Quantum Limit (SQL) in a limited frequency range is achievable by selecting an angle $\theta = -\pi/4$. However, this choice amplifies quantum noise in other frequency ranges. Bottom: Frequency Dependent Squeezing, the squeezing angle varies with frequency, evolving from $\theta = 0$ at low frequencies to $\theta = -\pi/2$ at high frequencies to achieve broadband reduction.

frequency is $\theta_{opt} = -\operatorname{arccot}(K_{Mi})$ [30]. In this case, the spectral density becomes:

$$h_{sqz}^{FDS} = \frac{h_{sql}}{2}\sqrt{2}\left(\frac{1}{K_{Mi}} + K_{Mi}\right)^{1/2} e^{-2r} \tag{1.35}$$

To achieve the dependence on the frequency, both LIGO and Virgo use a so-called Filter Cavity (FC), a detuned FP optical cavity, $\sim$ 300m long. The frequency-independent squeezed vacuum field is reflected by the FC, thereby acquiring a frequency dependence [30] dependent on its offset from the resonant frequency of the cavity. We can describe squeezed vacuum states through sidebands along the frequency spectrum. An important characteristic of the squeezed state is that its sidebands exhibit correlations depending on the type of squeezing (phase or amplitude); the angle of the squeezing ellipse depends on the relative phase between the sidebands. By detuning the FC, the sidebands at frequencies Ω far away from the resonance of the FC, ω_{fc}, will experience a $\pm 180°$ of phase shift, depending if $\Omega \gg \omega_{fc}$ or $\Omega \ll \omega_{fc}$. For those sidebands near ω_{fc} we obtain a phase shift which gradually transitions from $-180°$ to $+180°$ with the $0°$

phase shift at $\Omega = \omega_{fc}$. Consequently, this region undergoes a rotation in the orientation of the squeezing ellipse depending on the frequency, as shown in Figure 1.9.

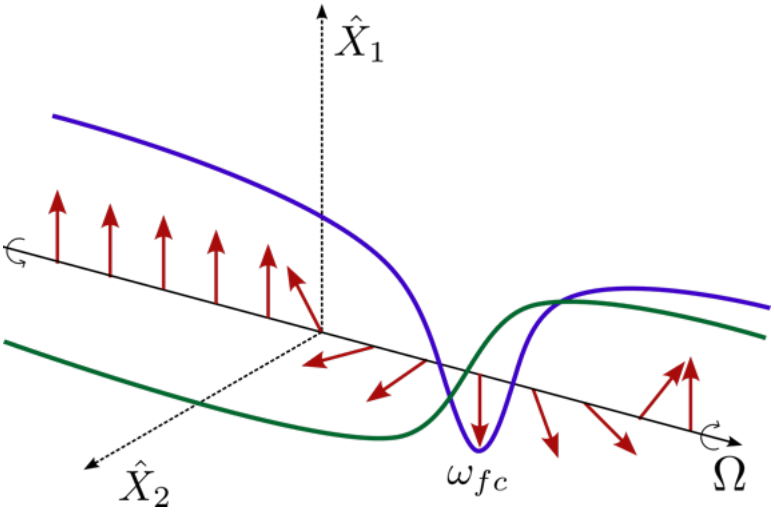

Figure 1.9: Behavior of the sidebands near and far away the resonance frequency ω_{fc} of the FC. The sidebands are represented as arrows at different frequencies Ω. When reflected from the detuned cavity, they acquire a phase shift depending on how near they are to ω_{fc}. For $\Omega \gg \omega_{fc}$ or $\Omega \ll \omega_{fc}$ they acquire a ±180° phase. Near the FC resonance, the phase shift gradually changes from −180° to +180°. The phase shift is 0° for the sidebands at frequency $\Omega = \omega_{fc}$ [31].

1.4.3 Impact of losses and role of mode mismatch

One of the main degradation mechanisms of the squeezing level, and therefore of quantum noise reduction, is optical losses. This type of degradation can be represented as a beam splitter (BS), an optical element that splits a single input beam into two outputs [32]. It can also be used to recombine two beams to obtain two outputs. The relationship between the input and output beams can be described through a matrix where the entries are the reflectance r and transmittance t of the BS:

$$\begin{pmatrix} \hat{c} \\ \hat{d} \end{pmatrix} = \begin{pmatrix} r & -t \\ t & r \end{pmatrix} \begin{pmatrix} \hat{a} \\ \hat{b} \end{pmatrix} \tag{1.36}$$

If the input fields $\hat{a}$ and $\hat{b}$ are the squeezed state $|\xi\rangle$ and the vacuum state $|0\rangle$, respectively, as shown in Figure 1.10, we obtain at the outputs $\hat{b}$ and $\hat{c}$ two squeezed states which have lost part of their squeezing level. Suppose the power reflectivity of the BS represents the power loss l. Then, we can write the output field as:

$$\hat{d} = \hat{a}\sqrt{1-l} + \hat{b}\sqrt{l} \tag{1.37}$$

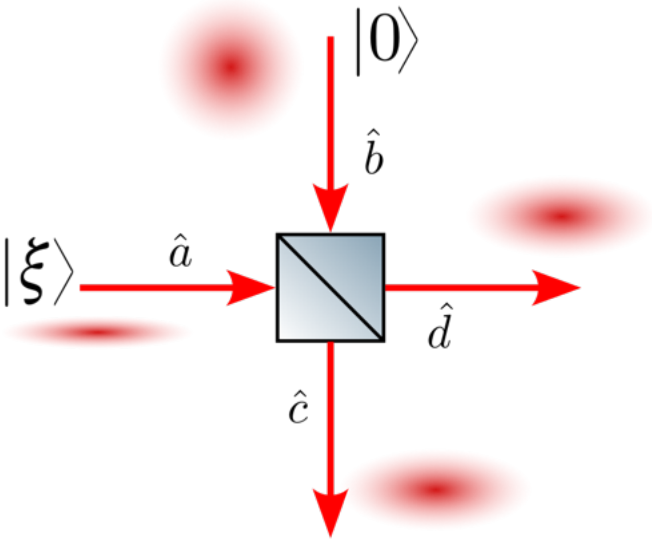

Figure 1.10: Schematic representation of the beam splitter model for optical losses. The squeezed state $|\xi\rangle$ recombines with a coherent state $|0\rangle$ which degrades the squeezing level.

Assuming uncorrelated fluctuations between $\hat{a}$ and $\hat{b}$, we can write the variance of the quadrature of this output field as:

$$\Delta X_d^l = (1-l)(\Delta X_a)^2 + l(\Delta X_b)^2 \tag{1.38}$$

where $\Delta X_a = V_\pm$ and $\Delta X_b = V_{vac}$ as defined in section 1.4.1. This leads to a degradation of the squeezing ratio of:

$$R_\pm^l = (1-l)R_\pm + l \tag{1.39}$$

From this equation, it is possible to note that due to the additivity of l, for high level of squeezing even small losses significantly compromise R_- while having little impact on R_+.

One of the factors contributing to the optical losses is the imperfection in mode-matching (mode mismatch) between the fundamental mode of an optical cavity and that of the incident laser beam. Mode mismatch is attributed to differences in waist size and position. If the input beam does not overlap completely with the cavity supported beam, then part of the amplitude does not enter yielding optical loss. In instances where the squeezed beam is not appropriately mode-matched to the FC, only a portion of it acquires the necessary phase dispersion for the FC-based FDS. Figure 1.11 shows the squeezing degradation budget for the FC, where it is possible to see how the mode mismatch (blue curve) can highly degrade the squeezing level, especially at low frequency. Moreover, mode-mismatch could cause even more complex mechanisms such as coupling between squeezing and anti-squeezing [33]. In particular, when the squeezed beam is not appropriately mode-matched to the filter cavity, a portion of the squeezed mode becomes coupled into higher-order modes. These modes undergo different phase evolutions compared to the fundamental mode, due to differences in their Gouy phases. If this beam is subsequently mismatched to another cavity, it results in an additional mixing effect, which can couple some anti-squeezing from higher order modes, now arbitrarily rotated, back into the fundamental mode. In the worst-case scenario, the coupling with anti-squeezing can lead to a status even worse than the vacuum state. For these reasons, reducing mode-mismatch between the squeezed beam and the filter cavity and between the filter cavity reflected field and the interferometer is fundamental.

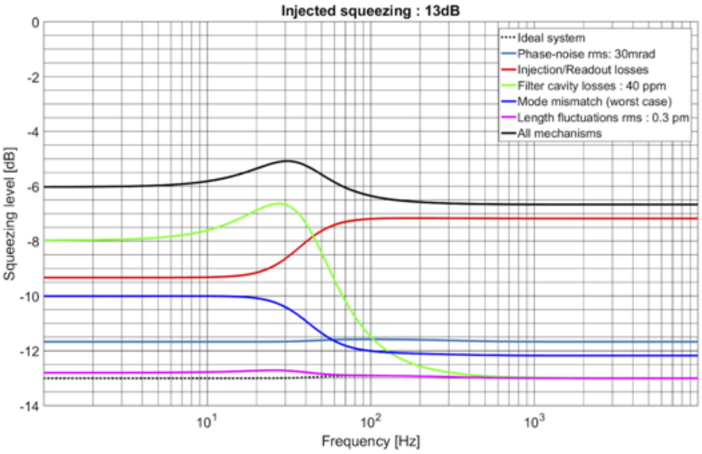

Figure 1.11: Plot of the different contributions for squeezing degradation, assuming 13 dB of injected squeezing, 40W of input power and the O4 loss budget for 285m long Filter Cavity [17].

Currently, there are relatively few methods proposed for sensing mode mismatch. This limited number can be attributed to the fact that, before the implementation of squeezing, we weren't as concerned with losses due to mismatch, and as a result, the development of online sensing techniques in this regard has been modest. Some of them include heterodyne detection with bullseye photodiodes [34], single sideband generation through an optical cavity [35], and the use of a mode converter combined with quadrant photodiodes [36]. However, these approaches often demand a significant number of sensors. In this thesis, we will present the initial successful outcomes of a method that employs only one single-element photodiode and that relies on RF modulation of the first Laguerre-Gauss higher-order mode by using a lensing element called Electro-Optical Lens. This approach marks a significant advancement in addressing the complexities associated with mode-mismatch sensing, offering promising results in the measurement of both degrees of freedom and, subsequently, the possibility of optimizing the total mode matching.

Chapter 2

Mode Mismatch: Concept and Principles

We saw in Chapter that minimizing losses is fundamental to maintaining the performance of interferometric GW detectors and that these detectors employ several optical cavities. One of the most important losses is caused by mode mismatch, which arises when the input beam's waist size and position are different than those supported by a cavity. In particular, since for the FDS a 300m optical cavity is used, it is fundamental to have the input beam matched to the cavity in order not to degrade the squeezing level and, consequently, maintain the target sensitivity.

In this chapter, the characteristics of Gaussian Beams and optical cavities will be described. The last two sections will focus on the description of mode mismatch and its implications.

2.1 Gaussian Beams

While the simplest solution to Maxwell's equations is a plane wave, it is an impractical description for real-world applications like laser beams due to its infinite extent in the plane transverse to the propagation direction. Laser beams are well collimated with a finite transverse intensity profile, necessitating a dedicated mathematical representation. To achieve this, we study the wave equation by employing the paraxial approximation, for which we assume that light rays propagate closely to the optical axis. Within this approximation, one of the solutions to the wave equation emerges as the Gaussian Beam, which features a Gaussian amplitude distribution across its cross-sectional area. To write the mathematical form for Gaussian beams, let us start with the electric field wave equation:

$$\nabla^2 E = \frac{1}{c^2}\frac{\partial^2 E}{\partial t^2} \tag{2.1}$$

where ∇^2 is the Laplacian and E is the electric field which we suppose has the form:

$$E(x, y, z, t) = E_0(x, y, z)e^{-i\omega t} \tag{2.2}$$

with E_0 being the complex field amplitude and ω the angular frequency of the wave. We can then rewrite (2.1) as:

$$(\nabla^2 + k^2)E_0(x, y, z) = 0 \tag{2.3}$$

with $k = \omega/c$. Consider now that the wave propagates along the z-axis, and assume it has the following form:

$$E(x, y, z) = u(x, y, z)\mathrm{e}^{ikz} \tag{2.4}$$

where $u(x, y, z)$ describes the transverse profile along the propagation. Then, equation (2.3) becomes:

$$\nabla^2 u(x, y, z) + 2ik\frac{\partial u(x, y, z)}{\partial z} = 0 \tag{2.5}$$

if the profile changes slowly with z compared to the scale of λ and of its transverse extent, then we can use the paraxial approximation:

$$\left|\frac{\partial^2 u}{\partial z^2}\right| \ll k\left|\frac{\partial u}{\partial z}\right| \qquad \left|\frac{\partial^2 u}{\partial z^2}\right| \ll \left|\frac{\partial^2 u}{\partial x^2}\right|, \left|\frac{\partial^2 u}{\partial y^2}\right| \tag{2.6}$$

If we use this information to compute equation (2.5), we obtain the Paraxial Helmholtz Equation (PHE) in cartesian coordinates

$$\frac{\partial^2 u}{\partial x^2} + \frac{\partial^2 u}{\partial y^2} + 2ik\frac{\partial u}{\partial z} = 0 \tag{2.7}$$

To solve this equation it is possible to separate the amplitude function into two functions both depending on z and, one of which is dependent on the transverse variable x and the other is dependent on the transverse variable y as:

$$u(x, y, z) = u_n(x, z)u_m(y, z) \tag{2.8}$$

As a result, the PHE can be examined by breaking it down into the two transverse directions of x and y. Specifically, the solutions are the product between a Gaussian function and the Hermite polynomials of order n and m. We call these solutions the Hermite-Gauss modes HG_{nm}:

$$HG_{nm} = \frac{\mathcal{C}_{nm}^{HG}}{w(z)} H_n\left(\frac{\sqrt{2}x}{w(z)}\right) H_m\left(\frac{\sqrt{2}y}{w(z)}\right) \exp\left[-\frac{x^2 + y^2}{w^2(z)}\right] \exp\left[ik\frac{x^2 + y^2}{2R(z)} - i\left(n + m + 1\right)\chi(z)\right] \tag{2.9}$$

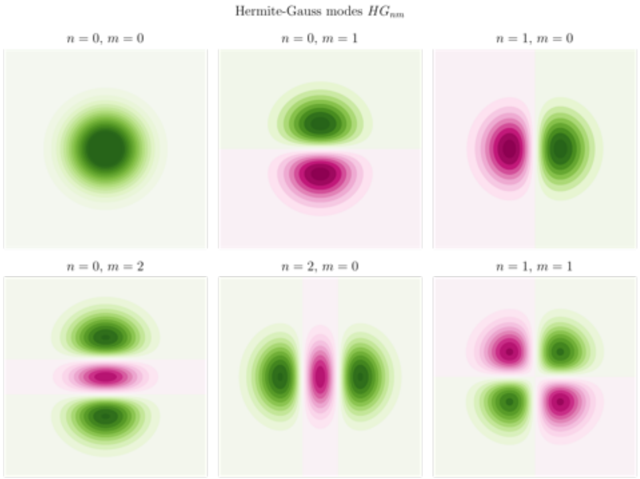

Figure 2.1: Hermite-Gauss intensity distribution for the first $N = 0, 1, 2$ orders. The green and pink colors represent regions of opposite electric field signs. The fundamental mode ($n = m = 0$) has a Gaussian distribution.

The total order of an HG_{nm} mode is calculated as the sum of the single polynomial orders: $N = n + m$. Figure 2.1 shows the HG_{nm} modes with $N = 0, 1, 2$. The normalization constant is $\mathcal{C}_{nm}^{HG} = \sqrt{2/(2^{n+m} n! m! \pi)}$. Since the Hermite polynomial $H_0 = 1$, the $n = m = 0$ mode has a simple bidimensional Gaussian intensity profile, and is called "fundamental mode". The width of the beam depends on z and is defined as the value for which the Gaussian amplitude drops to $1/e$ of its peak value:

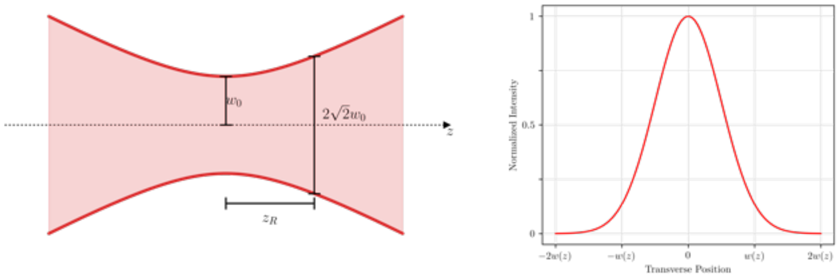

Figure 2.2: Left: Gaussian Beam profile as a function of the position z. The beam has a beam waist size w_0 and a Rayleigh range z_R. As the beam propagates along the z-axis, it narrows as it approaches the waist and broadens as it moves away. At the Rayleigh range, the beam radius increases to $\sqrt{2}$ times the beam waist size w_0. Right: Normalized Gaussian distribution of the beam intensity.

$$w(z) = w_0 \sqrt{1 + \left(\frac{z - z_0}{z_R} \right)^2} \tag{2.10}$$

with the constant w_0, called beam *waist*, being the minimum value for the radius, z_0 the position of the waist and z_R being the *Rayleigh range* defined as:

$$z_R = \frac{\pi w_0^2}{\lambda} \tag{2.11}$$

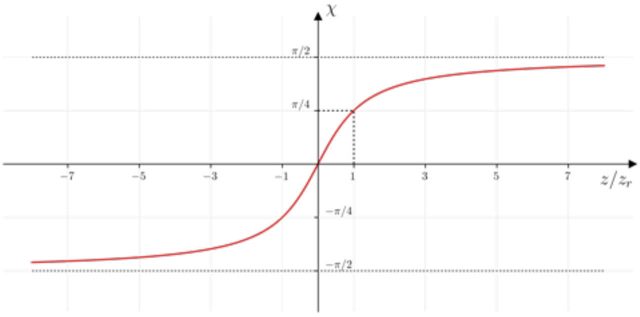

Figure 2.3: Gouy phase of a Gaussian beam. In the x-axis, values are represented in terms of z/z_R, where z is the propagation direction and z_R is the Rayleigh range.

The term $R(z)$ is the radius of curvature of the wavefront and is calculated as:

$$R(z) = (z - z_0)\left(1 + \left(\frac{z_R}{z - z_0}\right)^2\right) \tag{2.12}$$

It is useful to introduce the *complex beam parameter* $q(z)$ which can be defined as:

$$q(z) = (z - z_0) + iz_R \tag{2.13}$$

or alternatively:

$$\frac{1}{q(z)} = \frac{1}{R(z)} - \frac{i\lambda}{\pi w(z)^2} \tag{2.14}$$

Finally, the term $\chi(z)$ is the *Gouy phase*, which is due to the fact that Gaussian beams are confined in the transversal direction, therefore they acquire an additional phase with propagation with respect to a plane wave. In particular the function $\chi(z)$ has the following form:

$$\chi(z) = \arctan\left(\frac{z - z_0}{z_R}\right) \tag{2.15}$$

therefore the beam gains a π phase as it passes through the focus.

If we want to work in cylindrical coordinates, we can use the identity

$$\frac{\partial^2}{\partial x^2} + \frac{\partial^2}{\partial y^2} = \frac{\partial^2}{\partial r^2} + \frac{1}{r}\frac{\partial}{\partial r} + \frac{1}{r^2}\frac{\partial^2}{\partial \phi^2} \tag{2.16}$$

and combining it with the PHE we obtain the solutions known as Laguerre-Gauss modes:

$$LG_{lp} = \frac{C_{lp}^{LG}}{w(z)}\left(\frac{\sqrt{2}r}{w(z)}\right)^{|l|} L_p^{|l|}\left(\frac{2r^2}{w^2(z)}\right) \exp\left[-\frac{r^2}{w^2(z)}\right] \exp\left[-i\frac{kr^2}{2R(z)} - il\phi + i(|l| + 2p + 1)\chi(z)\right] \tag{2.17}$$

Where the indexes l and p are, respectively, the azimuthal and radial indexes. The normalization constant is $C_{lp}^{LG} = \sqrt{2p!/(\pi(|l|+p)!)}$ and $L_p^{|l|}$ are the Laguerre polynomials. The total order is calculated as $N = 2p + |l|$. Figure 2.4 shows the LG_{nm} modes with $N = 0, 2, 4$, with $l = 0$ and

$p = 0, 1, 2$, therefore with no dependency on the azimuthal angle ϕ. Note that the fundamental Gaussian beam is exactly the same in the two bases.

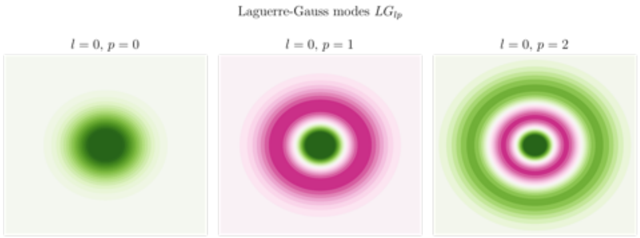

Figure 2.4: Laguerre-Gauss intensity distribution for the first $N = 0, 2, 4$ orders. The green and pink colors represent regions of opposite electric field signs. The fundamental order ($l = p = 0$) has the same Gaussian distribution as the Hermite-Gauss.

The Laguerre-Gauss and Hermite-Gauss modes constitute two distinct sets of functions that form a complete orthonormal basis for every paraxial beam solution of the PHE. From a mathematical perspective, one basis is just as valid as another, and it is possible to convert between them. Beijersbergen et al. [37] demonstrated how to convert HG modes into LG modes. For simplicity in notation they used the n,m indices also for the LG modes, being the radial index $p = \min(n, m)$ and the azimuthal index $l = |n - m|$. The conversion relationship then is:

$$LG_{nm}(x, y, z) = \sum_{k=0}^{N} i^k b(n, m, k) HG_{N-k,k}(x, y, z) \tag{2.18}$$

where the real coefficients $b(n, m, k)$ is calculated as:

$$b(n, m, k) = \sqrt{\frac{(N-k)!k!}{2^N n!m!}} \frac{1}{k!} \frac{d^k}{dt^k} \left[(1-t)^n (1+t)^m\right] \tag{2.19}$$

It is also useful to convert between the HG modes with principal axes aligned along the (x, y) axis and those with principal axes forming a 45-degree angle, commonly referred to as diagonal modes, $HG^{45}_{nm}(x, y, z) = HG_{nm}(\frac{x+y}{\sqrt{2}}, \frac{x-y}{\sqrt{2}}, z)$:

$$HG^{45}_{nm}(x, y, z) = \sum_{k=0}^{N} b(n, m, k) HG_{N-k,k}(x, y, z) \tag{2.20}$$

where the coefficients $b(n, m, k)$ are the ones calculated in equation (2.19). The main difference between the conversions in equation (2.18) and in equation (2.20) is that the first has a $\pi/2$ phase difference between successive HG_{nm} modes due to the presence of i^k, while in the latter every HG_{nm} mode is in-phase.

2.2 Optical Resonators

An optical resonator, or cavity, is composed of two (or more) precisely positioned mirrors configured to enable the resonance of a laser beam. These mirrors, typically highly reflective, are meticulously arranged to form a closed path for the light. Resonance occurs when specific requirements are met. In particular, the light bouncing back and forth needs to come back perfectly in phase with itself and with the same transverse intensity distribution, leading to constructive interference and, therefore, building up in intensity within the cavity.

In the first part of this section, we will see how to find the general stability condition to obtain stable resonance inside a cavity. Then we will see how this applies to a linear cavity. Moreover, we will see some important quantities that describe cavities, detailing the differences between resonators with an even and an odd number of mirrors.

2.2.1 Stability condition

To study the evolution of a Gaussian beam in an optical system, we can use the ABCD matrix formalism, which allows the description of the beam's evolution through matrices. Using this formalism, it is possible to define the q-parameter output, q_2, in terms of the input q-parameter, q_1, as [38]:

$$q_2 = \frac{Aq_1 + B}{Cq_1 + D} \tag{2.21}$$

where $q_1 = (z - z_1) + iz_{R1}$. In Table 2.5 are listed the ABCD matrices for the simplest optical systems. Generally, the ABCD determinant is equal to unity:

$$AD - BC = 1 \tag{2.22}$$

In order to have a stable resonance inside an optical cavity, the laser beam needs to replicate itself at each round-trip and therefore experience a periodic focusing action as in a periodic sequence of lenses [39]. Therefore, by using the ABCD matrices of Table 2.5, we can write the matrix of the optical system as the ABCD matrix T_{el} of the repeated element of the sequence to the power of the total number of round-trips N. The matrix of the optical cavity after N round trips is:

$$T_{el}^N = \begin{pmatrix} A & B \\ C & D \end{pmatrix}^N \tag{2.23}$$

In our case, the matrix T_{el} is the ABCD matrix for one round-trip, which consists of the multiplication of the single elements of the cavity including the free propagation. We can compute the matrix raised to the power of N by using Sylvester's matrix polynomial theorem.

Optical system	**ABCD matrix**
Free space distance d	$\begin{pmatrix} 1 & d \\ 0 & 1 \end{pmatrix}$
Medium of length d and refractive index n	$\begin{pmatrix} 1 & d/n \\ 0 & 1 \end{pmatrix}$
Reflection flat mirror	$\begin{pmatrix} 1 & 0 \\ 0 & 1 \end{pmatrix}$
Reflection curved mirror with radius of curvature R	$\begin{pmatrix} 1 & 0 \\ -\frac{2}{R} & 1 \end{pmatrix}$
Thin lens of focal f	$\begin{pmatrix} 1 & 0 \\ -\frac{1}{f} & 1 \end{pmatrix}$

Table 2.5: ABCD matrices for the simplest optical systems

If T_{el} is a $m \times m$ matrix with scalar eigenvalues $\lambda_1, \lambda_2, ...\lambda_m$, we can write T_{el}^N as [40]:

$$T_{el}^N = \sum_{j=1}^{m} \left(\lambda_j^N \prod_{i \neq j}^{m} \frac{\lambda_i I - T_{el}}{\lambda_i - \lambda_j} \right) \tag{2.24}$$

By studying its eigenvalues λ we can obtain conditions of the stability of the cavity. The characteristic equation of T_{el} is:

$$(A - \lambda)(D - \lambda) - BC = 0 \tag{2.25}$$

Using the fact that the determinant is unity we get:

$$\lambda^2 - (A + D)\lambda + 1 = 0 \tag{2.26}$$

if we define $m \equiv (A + D)/2$ then we can write the solution for the eigenvalues as:

$$\lambda = m \pm \sqrt{m^2 - 1} \tag{2.27}$$

Calling r_+ and r_- the eigenvectors of the ABCD matrix, we can then study two cases:

1. $|m| \leq 1$: we can write $m = \cos\phi$ and therefore $\lambda_\pm = e^{\pm i\phi}$. We can write the solution for the final ray after n roundtrip inside the cavity as

$$\mathbf{r}_n = c_- e^{-in\phi}\mathbf{r}_- + c_+ e^{in\phi}\mathbf{r}_+ \tag{2.28}$$

2. $|m| > 1$: the eigenvalues are positive and real, and we can write $m = \cosh\psi$. After n

round trips we can write the final ray as:

$$\mathbf{r}_n = c_- e^{n\psi}\mathbf{r}_- + c_+ e^{n\psi}\mathbf{r}_+ \tag{2.29}$$

The first case describes an oscillatory behavior therefore stable, while the second relation has an exponential damping on one component and exponential growth on the other one. That means the second relation gives an unstable resonator. We can finally write the stability condition $|m| \leq 1$ as:

$$0 \leq \frac{A+D+2}{4} \leq 1 \tag{2.30}$$

It is also possible to express the Gouy phase accumulated inside the optical cavity in terms of the entries of the ABCD matrix. In fact, as was demonstrated by Erden et al. [41], we can write the ABCD values as:

$$A = \frac{w_2}{w_1}\cos\tilde{\chi} - \frac{B}{R_1} \tag{2.31}$$

$$B = \frac{w_1 w_2 \pi}{\lambda}\sin\tilde{\chi} \tag{2.32}$$

$$C = \frac{A}{R_2} - \frac{\frac{1}{R_1}\left(A + \frac{B}{R_1}\right) + \frac{B\lambda^2}{\pi^2 w_1^4}}{\left(A + \frac{B}{R_1}\right)^2 + \frac{B\lambda^2}{\pi^2 w_1^4}} \tag{2.33}$$

$$D = \frac{BC+1}{A} \tag{2.34}$$

where $\tilde{\chi}$ is the accumulated Gouy phase through the optical system, w_1 and w_2 are the input and output beam radius (eq.(2.10)), R_1 and R_2 are the radii of curvature of the input and output wavefront (eq.(2.12)) and λ is the wavelength of the beam. We can now take the quantity in equation (2.30) and, taking into account that after one round-trip the beam has to replicate itself, we obtain:

$$\chi_{cav} = 2\arccos\left(\mathrm{sgn}B\sqrt{\frac{A+D+2}{4}}\right) \tag{2.35}$$

where we used the sign of B to solve the sign ambiguity given by the cosine [42].

In the next section, we will see how we can write conditions (2.30) and (2.35) for a linear cavity.

2.2.2 Two-mirrors Cavity

Suppose we have a linear cavity. As said in the previous section, we can consider the optical cavity as a periodic sequence of lenses, shown in Figure 2.6. We can write the ABCD matrix of the single element in the sequence after one round-trip as the multiplication of the ABCD matrices for the lens of focal f_2, followed by a spacing L, followed by the lens of focal f_1 and another spacing L:

$$\begin{pmatrix} A & B \\ C & D \end{pmatrix} = \begin{pmatrix} 1-\frac{L}{f_1} & 2L-\frac{L^2}{f_1} \\ -\frac{1}{f_1}-\frac{1}{f_2}+\frac{L}{f_1 f_2} & 1-\frac{L}{f_1}-\frac{2L}{f_2}+\frac{L^2}{f_1 f_2} \end{pmatrix} \tag{2.36}$$

The focal lengths f_1 and f_2 of the lenses are the same as the ones of the mirrors, which means $f_1 = R_1/2$ and $f_2 = R_2/2$, where R_1 and R_2 are the radii of curvature of the mirrors, and the distance between the lenses is equal to the length of the cavity L, as shown in Figure 2.6. We can rewrite the stability condition in equation (2.30) as:

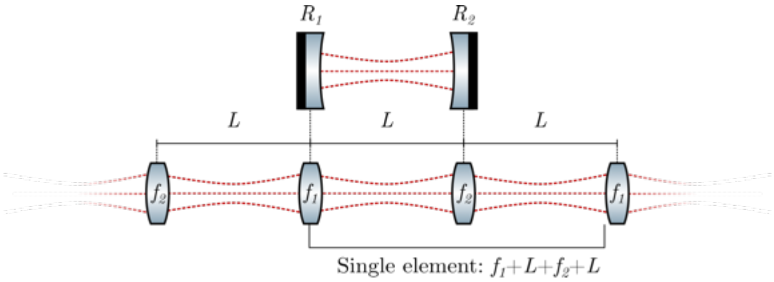

Figure 2.6: An optical cavity with mirrors with radii of curvature R_1 and R_2 can be described as a sequence of lenses at the same distance with focal length $f_1 = R_1/2$ and $f_2 = R_2/2$. The single element of the sequence is composed of the lens f_1 followed by a spacing L, followed by the lens f_2 and another spacing L.

$$0 \leq g_1 g_2 \leq 1 \tag{2.37}$$

where we define the *g-parameters* of the resonator as:

$$g_i \equiv 1 - \frac{L}{R_i} \tag{2.38}$$

where the i stands for the mirror, in our case $i = \{1, 2\}$. This condition defines a stability region in the g_1, g_2 space for linear optical cavities, shown in Figure 2.7. As we can see from this plot, if the g-parameters of the optical resonator fall inside the shaded area then it will be stable, and different Gaussian modes can resonate inside it. The plane-parallel resonator is also called the *Fabry-Pérot cavity* and is at the basis of many interferometers.

To find the waist of the supported resonant beam inside the cavity and the positions of the mirrors with respect to the supported waist, we need to impose that the Gaussian beam's wavefront has the same curvature as the mirrors when it interacts with them. Using equation (2.12) we can write:

$$\begin{cases} -R_1 = z_1 + \frac{z_R^2}{z1} \\ R_2 = z_2 + \frac{z_R^2}{z2} \\ z_2 - z_1 = L \end{cases} \tag{2.39}$$

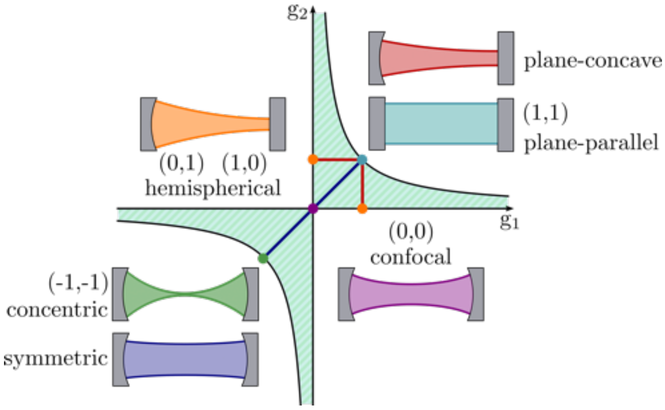

Figure 2.7: Stability condition for 2-mirrors cavities. The shaded area between $g_i = 0$ $i = (1, 2)$, $g_1 g_2 = 1$ is the stability region. Different types of resonators are also presented depending on their g-values[43].

Where z_1 and z_2 are the positions of the mirrors from the waist. By using the g-parameters, we can obtain the solutions as:

$$z_1 = -\frac{g_2(1 - g_1)}{g_1 + g_2 - 2g_1 g_2} L \tag{2.40}$$

$$z_2 = \frac{g_1(1 - g_2)}{g_1 + g_2 - 2g_1 g_2} L \tag{2.41}$$

$$w_0^2 = \frac{L\lambda}{\pi} \sqrt{\frac{g_1 g_2(1 - g_1 g_2)}{(g_1 + g_2 - 2g_1 g_2)^2}} \tag{2.42}$$

Since the *g-parameters* depend only on the geometrical quantities of the cavity, also the parameters of the resonating Gaussian beam depend only on the geometry of the cavity. From equation 2.42 we notice that if the stability condition in equation (2.37) is not satisfied, then we obtain imaginary values for the waist.

Moreover, using equation (2.35), for a two-mirrors system the Gouy phase accumulated is:

$$\chi_{cav} = 2 \arccos(\text{sgn} g_2 \cdot \sqrt{g_1 g_2}) \tag{2.43}$$

In addition to replicating its intensity profile after a round trip, we need to find the condition for which the field comes back in phase with itself, thus constructively interfering at each round trip. While the stability condition is a macroscopic geometric condition on the resonator, the one we are about to address is a microscopic one. In fact, the variation of the resonator length to obtain the correct phase for the constructive interference is of the order of the beam wavelength, therefore it does not affect the stability condition. To do this let us compute the transmitted, circulating and reflected fields. We define r_i and t_i as reflectivity and transmittivity of the mirrors (see fig.2.8). Assuming mirrors have a loss ρ_i, we have that:

$$r_i^2 + t_i^2 = 1 - \rho_i \tag{2.44}$$

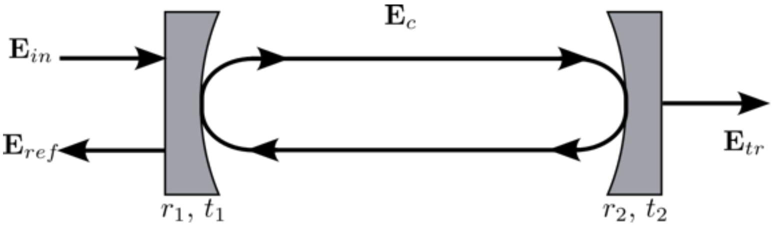

Figure 2.8: Scheme of an optical cavity with two mirrors: the first mirror, also called input mirror, has reflectivity r_1 and transmittivity t_1, while the second mirror, referred to as output mirror, has r_2 and t_2. The incident beam E_{in} on the input mirror is in part reflected and in part transmitted. The reflected beam E_{ref} is composed of the promptly reflected beam and the leaked beam. The transmitted light is trapped inside the cavity in a steady state, E_c. From the output mirror, we observe a fraction of the circulating field E_c which is transmitted by the mirror, identified as E_t.

A beam propagating along the z-axis is given by:

$$E_{in}(z) = E_0 e^{ikz} \tag{2.45}$$

The input mirror is positioned at $z = 0$, therefore just before entering the cavity is $E_{in}(0) = E_0$. When it reaches the input mirror, part of this beam is promptly reflected obtaining $E_0^r = r_1 E_0$, and part is transmitted as $E_0^t = t_1 E_0$. The transmitted beam propagates to the second mirror, placed at $z = L$, from which it gets reflected. When it reaches back to the first mirror it has acquired a phase of $2kL$, therefore we get $E_{2L}^r = t_1 r_2 E_0 e^{i2kL}$. If we repeat this process for n round-trips, we obtain the circulating field inside the cavity as:

$$E_c(t) = it_1 E_0 \sum_{n=0}^{\infty} (r_1 r_2 e^{i2\phi})^n = \frac{t_1}{1 - r_1 r_2 e^{i2\phi}} E_{in}(t) \tag{2.46}$$

where $\phi = kL$. From this, we can obtain the circulating intensity relative to the input intensity by calculating the squared modulus of $E_c(t)/E_{in}(t)$:

$$A_c = \frac{I_c}{I_{in}} = \frac{|E_c(t)|^2}{|E_{in}(t)|^2} = \frac{t_1^2}{(1 - r_1 r_2)^2 + 4 r_1 r_2 \sin^2(\phi)} \tag{2.47}$$

We can compute the same for the transmitted field $E_{tr}(t)$ and the reflected field $E_{ref}(t)$:

$$E_{tr}(t) = \frac{-t_1 t_2 e^{i\phi}}{1 - r_1 r_2 e^{i2\phi}} E_{in}(t) \tag{2.48}$$

$$E_{ref}(t) = r_1 E_{in}(t) - \frac{t_1^2 r_2 e^{i2\phi}}{1 - r_1 r_2 e^{i2\phi}} E_{in}(t) = \frac{r_1 - (r_1^2 + t_1^2) r_2 e^{i2\phi}}{1 - r_1 r_2 e^{i2\phi}} E_{in}(t) \tag{2.49}$$

where the reflected field in equation (2.49), is calculated as the sum of the promptly reflected field and the leaked field. We can then write the transmitted and reflected intensity relative to the input as:

$$A_{tr} = \frac{I_{tr}}{I_{in}} = \frac{|E_{tr}(t)|^2}{|E_{in}(t)|^2} = \frac{t_1^2 t_2^2}{(1 - r_1 r_2)^2 + 4 r_1 r_2 \sin^2(\phi)} \tag{2.50}$$

$$A_{ref} = \frac{I_{tr}}{I_{in}} = \frac{|E_{ref}(t)|^2}{|E_{in}(t)|^2} = \frac{\left(r_1 - r_2(r_1^2 + t_1^2)\right)^2 + 4 r_1 r_2 (r_1^2 + t_1^2) \sin^2(\phi)}{(1 - r_1 r_2)^2 + 4 r_1 r_2 \sin^2(\phi)} \tag{2.51}$$

In order to build up the resonance we need to maximize the circulating field. Taking equation (2.47) we obtain a resonance condition for the phase in a round-trip 2ϕ:

$$2\phi = 2\pi q \tag{2.52}$$

with q an integer. For Gaussian modes, we need to also take into account the contribution of the Gouy phase in ϕ. Therefore, taking equation (2.9) and combining it with (2.52) we obtain the resonance condition for an HG_{nm} mode inside a linear cavity of round-trip $2L$ as:

$$k2L - (n + m + 1)\chi_{cav} = 2\pi q \tag{2.53}$$

for a LG_{lp} mode we just replace $n + m = 2p + l$. As we can see for each mode we do have a different resonant condition being dependent on the order mode. However, we have that modes with same order $N = n + m$ resonate at the same frequency ν_{nm}:

$$\nu_{nm} = \frac{c}{2L} q + \frac{c}{2L} \frac{(n + m + 1)\chi_{cav}}{2\pi} \tag{2.54}$$

This equation holds more generally for optical cavities with an even number of mirrors. We will see in the next section how this changes for an odd number. Moreover from this equation, we can define an important quantity, the *Free Spectral Range* (FSR):

$$FSR = \frac{c}{2L} \tag{2.55}$$

which describes the spacing frequency between two consecutive longitudinal modes $q \to q + 1$. We can also compute the same between two transversal modes $N \to N + 1$, called *Higher Order Mode* (HOM) spacing frequency:

$$HOM = \frac{FSR}{\pi} \arccos(\mathrm{sgn} g_2 \cdot \sqrt{g_1 g_2}) \tag{2.56}$$

Another characteristic parameter of an optical cavity is the linewidth, usually defined as the *full width at half maximum*, FWHM, or in terms of the *pole frequency* f_p:

$$FWHM = 2f_p = \frac{2FSR}{\pi} \arcsin\left(\frac{1 - r_1 r_2}{2\sqrt{r_1 r_2}}\right) \tag{2.57}$$

We define *finesse*, F, as the ratio between the FSR and the linewidth:

$$F = \frac{\pi}{2\arcsin\left(\frac{1-r_1 r_2}{2\sqrt{r_1 r_2}}\right)} \tag{2.58}$$

This parameter quantifies how selective in frequency the resonance is. For high values of reflection coefficients, that is r_1 and r_2 closed to 1, we can make the approximation:

$$F = \frac{\pi}{1 - r_1 r_2} \tag{2.59}$$

In Figure 2.9 these quantities are shown graphically.

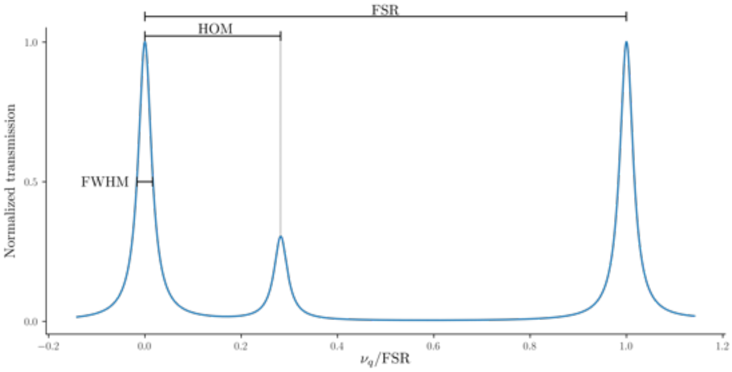

Figure 2.9: Normalized transmission of an optical cavity. The Free Spectral Range is defined as the frequency spacing between two fundamental modes, while the Higher-Order Mode frequency spacing is defined between two consecutive modes (in this case the fundamental and the first higher-order mode).

2.2.3 Odd and Even Cavities

Until now we only discussed 2-mirror cavities. There are some differences when we work with a cavity with an odd number of mirrors such as a triangular one, as shown in Figure 2.10. In particular, the resonance frequencies of odd horizontal modes, that is modes with n odd, will be shifted of half FSR. To understand this let us suppose that the coordinate system we are working with has z along the direction of propagation, x parallel to the plane of incidence and y perpendicular to it. Let us also write the transversal field distribution at a given point z_1 as [44]:

$$E(x, y|z_1) = E_0 \sum_{nm} a_{mn} HG_{nm}(x, y|z_1) \tag{2.60}$$

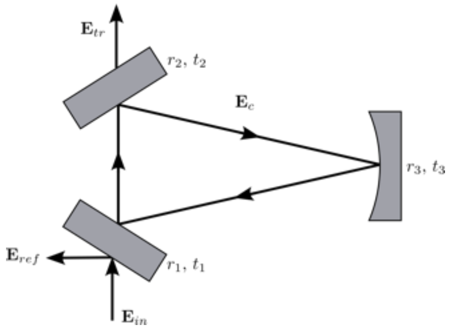

Figure 2.10: Scheme of an optical cavity with three mirrors arranged in an isosceles triangle.

where a_{mn} is the complex coefficient of the mode HG_{nm} at the given point z_1. When the beam is reflected by a mirror the field distribution does not change, however, the x-axis is flipped. Taking a point z_2 just after the reflection:

$$HG_{nm}(x, y|z_1) \to HG_{nm}(-x, y|z_2) \tag{2.61}$$

The Hermite-Gauss modes are eigenfunctions of this transformation with eigenvalues ±1,

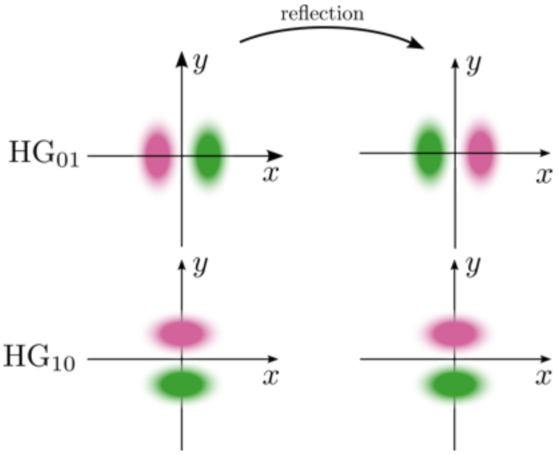

Figure 2.11: Example of behaviour upon reflection of the HG_{10} and HG_{01} modes. The propagation is along the z-axis while the incident plane is parallel to the x-axis. When there is an anti-symmetry between the mode and the y-axis then the mode acquires a π phase and is inversed, thus, for an odd number of reflections, the resonance is shifted by π radians, or half FSR.

therefore we can write it as a transformation of the complex coefficients as:

$$a_{mn} \to a'_{mn} = (-1)^n a_{mn} \tag{2.62}$$

Suppose n odd, then an optical cavity with an even number of mirrors will have an even number of this inversion. However, if a cavity has an odd number of mirrors, then we will have a negative sign in the complex coefficient which can be just incorporated as a π phase of the H_{nm} mode.

Therefore we need to modify equation (2.53) as:

$$k2L - (n+m+1)\chi_{cav} - \pi = 2\pi q \tag{2.63}$$

obtaining the resonant frequencies for an odd cavity:

$$\nu_{nm}^{odd} = FSR\left(q + (n+m+1)\frac{\chi_{cav}}{2\pi} + \frac{1}{2}\right) \tag{2.64}$$

Defining M as the number of mirrors, we can give a more general definition of the resonant frequency inside a cavity:

$$\nu_{nm} = FSR\left(q + (n+m+1)\frac{\chi_{cav}}{2\pi} + \frac{1-(-1)^{nM}}{4}\right) \tag{2.65}$$

Since the layout of a triangular cavity as shown in Figure 2.10 is symmetric, it is possible to simplify it with a linear cavity with length equal to the hypotenuse plus half the base, however,

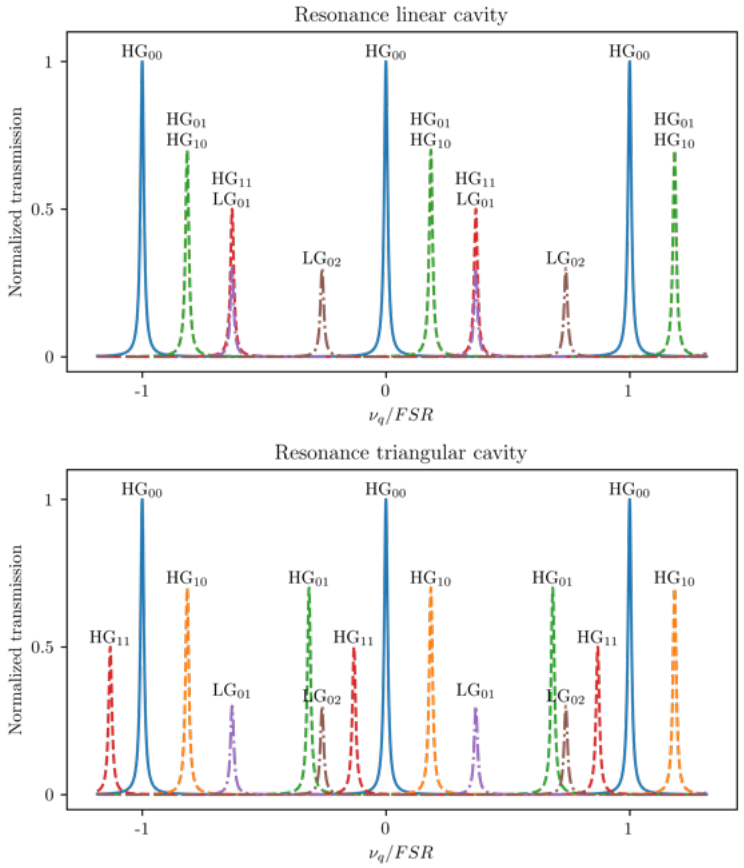

Figure 2.12: Normalized transmission for linear (up) and triangular (down) cavities with same parameters. The triangular cavity discriminates between horizontal and vertical modes. Here, also, represented the LG_{lp} modes which has symmetry with respect to the y-axis, and therefore does not experiment the π phase shift.

when studying it is fundamental to take into account the π phase due to the presence of the three mirrors. The differences in the resonant frequencies for the two cases are shown in Figure 2.12.

2.3 Mode Mismatch

Achieving optimal alignment and mode-matching within an optical cavity ensures complete coupling of the power inside the cavity when it is on resonance. D. Z. Anderson [45] illustrated how slight misalignment and mode mismatch result in coupling with the first and second higher-order transverse modes, respectively. In this section, we will primarily focus on the effects of mode mismatch coupling, but similar calculations can be applied to misalignment.

There are two types of mismatch to consider: waist size and waist position mismatch (see Fig. 2.13), relative to the values supported by the cavity (refer to Section 2.2.2). For simplicity, we are going to work in cylindrical coordinates with the Laguerre-Gauss modes (eq. (2.17)). Recalling from equation (2.17) how to calculate them, we can write the modes with $l = 0$ and $p = 0, 1, 2$, therefore with no dependency on the azimuthal angle ϕ, as:

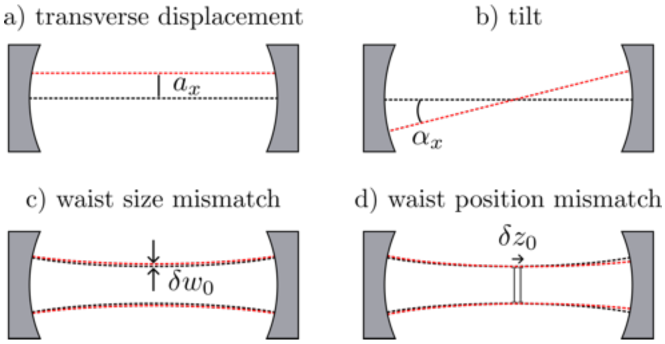

Figure 2.13: Misalignment and mismatch of the input beam. a) Transverse displacement from the cavity axis, b) angular misalignment, which is a tilt with respect to the axis, c) waist size mismatch and d) waist position mismatch with respect to the size and position supported by the cavity.

$$LG_{00}(r,z) = \sqrt{\frac{2}{\pi}}\frac{1}{w(z)}\exp\left\{\left[-\frac{r^2}{w^2(z)} - i\frac{kr^2}{2R(z)} + i\chi(z)\right]\right\} \tag{2.66}$$

$$LG_{01}(r,z) = \left(1 - \frac{2r^2}{w(z)^2}\right)\exp\left[2i\chi(z)\right] LG_{00}(r,z) \tag{2.67}$$

$$LG_{02}(r,z) = \left(1 - \frac{4r^2}{w(z)^2} + \frac{2r^4}{w(z)^4}\right)\exp\left[4i\chi(z)\right] LG_{00}(r,z) \tag{2.68}$$

In the next part, we are going to calculate the Taylor expansion with respect to the waist mismatch in size and position and evaluate it in $z = 0$, assuming it as the cavity waist coordinate.

2.3.1 Waist size mismatch

To calculate the coupling resulting from a slight waist size mismatch, let's assume that the beam is aligned and nearly mode-matched. The only variation is attributed to a small difference $w_0^{IN} - w_0^{CAV} = \delta w_0$ in the waist size, then:

$$LG_{00}(r|w_0 + \delta w_0) \simeq LG_{00}(r|w_0) + \delta w_0 \left.\frac{\partial LG_{00}(r,z)}{\partial w_0}\right|_{z=0} \tag{2.69}$$

Where we limited the study to the first-order derivative since we are not interested in working with modes higher than the LG_{01}. If we compute the first order derivative and use equation (2.67), we obtain:

$$\left.\frac{\partial LG_{00}(r,z)}{\partial w_0}\right|_{z=0} = -\frac{1}{w_0}\left(1 - \frac{2r^2}{w_0^2}\right) LG_{00}(r|w_0) = -\frac{1}{w_0} LG_{01}(r|w_0) \tag{2.70}$$

We perform the same calculations for the Laguerre-Gauss mode LG_{01}:

$$LG_{01}(r|w_0 + \delta w_0) \simeq LG_{01}(r|w_0) + \delta w_0 \left.\frac{\partial LG_{01}(r,z)}{\partial w_0}\right|_{z=0} \tag{2.71}$$

Again, the derivative of the LG_{01} mode with respect to the waist is:

$$\begin{aligned}\left.\frac{\partial LG_{01}(r,z)}{\partial w_0}\right|_{z=0} = &-\frac{2}{w_0}\left(\frac{1}{2} - \frac{4r^2}{w_0^2} + \frac{2r^4}{w_0^4}\right) LG_{00}(r|w_0) = \\ &\frac{1}{w_0}\left[LG_{00}(r|w_0) - 2LG_{02}(r|w_0)\right]\end{aligned} \tag{2.72}$$

We define the *waist size mismatch parameter* β as the difference δw_0 normalized to the waist dimension w_0:

$$\beta = \frac{\delta w_0}{w_0^{cav}} \tag{2.73}$$

Then we can write the fundamental input mode in terms of the cavity basis as:

$$LG_{00}(r|\beta) \simeq LG_{00}(r|w_0) - \beta LG_{01}(r|w_0) \tag{2.74}$$

and the first-order LG mode of the input beam as:

$$LG_{01}(r|\beta) \simeq LG_{01}(r|w_0) + \beta\left(LG_{00}(r|w_0) - 2LG_{02}(r|w_0)\right) \tag{2.75}$$

2.3.2 Waist position mismatch

Let us now assume that the input beam is perfectly matched in waist size to the cavity, while the position is slightly different. Analogously to what we did in the previous section, we define $z_0^{IN} - z_0^{CAV} = \delta z_0$ and we perform the Taylor expansion of the fundamental and first-order

Laguerre-Gauss mode with respect to z:

$$LG_{00}(r,\delta z_0) \simeq LG_{00}(r|w_0) + \delta z_0 \left.\frac{\partial LG_{00}(r,z)}{\partial z_0}\right|_{z=0} \tag{2.76}$$

The derivative becomes:

$$\begin{aligned}\left.\frac{\partial LG_{00}(r,z)}{\partial z}\right|_{z=0} =& \frac{i}{2z_R}\left(2-\frac{2r^2}{w_0^2}\right)LG_{00}(r|w_0) = \\ & \frac{i}{2z_R}\left[LG_{00}(r|w_0)+LG_{01}(r|w_0)\right]\end{aligned} \tag{2.77}$$

And again for the expansion of the first Laguerre-Gauss mode LG_{01}:

$$LG_{01}(r,\delta z_0) \simeq LG_{01}(r|w_0) + \delta z_0 \left.\frac{\partial LG_{01}(r,z)}{\partial z_0}\right|_{z=0} \tag{2.78}$$

where the derivative is:

$$\begin{aligned}\left.\frac{\partial LG_{01}(r,z)}{\partial z}\right|_{z=0} =& \frac{i}{z_R}\left(3-\frac{7r^2}{w_0^2}+\frac{2r^4}{w_0^4}\right)LG_{00}(r|w_0) = \\ & \frac{i}{2z_R}\left(LG_{00}(r|w_0)+3LG_{01}(r|w_0)+2LG_{02}(r|w_0)\right)\end{aligned} \tag{2.79}$$

We define, then, the *waist position mismatch parameter* γ as:

$$\gamma = \frac{\delta z_0}{2z_R^{cav}} \tag{2.80}$$

and using this parameter we can write the fundamental and first-order Laguerre-Gaussian modes for a small position mismatch as:

$$LG_{00}(r|\gamma) \simeq (1+i\gamma)\,LG_{00}(r|w_0) + i\gamma LG_{01}(r|w_0) \tag{2.81}$$

$$LG_{01}(r|\gamma) \simeq i\gamma LG_{00}(r|w_0) + (1+3i\gamma)\,LG_{01}(r|w_0) + 2i\gamma LG_{02}(r|w_0) \tag{2.82}$$

If we combine at first order in γ and β equations (2.74) with (2.81) and equations (2.75) with (2.82), we obtain the total effect on the fundamental mode and first-order Laguerre-Gauss mode due to mismatch both in size and position:

$$LG_{00}(r|\beta,\gamma) \simeq (1+i\gamma)\,LG_{00}(r|w_0) + (i\gamma-\beta)\,LG_{01}(r|w_0) \tag{2.83}$$

$$LG_{01}(r|\beta,\gamma) \simeq (i\gamma+\beta)\,LG_{00}(r|w_0) + (1+3i\gamma)\,LG_{01}(r|w_0) + (2i\gamma-2\beta)\,LG_{02}(r|w_0) \tag{2.84}$$

From equation (2.83) we see that an input beam with mode mismatch with respect to the cavity generates a coupling with the first-order Laguerre-Gauss mode LG_{01}. In particular size mismatch causes an in-phase coupling with this mode, while position mismatch is in quadrature-phase. The mode mismatch coupling, then, can be easily calculated as the amplitude of the complex coefficient:

$$MM_a = \sqrt{\gamma^2 + \beta^2} \tag{2.85}$$

Where the suffix a stands for *amplitude mismatch*. However, in this dissertation, we are going to use *power mismatch*, therefore:

$$MM = \gamma^2 + \beta^2 \tag{2.86}$$

The parameters γ and β are at the basis of this dissertation. In the next chapter, we will present a method to extract them by using RF modulation of the LG_{01} mode.

Chapter 3

RF Higher-Order Modulation Technique

In this chapter we will present a novel online mode-matching sensing technique, called RF higher-order modulation (RFHM) technique, able to measure mode mismatch and decouple the contributions of the mismatch parameters β and γ [46][47]. The idea behind this technique is the same as the one presented by P. Fulda et al.[48] for alignment sensing. The laser beam is modulated to introduce sidebands on the higher-order mode corresponding to the beam distortion (misalignment in the case of Fulda et al., mode mismatch in this work). The beat between the HOM carrier and its sidebands is then recorded by using a single-element photodiode in reflection from the cavity and the error signals on the beam distortion parameters are obtained through I/Q demodulation of the beat. It is important to note that the modulation frequency is set to be equal to the resonant frequency of the HOM in order to break the sideband symmetry and allow to sense the two mismatch degrees of freedom independently

Due to the relatively high frequency needed, to introduce the sidebands both methods use an optical element based on an electro-optical crystal sandwiched between electrodes. In particular, for alignment sensing the sidebands are generated through an Electro-Optical Beam Deflector (EOBD) in the HG_{01} mode, while for mode-mismatch sensing we use an Electro-Optical Lens (EOL) to introduce the sidebands on the LG_{01} mode.

The first section will cover more in depth the description of the RFHM technique for mode-mismatch, while the second section will provide an exhaustive explanation of the electro-optical effect.

3.1 Online Mode-Matching Sensing Technique

Our objective is to decouple the mode-mismatch coefficients encoded with the LG_{01} mode. The concept involves modulating the waist size or position (or a combination of the two) of the input beam. However, given the relatively high frequency values needed to match the HOM spacing of most cavities, on the order of MHz (RF), traditional mechanical lenses with actuators are impractical. Instead, we employ an Electro-Optical Lens (EOL).

3.1.1 LG_{01} RF Sidebands Generation

The working principle behind the EOL is the same as an electro-optical modulator (EOM): we rely on the Pockels effect to modulate the beam phase and generate sidebands. However, while an EOM nominally modulates the phase uniformly across the transverse plane, the EOL is designed to act as a lens. By strategically shaping the electrodes on the crystal and, therefore, modifying the refractive index through the external electric field, we transform the crystal into a lens that can generate sidebands in the LG_{01} mode.

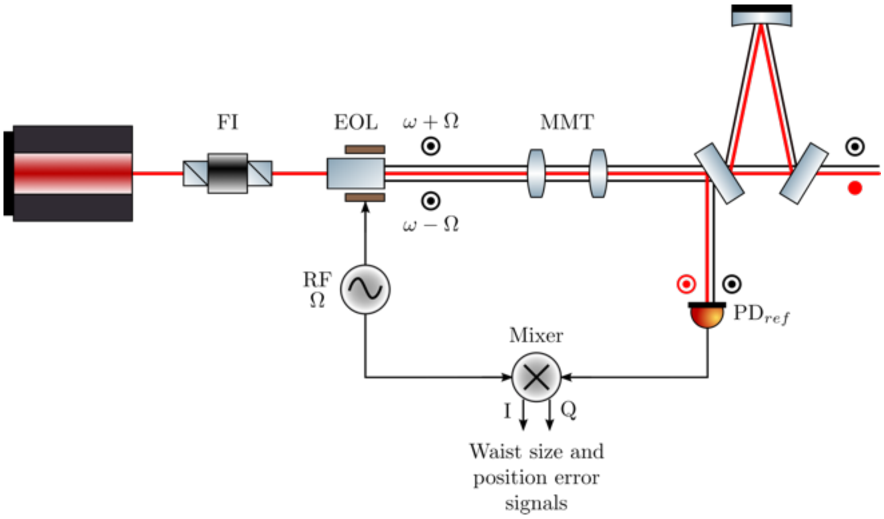

Figure 3.1: RFHM technique conceptual scheme. The EOL produces sidebands in the LG_{01} mode. One sideband is resonant inside the cavity together with the LG_{00} carrier while the other is reflected together with the LG_{01} carrier. Their beating is recorded by a PD and it is I/Q demodulated to obtain two signals that contain the information γ and β.

In Figure 3.1 we show the working principle layout of the RFHM technique. The beam enters inside the EOL which generates the sidebands on the LG_{01} mode. A mode-matching telescope (MMT) is placed after the EOL to match the beam parameters to those of the optical cavity. Once the beam arrives at the cavity, which is locked to the fundamental mode through the Pound-Drever-Hall (PDH) locking technique (see appendix A), the LG_{01} carrier is reflected back and reaches the single-element PD in reflection, which is the same used for the PDH error signal. For what concerns the LG_{01} sidebands, when both sidebands are reflected by the cavity, a single signal is generated, containing both mismatch parameters. In this scenario, it is not possible to isolate the mismatch terms because there is only one signal with mixed information. However, if the symmetry of the sidebands is broken, two signals are obtained after demodulation allowing for the separation of mismatch parameters. In order to have this situation we need to modulate the beam at twice the higher order mode spacing frequency of the cavity, $\Omega = 2HOM$.

Let us see quantitatively how the modulation changes the form of the beam entering the cavity. Suppose the EOL modulates at frequency Ω the waist size and waist position of the input beam. These modulations can be described as:

$$\mathrm{B} = \frac{\delta w_0^{EOL}}{w_0^{IN}} = \frac{m_B}{2}(e^{i\Omega t} + e^{-i\Omega t}) \tag{3.1}$$

$$\mathrm{G} = \frac{\delta z_0^{EOL}}{2 z_R^{IN}} = \frac{m_G}{2}(e^{i\Omega t} + e^{-i\Omega t}) \tag{3.2}$$

where δw_0^{EOL} and δz_0^{EOL} refer to the difference between the input and output beam, i.e. the change in waist position and dimension due to the EOL. The quantities m_B and m_G are the modulation depths of the EOL which depend on the overall focal length modulation (dependent on the external applied field) as well as on the position of the EOL along the beam. Similarly to equation (2.83), we can define the beam after the EOL in terms of the beam before the EOL, that is in the input beam basis LG_{lp}^{IN} which, in general, will be mismatched with respect to the cavity:

$$LG_{00}^{OUT}(r, z|B, G, \beta, \gamma) = (1 + iG)LG_{00}^{IN}(r, z|\beta, \gamma) + (iG - B)LG_{01}^{IN}(r, z|\beta, \gamma) \tag{3.3}$$

We can rewrite (3.3) in terms of the cavity base LG_{lp} using (2.83). Moreover, suppose that z is the propagation axis and that the actuator is at distance z_{EOL} from the cavity, we need to take into account the Gouy phase $\Delta\psi = \arctan(z_{EOL}/z_R^{IN})$ in LG_{01}. Therefore we obtain the beam at the input surface of the cavity::

$$\begin{aligned} LG_{00}(r, z|B, G, \beta, \gamma) = &\left[(1 + iG)(1 + i\gamma) + e^{i\Delta\psi}(iG - B)(\beta + i\gamma)\right] LG_{00}(r, z|w_0) \\ &+ \left[(1 + iG)(i\gamma - \beta) + e^{i\Delta\psi}(iG - B)(1 + 3i\gamma)\right] LG_{01}(r, z|w_0) \end{aligned} \tag{3.4}$$

The laser beam in input to the cavity is described by the product between the complex amplitude and the plane wave $u_0 e^{i\omega t - ikz_{EOL}}$, where u_0 is the amplitude of the plane wave and k is the wave number:

$$\begin{aligned} u_{in}^{cav}(r, z, t) = u_0 e^{i(\omega t - kz_{EOL})} &\left[\left[(1 + iG)(1 + i\gamma) + e^{i\Delta\psi}(iG - B)(\beta + i\gamma)\right] LG_{00}(r, z|w_0)\right. \\ &\left. + \left[(1 + iG)(i\gamma - \beta) + e^{i\Delta\psi}(iG - B)(1 + 3i\gamma)\right] LG_{01}(r, z|w_0)\right] \end{aligned} \tag{3.5}$$

Using the definitions of B and G in equations (3.1) and (3.2), we can rewrite equation (3.5) as:

$$u_{in}^{cav}(r,z,t) = u_0 e^{-ikz_{EOL}} \Big[a_{00} LG_{00}(r,z|w_0) e^{i\omega t} + b_{00} LG_{00}(r,z|w_0) \left(e^{i(\omega+\Omega)t} + e^{i(\omega-\Omega)t}\right) \\ + a_{01} LG_{01}(r,z|w_0) e^{i\omega t} + b_{01} LG_{01}(r,z|w_0) \left(e^{i(\omega+\Omega)t} + e^{i(\omega-\Omega)t}\right)\Big] \tag{3.6}$$

where the coefficients contain the information of the input beam and are defined as:

$$a_{00} = 1 + i\gamma \tag{3.7}$$

$$b_{00} = \frac{m_G}{2}\left(i - \gamma + e^{i\Delta\psi}(i\beta - \gamma)\right) - \frac{m_B}{2} e^{i\Delta\psi}(\beta + i\gamma) \tag{3.8}$$

$$a_{01} = i\gamma - \beta \tag{3.9}$$

$$b_{01} = -\frac{m_G}{2}\left(i\beta + \gamma - e^{i\Delta\psi}(i - 3\gamma)\right) - \frac{m_B}{2} e^{i\Delta\psi}(1 + i3\gamma) \tag{3.10}$$

From equation (3.6) we can clearly see how this kind of modulation generates sidebands on the LG_{00} and LG_{01} modes at frequency $\pm\Omega$.

3.1.2 Cavity Reflected Field

The photocurrent read by the single-element photodetector is defined as:

$$I_{ref} = \int_{-\infty}^{\infty} \int_{-\infty}^{\infty} u_{ref} u_{ref}^* dx dy \tag{3.11}$$

where u_{ref} is the reflected field. To calculate it we multiply each incident beam (the LG_{00} and LG_{01} carriers and their sidebands at $\pm\Omega$) in equation (3.6) by the complex reflection coefficient $F_{lp}(\omega)$ of the cavity at the respective frequency. This coefficient is calculated as the ratio between the reflected and the incident fields from equation (2.49), for which we obtain:

$$F_{lp}(\omega) = \frac{r_1 - r_2(r_1^2 + t_1^2) \exp\left(-i\left(\frac{\omega}{FSR} + N\psi_{rt}\right)\right)}{1 - r_1 r_2 \exp\left(-i\left(\frac{\omega}{FSR} + N\psi_{rt}\right)\right)} \tag{3.12}$$

where r_1,r_2,t_1 and t_2 are the reflectivity and the transmissivity of the cavity mirrors, and ψ_{rt} is the Gouy phase accumulated after one round-trip and $N = 2p + l$. We can write the reflected field as:

$$u_{ref}(r,z) = u_0 e^{-ikz_{EOL}} \left[f_{00} LG_{00}(r,z|w_0) + f_{01} LG_{01}(r,z|w_0)\right] \tag{3.13}$$

where:

$$f_{00} = a_{00} F_{00}(\omega) e^{i\omega t} + b_{00}\left(F_{00}(\omega+\Omega) e^{i(\omega+\Omega)t} + F_{00}(\omega-\Omega) e^{i(\omega-\Omega)t}\right) \tag{3.14}$$

$$f_{01} = a_{01} F_{01}(\omega) e^{i\omega t} + b_{01}\left(F_{01}(\omega+\Omega) e^{i(\omega+\Omega)t} + F_{01}(\omega-\Omega) e^{i(\omega-\Omega)t}\right) \tag{3.15}$$

Defining $I_0 = |u_0|^2$, using the orthogonality of the modes we can write:

$$\frac{I_{ref}}{I_0} = |f_{00}|^2 + |f_{01}|^2 \tag{3.16}$$

with:

$$\begin{aligned} |f_{00}|^2 =& |a_{00}F_{00}(\omega)|^2 + |b_{00}|^2(|F_{00}(\omega+\Omega)|^2 + |F_{00}(\omega-\Omega)|^2) \\ &+ a_{00}b_{00}^* F_{00}(\omega)\left(F_{00}^*(\omega+\Omega)e^{-i\Omega t} + F_{00}^*(\omega-\Omega)e^{i\Omega t}\right) \\ &+ a_{00}^* b_{00} F_{00}^*(\omega)\left(F_{00}(\omega+\Omega)e^{i\Omega t} + F_{00}(\omega-\Omega)e^{-i\Omega t}\right) + (2\Omega \text{ terms}) \end{aligned} \tag{3.17}$$

$$\begin{aligned} |f_{01}|^2 =& |a_{01}F_{01}(\omega)|^2 + |b_{01}|^2(|F_{01}(\omega+\Omega)|^2 + |F_{01}(\omega-\Omega)|^2) \\ &+ a_{01}b_{01}^* F_{01}(\omega)\left(F_{01}^*(\omega+\Omega)e^{-i\Omega t} + F_{01}^*(\omega-\Omega)e^{i\Omega t}\right) \\ &+ a_{01}^* b_{01} F_{01}^*(\omega)\left(F_{01}(\omega+\Omega)e^{i\Omega t} + F_{01}(\omega-\Omega)e^{-i\Omega t}\right) + (2\Omega \text{ terms}) \end{aligned} \tag{3.18}$$

We can demodulate the signal read by the photodetector by mixing it with a local oscillator at frequency Ω and low-pass filtering it. Therefore only the terms with $e^{\pm i\Omega t}$ remain and their coefficients, at first order in γ and β are:

$$a_{00}b_{00}^* = -\frac{m_G}{2}\left(i + e^{-i\Delta\psi}(i\beta+\gamma)\right) - \frac{m_B}{2}e^{-i\Delta\psi}(\beta - i\gamma) \tag{3.19}$$

$$a_{01}b_{01}^* = \frac{e^{-i\Delta\psi}}{2}\left(\gamma m_G + \beta m_B + i\beta m_G - i\gamma m_B\right) \tag{3.20}$$

After some math, we can obtain:

$$\begin{aligned} \frac{I_{ref}}{I_0} =& 2\cos\Omega t\,\mathrm{Re}\left[a_{00}b_{00}^*F_{00}(\omega)\Big(F_{00}^*(\omega+\Omega) + F_{00}^*(\omega-\Omega)\Big)\right] \\ &+ 2\sin\Omega t\,\mathrm{Im}\left[a_{00}b_{00}^*F_{00(\omega)}\Big(F_{00}^*(\omega+\Omega) - F_{00}^*(\omega-\Omega)\Big)\right] \\ &+ 2\cos\Omega t\,\mathrm{Re}\left[a_{01}b_{01}^*F_{01}(\omega)\Big(F_{01}^*(\omega+\Omega) + F_{01}^*(\omega-\Omega)\Big)\right] \\ &+ 2\sin\Omega t\,\mathrm{Im}\left[a_{01}b_{01}^*F_{01}(\omega)\Big(F_{01}^*(\omega+\Omega) - F_{01}^*(\omega-\Omega)\Big)\right] + (2\Omega\&\text{DC terms}) \end{aligned} \tag{3.21}$$

However, we need to fix some conditions of the complex reflection coefficients in order to retrieve the information we want. Assuming the cavity is impedance matched and locked to the fundamental mode, $F_{00}(\omega) = 0$ and we only have the last two terms. If the LG_{01} sidebands are both reflected by the cavity together with their carrier, $F_{01}(\omega) = F_{01}(\omega+\Omega) = F_{01}(\omega-\Omega) = 1$, then only the cosine term remains. Retrieving information on both degrees of freedom using this approach is unfeasible, given that through demodulation we would be able to obtain only one signal containing both β and γ without the possibility of decoupling them. On the contrary, if we break the sideband symmetry by assuming that one of the sidebands is resonant inside the cavity together with the fundamental mode, we can I/Q demodulate the PD signal and obtain two error signals containing the information needed. Assuming then that $F_{01}(\omega+\Omega) = 0$ and

$F_{01}(\omega) = F_{01}(\omega - \Omega) = 1$, the photocurrent is:

$$\begin{aligned}\frac{I_{ref}}{I_0} =& 2\cos\Omega t \,\mathrm{Re}\left[a_{01}b_{01}^*\right] - 2\sin\Omega t\,\mathrm{Im}\left[a_{01}b_{01}^*\right] + (2\Omega\&\mathrm{DC\ terms}) = \\ & \left[(\gamma m_G + \beta m_B)\cos(\Omega t - \Delta\psi) + (\beta m_G - \gamma m_B)\sin(\Omega t - \Delta\psi)\right] + (2\Omega\&\mathrm{DC\ terms})\end{aligned} \tag{3.22}$$

In this scenario, we encounter two quantities—one multiplied by a cosine and the other by a sine. To extract γ and β by demodulation, one should know the phase $\Delta\psi$, which represents the Gouy phase associated with the generated LG_{01} mode due to the EOL, and depends on the crystal's position along the beam, as discussed earlier. In a practical optical setup, determining this phase term precisely a priori is challenging and a method is needed to tune the demodulation angle so as to compensate for this phase. In the upcoming section, we'll explore the process of demodulating these signals using I/Q demodulation. This will enable us to derive two error signals that convey information about the mismatch parameters.

3.1.3 I/Q Error Signals

In order to retrieve the error signals for the mismatch parameters we perform I/Q demodulation. This method is often used in RF applications. The terminology I/Q stands for *in-phase* and *quadrature-phase* and it refers to two channels that are 90 degrees out of phase with each other. A sinusoidal RF signal can be represented as a phasor, formed by a rotating vector characterized by an amplitude A, frequency ω, and an initial phase ϕ_0:

$$y(t) = A\sin(\omega t + \phi_0) \tag{3.23}$$

which can be rewritten as:

$$y(t) = A\cos(\phi_0)\sin(\omega t) + A\sin(\phi_0)\cos(\omega t) = I\sin(\omega t) + Q\cos(\omega t) \tag{3.24}$$

where $I = A\cos(\phi_0)$ and $Q = A\sin(\phi_0)$. We can easily calculate the magnitude and phase of $y(t)$ by using I and Q:

$$A = \sqrt{I^2 + Q^2} \tag{3.25}$$

$$\phi_0 = \arctan\frac{Q}{I} \tag{3.26}$$

Now, let's consider multiplying the signal by a LO with the same frequency. In particular, multiplying the signal by both the in-phase ($\sin(\omega t)$) and quadrature ($\cos(\omega t)$) components of the LO. Since in reality, it is not always possible to have the phase of the LO equal to that of the RF signal, we will also add a phase φ. We obtain:

$$Ch_1 = y(t)\cdot\cos(\omega t + \varphi) = Q\cos\varphi - I\sin\varphi + (2\omega t\ \mathrm{terms}) \tag{3.27}$$

$$Ch_2 = y(t) \cdot \sin(\omega t + \varphi) = Q \sin\varphi + I \cos\varphi + (2\omega t \text{ terms}) \tag{3.28}$$

As we can see, the two quantities Ch_1 and $_2$ are just a rotation of I and Q. In this context, if we are able to adjust the phase φ of the LO, then we can align s_1 with Q and s_2 with I. This can also be written in matrix form as:

$$\begin{pmatrix} Q \\ I \end{pmatrix} = \begin{pmatrix} \cos\varphi & \sin\varphi \\ -\sin\varphi & \cos\varphi \end{pmatrix} \begin{pmatrix} Ch_1 \\ Ch_2 \end{pmatrix} \tag{3.29}$$

Let us now apply this to the photocurrent measured by the PD in reflection in equation (3.22). The demodulation setup includes a photodetector in reflection and two electronic chains intended to split and demodulate the signal. Each signal undergoes mixing with the LO, with one in-phase and the other in quadrature, followed by passage through two low-pass filters. While the two electronic chains ideally possess equal gains, real-world conditions may lead to a slight imbalance. Consequently, this can result in potentially different gains, c_1 and c_2 and an additional phase delay, $\delta\phi$, between the two LOs. However, for simplicity let us for now assume equal unity gain and no phase delay in the two electronic chains. Then, channels Ch_1 and Ch_2 can be written as:

$$\begin{aligned} Ch_1 =& \frac{I_{ref}}{I_0} \cdot \cos(\Omega t + \phi_0) = \\ & \Big[(\gamma m_G + \beta m_B)\cos(\Delta\psi + \phi_0) - (\beta m_G - \gamma m_B)\sin(\Delta\psi + \phi_0)\Big] \end{aligned} \tag{3.30}$$

$$\begin{aligned} Ch_2 =& \frac{I_{ref}}{I_0} \cdot \sin(\Omega t + \phi_0) = \\ & \Big[(\gamma m_G + \beta m_B)\sin(\Delta\psi + \phi_0) + (\beta m_G - \gamma m_B)\cos(\Delta\psi + \phi_0)\Big] \end{aligned} \tag{3.31}$$

Here, we retained only the DC components, as we subsequently applied low-pass filters to the signals post-mixing. The Q and I signals, therefore are:

$$Q = \gamma m_G + \beta m_B \tag{3.32}$$

$$I = \beta m_G - \gamma m_B \tag{3.33}$$

Additionally, we can define an angle α such that $m_B = \sin\alpha$ and $m_G = \cos\alpha$ (except for a global scaling factor that can be incorporated in the gains). This means that the coefficients γ and β are, in turn, a rotation of I and Q signals. We can rewrite this in matricial form:

$$\begin{aligned} \begin{pmatrix} Ch_1 \\ Ch_2 \end{pmatrix} &= \begin{pmatrix} \cos(\Delta\psi + \phi_0) & -\sin(\Delta\psi + \phi_0) \\ \sin(\Delta\psi + \phi_0) & \cos(\Delta\psi + \phi_0) \end{pmatrix} \begin{pmatrix} Q \\ I \end{pmatrix} = \\ & \begin{pmatrix} \cos(\Delta\psi + \alpha + \phi_0) & -\sin(\Delta\psi + \alpha + \phi_0) \\ \sin(\Delta\psi + \alpha + \phi_0) & \cos(\Delta\psi + \alpha + \phi_0) \end{pmatrix} \begin{pmatrix} \beta \\ \gamma \end{pmatrix} \end{aligned} \tag{3.34}$$

Therefore, by just inverting the matrix, we are able to obtain the signals for β and γ.

$$\begin{pmatrix}\beta\\ \gamma\end{pmatrix} = \begin{pmatrix}\cos(\Delta\psi+\alpha+\phi_0) & \sin(\Delta\psi+\alpha+\phi_0)\\ -\sin(\Delta\psi+\alpha+\phi_0) & \cos(\Delta\psi+\alpha+\phi_0)\end{pmatrix}\begin{pmatrix}Ch_1\\ Ch_2\end{pmatrix} \tag{3.35}$$

Let us see now how to obtain the total rotation angle $\theta = \Delta\psi + \alpha + \phi_0$ which is needed to either add an offset to ϕ_0 or rotate the data in post-processing, so as to obtain error signals aligned with β and γ.

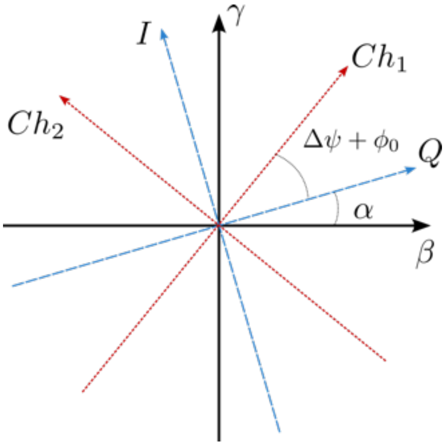

Figure 3.2: The orientation of the Ch_1-Ch_2 space is rotated by an angle of $\Delta\psi+\phi_0$ with respect to the I-Q space. Simultaneously, the I-Q space is rotated by an angle of α with respect to the γ-β space.

One way of measuring the total angle θ, exploiting a well-modeled mode matching telescope, is to adjust its lenses so as to take a series of measurements along the isolines of β and the isolines of γ, that is where β and γ are constant respectively. Let us review the equations for the signals we actually measure, which are Ch_1 and Ch_2 in equation (3.34). We have:

$$Ch_1 = \beta\cos\theta - \gamma\sin\theta \tag{3.36}$$

$$Ch_2 = \beta\sin\theta + \gamma\cos\theta \tag{3.37}$$

Suppose we are moving on an isoline of β, then only γ changes and we can write Ch_2 in terms of Ch_1 obtaining:

$$Ch_{2,\beta} = -Ch_1\frac{\cos\theta}{\sin\theta} + \frac{\beta}{\sin\theta} \tag{3.38}$$

A similar goes on the isoline of γ:

$$Ch_{2,\gamma} = Ch_1\frac{\sin\theta}{\cos\theta} + \frac{\gamma}{\cos\theta} \tag{3.39}$$

Therefore by calculating the slope m of equation (3.39) we can retrieve the rotation angle θ as:

$$\theta = \arctan(m) \tag{3.40}$$

Let us see now how these equations change if we introduce both the scaling factors c_1 and c_2 and the phase delay $\delta\phi$. In this case, the matrix form in (3.34) becomes:

$$\begin{pmatrix} Ch_1 \\ Ch_2 \end{pmatrix} = \begin{pmatrix} c_1 & 0 \\ 0 & c_2 \end{pmatrix} \begin{pmatrix} \cos(\theta) & -\sin(\theta) \\ \sin(\theta+\delta\phi) & \cos(\theta+\delta\phi) \end{pmatrix} \begin{pmatrix} \beta \\ \gamma \end{pmatrix} \tag{3.41}$$

By inverting the matrices we can write β and γ as functions of Ch_1 and Ch_2:

$$\begin{pmatrix} \beta \\ \gamma \end{pmatrix} = \frac{1}{\cos(\delta\phi)} \begin{pmatrix} \cos(\theta+\delta\phi) & \sin(\theta) \\ -\sin(\theta+\delta\phi) & \cos(\theta) \end{pmatrix} \begin{pmatrix} 1/c_1 & 0 \\ 0 & 1/c_2 \end{pmatrix} \begin{pmatrix} Ch_1 \\ Ch_2 \end{pmatrix} \tag{3.42}$$

where we assumed $|\delta\phi| < \pi/2$.

The equations of the isolines (3.39) and (3.38) become, respectively:

$$Ch_{2,\beta} = -\frac{c_2}{c_1}\frac{\cos(\theta+\delta\phi)}{\sin\theta} Ch_{1,\beta} + c_2\beta\frac{\cos\delta\phi}{\sin\theta} \tag{3.43}$$

$$Ch_{2,\gamma} = \frac{c_2}{c_1}\frac{\sin(\theta+\delta\phi)}{\cos\theta} Ch_{1,\gamma} + c_2\gamma\frac{\cos\delta\phi}{\cos\theta} \tag{3.44}$$

If $\delta\phi \simeq 0$ and $c_2/c_1 \simeq 1$, we can still approximately find the angle of rotation from the slope as in equation (3.40). Otherwise, other analysis methods are necessary, for example by acquiring the channels for different values of mode-matching and by comparing the experimental data with the theoretical ones.

Recalling that $\theta = \Delta\psi + \alpha + \phi_0$, it is also important to note that $\Delta\psi$ and α remain constant over time since they are optical phases. In fact, the first one depends on the position of the EOL with respect to the cavity and the second one with respect to the beam. However, the phases ϕ_0 and $\delta\phi$ may vary depending on the configuration of the electronic demodulation chain.

3.2 Electro-Optical Modulation

As already explained, the RFHM technique needs a high-frequency modulator; we use a modulator called Electro-Optical Lens. While the design of the modulator will be explained in the next chapter, here we briefly describe the electro-optical effect that is at the base of its working principle. The *electro-optical* effect is the change in the refractive index of a medium due to an external electric field. This effect has two different contributions: the linear effect, which is directly proportional to the electric field and was initially investigated by F. Pockels in 1894 [49], and the second-order effect, which is proportional to the square of the electric field and was first examined by J. Kerr in 1875 [50]. The linear effect is specific to non-centrosymmetric media, while the second-order effect can manifest in both centrosymmetric and non-centrosymmetric media. However, in the case of non-centrosymmetric media, the linear effect tends to dominate. Generally speaking, the crystals which can experience the electro-optic effect are called electro-optic crystals. The simplest linear electro-optic modulator (EOM) is the *Pockels cell*, which is made up of an electro-optic crystal with electrodes to generate a uniform electric field.

This dissertation will only focus on the discussion of the linear electro-optic effect inside an uniaxial anisotropic and non-centrosymmetric medium, specifically a lithium niobate crystal ($LiNbO_3$).

3.2.1 Pockels Effect

To describe the linear electro-optic effect, also called *Pockels effect*, let us recall some properties and notation used in crystal optics [51]. One important quantity is the *dielectric tensor* ε_{ij} which describes the dielectric properties of the medium in relation to its anisotropy. The dielectric tensor is a 3x3 matrix, and each element of the matrix represents the relationship between the electric field applied along a particular axis and the resulting polarization **P** or electric displacement **D**. In anisotropic materials, the dielectric tensor elements can be different for each axis, indicating that the material's response to an electric field varies depending on the direction of the field relative to the crystal's symmetry. Specifically (we will use the Einstein notation):

$$D_i = \varepsilon_{ij} E_j \tag{3.45}$$

The dielectric tensor is symmetric, which means we can diagonalize it, obtaining a new set of axes referred to as the principal axes:

$$\varepsilon = \begin{pmatrix} \varepsilon_x & 0 & 0 \\ 0 & \varepsilon_y & 0 \\ 0 & 0 & \varepsilon_z \end{pmatrix} \tag{3.46}$$

where ε_x, ε_y and ε_z are the principal values of the tensor. The refractive indices in the three principal axes are connected to the principal values through the vacuum permittivity ε_0 as:

$$n_i = \sqrt{\frac{\varepsilon_i}{\varepsilon_0}} \tag{3.47}$$

with $i = (x, y, z)$. In general, to describe the refractive indices of a medium associating them to the polarisation of a propagating optical radiation inside the medium we use a geometrical construction called index ellipsoid:

$$\frac{x^2}{n_x^2} + \frac{y^2}{n_y^2} + \frac{z^2}{n_z^2} = 1 \tag{3.48}$$

where x,y and z are the cartesian principal axis. We can also write it using the *impermeability* tensor $\eta_{ij} = \varepsilon_0 \varepsilon_{ij}^{-1}$:

$$\eta_{ij} x_i x_j = 1 \tag{3.49}$$

A crystal is uniaxial, as is the case for lithium niobate, when two of the principal values are equal. In this scenario, we are referring to *birefringence* since, depending on the direction of the polarization of the light, we can experience two different refractive indices. Without loss of generality, let us assume that the x and y axes share the same refractive index, then these axes are denoted as the *ordinary* axes with a refractive index labeled n_o. The z axis, then, is designated as the *extraordinary* axis and its refractive index is labeled n_e. More generally, the extraordinary axis is also referred to as *c-axis* or *optic axis*. In Figure 3.3 it is possible to see the index ellipsoid for a uniaxial crystal. Light propagating along the c-axis can be polarized only along an ordinary axis, which means the beam will not experience birefringence. However, if the beam propagates in any other direction, birefringence will occur.

When we have an external electric field **E** the impermeability tensor changes due to the change in the distribution of charges inside the medium. This can be computed by a Taylor expansion. For the linear electro-optic effect we stop at the first order in the electric field:

$$\eta_{ij}(\mathbf{E}) \simeq \eta_{ij}(0) + r_{ijk} E_k \tag{3.50}$$

the constant r_{ijk} is the linear electro-optic (Pockels) tensor with rank 3. However, since ε_{ij} is symmetric, so must be η_{ij}, therefore the number of independent elements in r_{ijk} goes from 27 to 18. Therefore we can write it in a more compact way as a matrix of dimension (6×3), using the same notation as A. Yariv and A. P. Yeh [51], that is:

$$r_{1k} = r_{11k} \qquad r_{2k} = r_{22k} \qquad r_{3k} = r_{33k} \tag{3.51}$$

$$r_{4k} = r_{23k} = r_{32k} \qquad r_{5k} = r_{13k} = r_{31k} \qquad r_{6k} = r_{12k} = r_{21k} \tag{3.52}$$

The index ellipsoid will change accordingly to the new impermeability tensor as:

$$\eta_{ij}(\mathbf{E}) x_i x_j = 1 \tag{3.53}$$

From the electro-optic tensor, we can understand why only non-centrosymmetric media can experience the Pockels effect. Suppose that we have a centrosymmetric medium. Then if we apply the inversion operation which transforms (x, y, z) in $(-x, -y, -z)$, the electro-optic

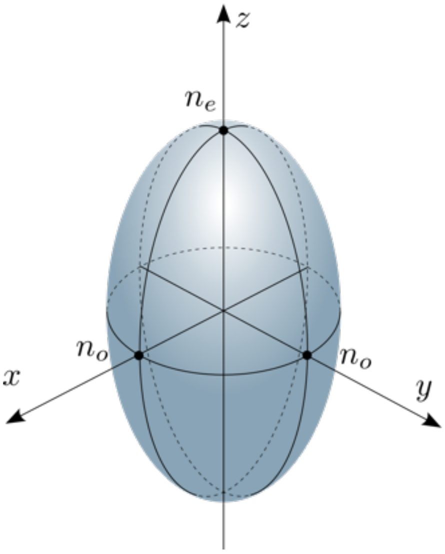

Figure 3.3: Index ellipsoid for a uniaxial crystal. In the xy plane (ordinary axes) the index of refraction is n_o, in the z axis (extraordinary axis, c-axis, optic axis) the index of refraction is n_e.

tensor will transform as $r'_{ijk} = -r_{ijk}$. However, centrosymmetric mediums are characterized by inversion symmetry so the tensor should remain invariant under the inversion operation. This means the only possibility is if $r_{ijk} = 0$.

Let us now describe the Pockels effect in the case of a lithium niobate ($LiNbO_3$) crystal. $LiNbO_3$ is part of the $3m$ point group [52] and its electro-optic coefficients are:

$$r_{ik} = \begin{pmatrix} 0 & -r_{22} & r_{13} \\ 0 & r_{22} & r_{13} \\ 0 & 0 & r_{33} \\ 0 & r_{51} & 0 \\ r_{51} & 0 & 0 \\ -r_{22} & 0 & 0 \end{pmatrix} \tag{3.54}$$

If the external electric field is on the c-axis,which corresponds to the z-axis in this description, $\mathbf{E} = (0, 0, E_z)$, then the index ellipsoid equation (3.53) becomes:

$$x^2 \left(\frac{1}{n_o^2} + r_{13} E_z \right) + y^2 \left(\frac{1}{n_o^2} + r_{13} E_z \right) + z^2 \left(\frac{1}{n_e^2} + r_{33} E_z \right) = 1 \tag{3.55}$$

Usually, the terms $r_{13}E_z$ and $r_{33}E_z$ are small compared to $n_{o,e}^{-2}$ meaning a weak nonlinearity induced by the Pockels effect. Therefore we can approximate the new refractive indices along the three principal axes as:

$$n_x = n_o - \frac{1}{2} n_o^3 r_{13} E_z \tag{3.56}$$

$$n_y = n_o - \frac{1}{2} n_o^3 r_{13} E_z \tag{3.57}$$

$$n_z = n_e - \frac{1}{2} n_e^3 r_{33} E_z \tag{3.58}$$

The values for these electro-optic coefficients are slightly different in the case of low and high frequencies of the electric field. For low frequency (from DC to audio range) $r_{13} \simeq 10$ pm/V, $r_{33} \simeq 32.2$ pm/V while for high frequency $r_{13} \simeq 8.6$ pm/V and $r_{33} \simeq 30.8$ pm/V [51].

Supposing a beam enters inside the medium along the x-axis and is polarized along the z-axis. The beam will experience a phase shift ϕ calculated as the integral of the refractive index along the crystal:

$$\phi = \frac{2\pi}{\lambda} \int_0^L n_z dx \tag{3.59}$$

where λ is the wavelength of the beam and L is the length of the crystal. Using equation (3.58) and writing $E_z = V/d$ where d is the crystal thickness, we obtain:

$$\phi(V) = \phi_0 - \frac{\pi}{\lambda} \frac{n_e^3 r_{33} L}{d} V \tag{3.60}$$

When we introduce periodic phase modulation through an oscillating voltage, we can produce sidebands in the light beam. If we assume that the oscillating voltage has a frequency of Ω and amplitude V_0, the phase can be expressed as follows:

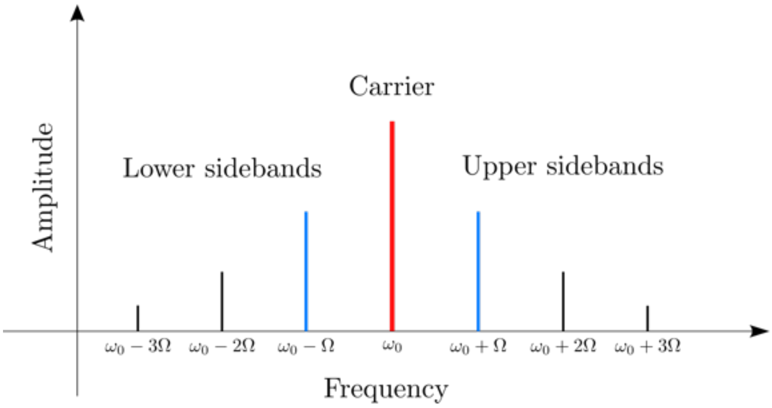

Figure 3.4: Graphical representation of the carrier and its sidebands. The blue ones are the first-order sidebands at frequency $\omega_0 \pm \Omega$. Usually, the other sidebands are negligible.

$$\phi(t) = \phi_0 - m \sin(\Omega t) \tag{3.61}$$

Here, we define $m = \pi n_e^3 r_{33} L V_0/(\lambda d)$ as the modulation depth. Therefore after the crystal we can write the beam field $u_{out}(x,t)$ as:

$$u_{out}(x,t) = u_0(x) e^{i(\omega_0 t + \phi_0 - m \sin(\Omega t))} \tag{3.62}$$

where ω is the beam frequency. For small modulation depths, $m < 1$, we can expand the exponential using the Jacobi-Anger expansion which is:

$$e^{\pm\beta\sin(\theta)} = \sum_{n=-\infty}^{n=+\infty} J_n(\beta)e^{\pm in\theta} = J_0(\beta) + \sum_{n=1}^{n=+\infty} J_n(\beta)e^{\pm in\theta} + \sum_{n=1}^{n=+\infty} (-1)^n J_n(\beta)e^{\mp in\theta} \tag{3.63}$$

where $J_n(\beta)$ are the Bessel functions. Then we can rewrite equation (3.62) as.

$$u_{out}(x,t) = u_0(x)e^{i(\omega_0 t+\phi_0)}\left(J_0(m) + \sum_{n=1}^{n=+\infty} J_n(m)e^{-in\Omega t} + \sum_{n=1}^{n=+\infty} (-1)^n J_n(m)e^{+in\Omega t}\right) \tag{3.64}$$

From this equation, we observe that an oscillating modulation at the frequency Ω creates sidebands around the main frequency, referred to as the carrier frequency or simply carrier for brevity (see Figure 3.4). Specifically, the carrier is located at the frequency ω_0, while the sidebands appear at frequencies $\omega_0 \pm n\Omega$. If we consider only the first-order effects $n = 1$, the sidebands occur at frequencies $\omega_0 \pm \Omega$.

Chapter 4

Experimental Setup

In this chapter, we will take a closer look at the experimental setup for generating the LG_{01} sidebands and acquiring the values of the mismatch parameters γ and β.

In the first part (4.1), we will present the details of designing and simulating the EOL through Comsol Multiphysics software. Our focus centers on two prototypes: one functioning as a spherical lens and the other as an astigmatic lens with opposite focal lengths on the two axes. To restore spherical behavior in the latter configuration, a cylindrical telescope, acting as a mode converter is needed.

In section 4.2, we will outline the layout of the optical test bench, focusing on two essential components: the mode converter and the mode-matching telescope. The mode-matching telescope is fundamental to the technique since it is used to create controlled mismatch and map out the theoretical isolines of γ and β.

Lastly, in section 4.3, we'll provide a detailed overview of the electronic setup. This section includes the electronics for Pound-Drever-Hall (PDH) locking, EOL modulation, and the extraction of mismatch parameters from the signal reflected from the cavity through I/Q demodulation.

4.1 Electro-Optical Lens

In this section, we will outline the designs of the EOL, composed of a lithium niobate crystal surrounded by electrodes to leverage the electro-optic effect. As we have seen in the previous chapter, through the electro-optic effect, the beam undergoes a phase shift, which is calculated as the integral of the electric field along the crystal as shown in equation (3.59). To achieve a lens effect, it is necessary to introduce a different phase shift at various points on the transverse plane. This variation can be attained by shaping the electrodes to create a particular distribution of the electric field. We conducted Comsol Multiphysics simulations to determine the optimal configuration and shape for the electrodes to achieve the desired optical effects. Two distinct

EOLs designs were considered: EOL_{PD} operates as a spherical lens, while EOL_{FL}[53] functions as a lens with opposite focal lengths on the two axes. The addition of a cylindrical telescope is crucial to restore spherical behavior in the latter case. The choice of two designs arises from their individual characteristics. EOL_{PD}, inherently behaving as a spherical lens, requires no additional optical elements. However, it features a small effect that can be more difficult to measure and is more sensitive to design and construction imperfections. On the other hand, EOL_{FL} exhibits a more solid design and a more pronounced effect but needs the addition of a mode converter to restore spherical behavior.

The initial concept for the EOL_{FL} design was proposed by P. Fulda and M. Diaz-Ortiz from the LIGO group of the University of Florida [53][54].

4.1.1 Design

Figure 4.1 shows the two distinct designs, both composed of a lithium niobate crystal with dimensions $(x, y, z) = (5, 8, 20)$mm and copper electrodes on the yz faces. The difference lies in the electrode shapes:

- EOL_{FL}: Three pairs of electrodes with alternating polarity, equidistant from each other, share the same height (0.5mm) and width (2mm). However, the lateral electrodes measure 1cm in length, while the central ones measure 7mm. This EOL behaves as a particular astigmatic lens. It acts on the two transversal planes as two lenses with inverse focal lengths, which creates a phase shift of π between the two planes. In order to regain back this π phase and, therefore, regain the spherical behavior, a cylindrical telescope is used, also known as mode converter telescope (MCT) which will be explained at the end of this section.
- EOL_{PD}: Comprising a single pair of electrodes with one flat side and the other side curved, featuring a radius of curvature of 1.3cm. The height is 0.5mm and the length is 6mm.

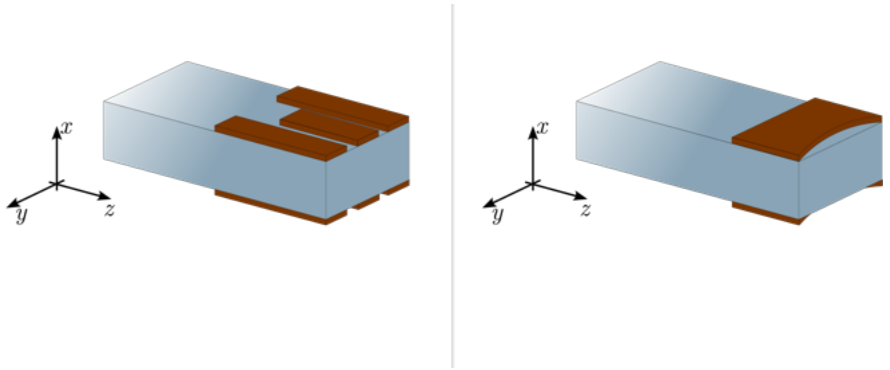

Figure 4.1: The two different designs for the EOL. On the left the astigmatic EOL_{FL}, while on the right the spherical one, EOL_{PD}. The electrodes are colored in brown.

From the simulations, it has been observed that the $\mathrm{EOL_{PD}}$ design is very sensitive to variations in its design parameters, which, if not perfectly tuned, easily lead to the final lens being highly astigmatic rather than spherical [46]. When studying the $\mathrm{EOL_{FL}}$, we find instead that it is much easier to achieve an equal and opposite astigmatism effect along the two axes, and that the result is much more tolerant. Even considering realistic variations to the nominal design parameters the astigmatic effect remains almost unchanged, providing stability to the configuration. This sensitivity becomes a crucial consideration during the construction phase, where small error margins are significant. There is another substantial difference between the two EOLs. In general, the adaptive lens should not introduce an average phase change to the beam so that, once polarized with an RF voltage, the EOL will inject sidebands in the LG_{10} mode but not in the LG_{00} one. However, the $\mathrm{EOL_{PD}}$ design as presented here does not have enough DoF in the design to be optimized in this respect. It serves as the first prototype for a more complex project where this feature is provided through the use of another pair of electrodes placed just before the current ones, which does not provide curvature but is solely meant to eliminate this additional phase. On the other hand, $\mathrm{EOL_{FL}}$, by having three pairs of electrodes with alternating polarity, can be optimized to maintain an overall zero-phase modulation. In this specific design, achieving this was done by changing the length of the central electrode compared to the lateral electrodes. Moreover, the length of the lateral electrodes did not substantially affect the final value, hence a value of 1cm was chosen for simplicity. On the other hand, the length of the $\mathrm{EOL_{PD}}$ electrode was decided to minimize the residual electric field at the input of the crystal.

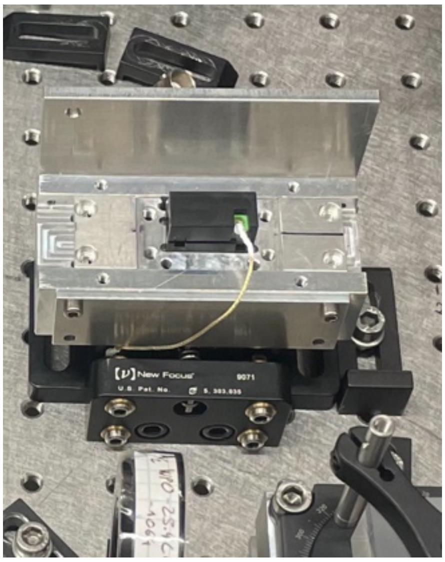

Figure 4.2: EOL placement. The crystal is inside the black case, which is positioned on top of a metallic base.

The crystal and the electrodes are situated within a plastic case, which ensures relative alignment; in turn, this case is positioned onto a metallic base featuring screws for precise adjustments and the required electric connections for the electrodes, as shown in Figure 4.2. To clamp the crystal within the plastic case, a thin metallic plate is employed and securely fastened to the foundational support. Moreover, a metallic box covers the EOL to provide well-defined boundary conditions for the electric field in the region of the crystal, and to contain the RF electromagnetic field preventing it from affecting the nearby electronic setup. This multi-layered assembly ensures the stability and accurate positioning of the crystal, providing a robust structure for its functionality.

Both EOLs were built as shown in Figures 4.3 and 4.4. In the construction of the plastic housing for the lens, we implemented a design allowing secure placement for both the crystal and electrodes. This design ensures that these components are securely fitted inside the box, without the need for glue or adhesives.

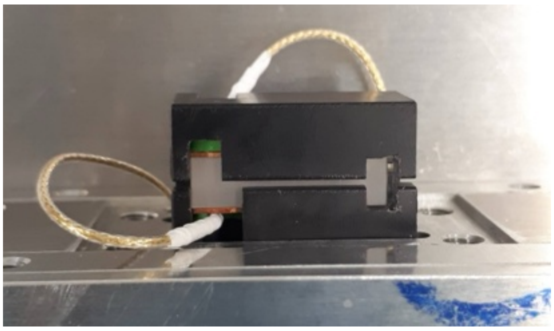

Figure 4.3: Photo of the final $\mathrm{EOL}_{\mathrm{PD}}$ inside the plastic case in black (the green part is a plastic spacer to fill a gap). The electrodes are soldered to a connector using coaxial cables. Specifically, one electrode is connected to the ground, and the other electrode has the core connected to the plug, while the shield is connected to the ground.

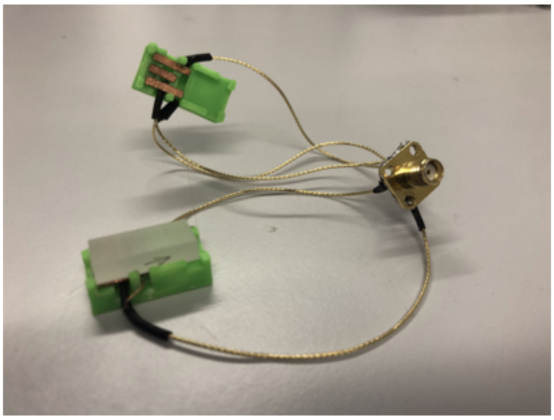

Figure 4.4: Photo of the final $\mathrm{EOL}_{\mathrm{FL}}$ inside the plastic case in green. The electrodes are soldered to a connector using coaxial cables. Specifically, they are alternatively connected to the ground and to the plug. The cables connected to the plug have the shield connected to the ground.

Mode Converter Telescope

As stated before, in order to obtain a spherical behavior in the variation of the wavefront curvature induced by $\mathrm{EOL}_{\mathrm{FL}}$, we need another optical element known as Mode Converter Telescope (MCT)[37][36]. To simplify the description, we will consider a static scenario, where there is no electro-optical modulation and, consequently, no sidebands.

Mathematically, the astigmatism introduced by the $\mathrm{EOL}_{\mathrm{FL}}$ gives rise to an additional HG_{11} mode rotated at 45°. This mode can be written in terms of the HG_{nm} modes using the conversion rule (2.20) as:

$$HG_{11}^{45} = \frac{HG_{20} - HG_{02}}{\sqrt{2}} \tag{4.1}$$

Using the Hermite-Gauss modes HG_{nm} we can write the astigmatic beam ψ_{eol} after the EOL as:

$$\begin{aligned}\psi_{eol} \simeq HG_{00}(\tilde{q}) + &\frac{\epsilon_c}{\sqrt{2}}\left(HG_{20}(\tilde{q}) + HG_{02}(\tilde{q})\right) + \\ &+ \frac{\epsilon_d}{\sqrt{2}}\left(HG_{20}(\tilde{q}) - HG_{02}(\tilde{q})\right)\end{aligned} \tag{4.2}$$

Where we define $\tilde{q}$ as the complex parameter, calculated using the average waist size and position of the astigmatic beam, while ϵ_c and ϵ_d represent the common and differential mismatches on the x and y axes [55]:

$$\epsilon_c = \frac{\epsilon_x + \epsilon_y}{2} \tag{4.3}$$

$$\epsilon_d = \frac{\epsilon_x - \epsilon_y}{2} \tag{4.4}$$

In particular, since for construction $\mathrm{EOL}_{\mathrm{FL}}$ has equal but opposite focal lengths on the two axes, the common mismatch is approximately zero.

From the conversion rules in equation (2.18) we know that the LG_{01} mode can be written as:

$$LG_{01} = \frac{HG_{20} + HG_{02}}{\sqrt{2}} \tag{4.5}$$

Therefore, to convert the differential part of equation (4.2) into an LG_{01} we need to change the relative sign between the HG_{02} and HG_{20} modes. This can be achieved by accumulating a π Gouy phase between the two axes. In order to do this we can use a particular type of MCT, which is the $\pi/2$ MCT. This telescope is composed of two cylindrical lenses and, under specific conditions, it accumulates $\pi/2$ more Gouy phase on the focusing axis than on the other axis. For second-order HG modes, this means that the total phase difference between the two axes is π.

To design the $\pi/2$ MCT, we need to fulfill two main requirements:

1. The mean waist between the two transversal axes should be positioned at the center of the mode converter.
2. Depending on the focal length f_{cyl} of the lenses, we need to satisfy conditions on the value

of the mean waist w_0^{MC} and of the length l^{MC} of the telescope:

These relations arise by imposing the π difference in the Gouy phase between HG_{02} and HG_{20} and ensuring that the beam after the mode converter has no astigmatism ($q_x = q_y$). Using the ABCD matrices, we can derive the requirements for the telescope design:

$$w_0^{MC} = \sqrt{\left(1 + \frac{1}{\sqrt{2}}\right) \frac{\lambda f_{cyl}}{\pi}} \tag{4.6}$$

$$l^{MC} = \sqrt{2} f_{cyl} \tag{4.7}$$

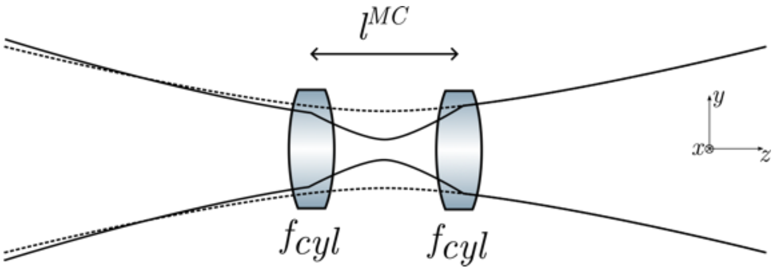

Figure 4.5: Sketch of a $\pi/2$ mode converter telescope. The dashed and solid curves denote the Gaussian beams in the xz and yz planes. Before the MCT the beam presents astigmatism on the two transverse axes. The MCT operates only on the beam in the axis aligned with the cylindrical lenses' axis.

4.1.2 Comsol Simulations

To explore the effect of different design parameters on the EOL performance, we employed Comsol Multiphysics, a finite element analysis software. The simulation calculates the electric field along the crystal due to the polarized electrodes. From this, we are able to calculate the variation in the refractive index along the optical axis and, eventually, of the optical path on the output face of the EOL, and therefore the phase shift experienced by the beam in different positions in the transverse plane. Specifically, in the $\mathrm{EOL_{PD}}$ case, our goal is to observe a phase shift with a spherical shape (at least in the central region), while in the $\mathrm{EOL_{FL}}$ case, we aim for a phase shift profile resembling a saddle shape. To set up and perform the simulations, we used the same methodology for both configurations and we implemented the same procedure outlined in [46]:

Geometry: the geometry of the entire system includes the electrodes, the crystal, an air-filled enclosure simulating the metallic box used for shielding the EOL and the metallic plate positioned within the enclosure. The metallic box eternal surfaces and the metallic plate are set to zero potential. The geometry of the electrodes for both EOLs follows the design shown in the previous section in Figure 4.1, while the parameters for the crystal, the box and the plate are listed in Table 4.6. Because this geometry exhibits symmetry with respect to the xz plane, simulations can be conducted on only half of it. The illustrated half geometry is presented in Figure 4.7. We opted not to include the plastic case in the simulations to avoid unnecessary geometric complexity. Since the plastic material is non-conductive, its exclusion should minimally affect the final results. However, the inclusion of the metallic plate is essential, in fact, as it is possible to see in Figure 4.7, the EOL is not situated at the center of the metallic box. Introducing an additional metallic boundary at the same distance as the base of the box contributes to making the electric field distribution more symmetric and controllable.

Parameter	Value
L_{cst}	$2[cm]$
W_{cst}	$0.8[cm]$
H_{cst}	$0.5[cm]$

Parameter	Value
L_{box}	$5.4[cm]$
W_{box}	$3.25[cm]$
H_{box}	$3.5[cm]$

Parameter	Value
L_{plt}	$4[cm]$
W_{plt}	$2[cm]$
H_{plt}	$0.1[cm]$

Table 4.6: Values of the fixed parameters of the crystal (*cst*, left), of the shielding box (*box*, center) and of the metallic plate (*plt*, right).

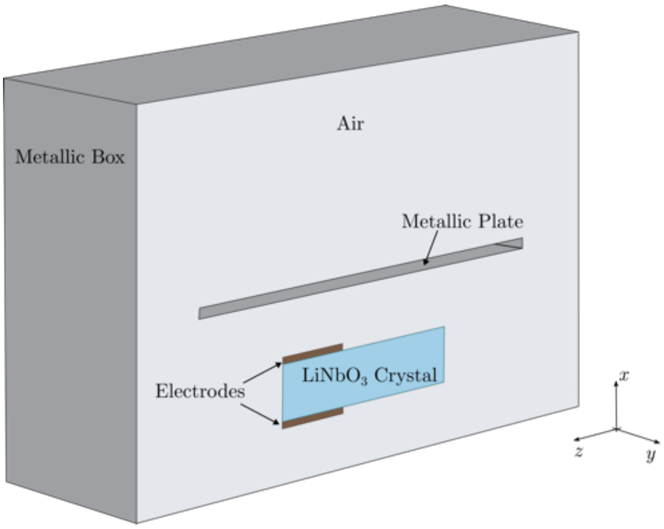

Figure 4.7: Geometry of half elements simulated in Comsol. In this figure, the transversal section of the elements is shown. In grey the metallic box and plate. In light blue the lithium niobate crystal and in brown the copper electrodes. The light grey part is the air inside the shielding box.

Material and Electrostatic: The definition of materials and electrostatic properties for each element involves configuring the crystal as lithium niobate, the electrodes as copper, and the surrounding box as air. The c-axis of the lithium niobate is set to be along the x-axis to maximize the electro-optic effect as described in section 3.2 (note that in that section we defined the c-axis on the z-axis: here we are just using a different orientation of the cartesian axis). The electrostatic properties are also established, with the external boundaries of the box set at ground, and the electrodes at a constant and uniform electric potential. The electrodes' potential is set to be constant and symmetric with respect to the external boundaries of the box, which are at the ground. This implies that we polarized the electrodes with $+V$ on one side and $-V$ on the other. In particular, to have an idea of the order of magnitude achievable during operation, we decided to work in the range we can obtain in the laboratory which is ±200V. However, since we have only one RF amplifier, we are only able to polarize one group of electrodes at +400V while setting the others at ground. At the end of the presentation of both configurations, we will see how this changes the results for both EOLs.

Mesh: To solve physics simulations, Comsol uses the Finite Element Method (FEM). This numerical technique solves problems by dividing a complex structure into smaller and simpler domains, forming the so-called *mesh*. Differential equations are solved numerically by sampling the domain at each element, calculating the derivatives, updating the field values and repeating the process iteratively until convergence is achieved. A fine mesh captures more details but may require more computational resources, while a coarse mesh simplifies the problem but may result in less accurate solutions. Balancing the mesh density is a key aspect of using the FEM effectively. An example of mesh is shown in Figure 4.8.

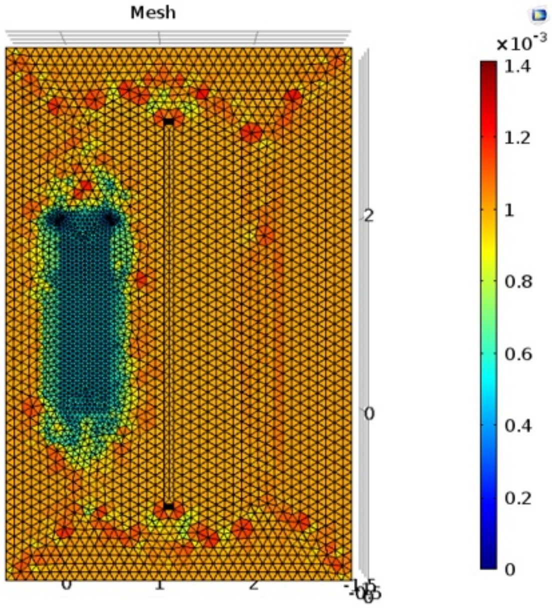

Figure 4.8: An example of mesh for our geometry. Since we are interested in the behavior of the crystal refractive index due to the electric field, the mesh on the crystal needs to be as fine as possible, while the one on the box can be coarser since we don't expect rapid variations of the field. The color bar refers to the dimensions of the domains.

Electrostatic Stationary Study Model: The electrostatic stationary study model was established to analyze the behavior of the optical element when the electrodes are polarized. Specifically, our simulation provides the electric field distribution along the crystal, $E_x(y, z)$, from which we can recover the variation in the optical path length (OPL). By applying equation (3.58) we can calculate the refractive index change $\Delta n_x = n_e - n_x$ resulting from the presence of the electric field. Since our primary interest lies in the variation of the optical path OPL. We integrate Δn_x along the length of the EOL, which, in our case, corresponds to the z-axis. This model allows us to understand how changes in the geometrical parameters of the electrodes affected the refractive index of the crystal and therefore the optical path of the beam. It is also important to note that these simulations were conducted using a static electric field. However, the EOL is planned to operate with an RF electric field.

Result Plots: The results are visualized through plots generated from the simulations. These plots provide insights into the changes in the OPL of the beam across the plane transverse to the propagation direction, based on variations in electrode parameters, as described above. Since the beam is centered within the crystal with a waist size of approximately 200μm, we can limit the analysis to a small region around the center. Specifically, we aim to maintain consistent concavity (a nearly spherical profile for $\mathrm{EOL_{PD}}$ and saddle profile for $\mathrm{EOL_{FL}}$) within a range of 0.05cm from the center. This can be visualized using a plot of the OPL change along the transversal axes, namely the x-axis and y-axis, as shown in Figure 4.9. We decided arbitrarily to align the centers of both x and y axes at 0.25cm. Extracting the optical path from these axes allows us to calculate the focal length of the lens as the curvature of the OPL in a small range of the crystal's center. Since we are working in a range where we have a small OPL variation, we can perform a quadratic fit on the OPL data between the extreme points of the range for both axes, i.e. between 0.20cm and 0.25cm. The radius of curvature can be calculated as the radius of the osculating circle of the parabola at $x_0, y_0 = 0.25$, which is:

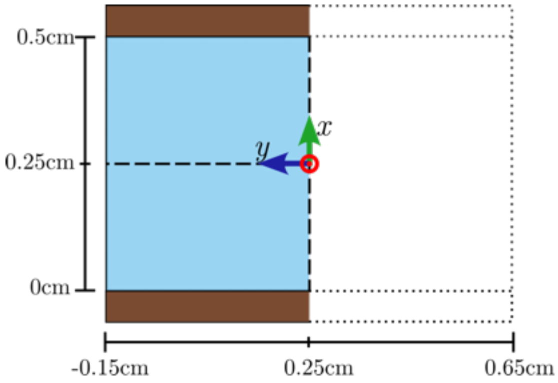

Figure 4.9: Output face of the EOL. Due to the symmetry of the system, we can restrict ourselves to simulate only half geometry, which corresponds to the colored part (light blue for the crystal and brown for the electrodes). The other half is shown with dotted lines. The dashed lines are the x and y axes in which the change in the refractive index is calculated. The center lies at 0.25cm for both axes.

$$R = \frac{\left[1 + f'(0.25)^2\right]^{3/2}}{f''(0.25)} = \frac{1}{2a} \tag{4.8}$$

where $f = a(x - 0.25)^2 + b$ is the generic parabola equation centered in 0.25.

In order to study the stability of the two configurations, we examine how the OPL evolves along the transverse planes, i.e. the xz-plane and the yz-plane. This involves calculating the optical path along two lines inside the crystal, one in the xz-plane and one in the yz-plane shifted of $0.05cm$ with respect to the crystal's center, as shown in Figure 4.10. Since we are interested in the differential effect with respect to the crystal's center, we normalize our data by subtracting the values along the line $x = y = 0$. This line is common to both planes and serves as a reference for a clearer visualization of the variations. We calculate the integral of this differential OPL variation on the two planes as:

$$OPL(z) = \int_0^z n(z)dz \tag{4.9}$$

where $n(z)$ is the refractive index on each line and z is the position inside the crystal, which is in the range $(0, 2)$cm. By plotting this quantity for each z, we are able to see how the OPL evolves along the crystal. In particular, in the $\mathrm{EOL_{PD}}$ case we expect the final value to be equal on both lines, while for $\mathrm{EOL_{FL}}$ it should be equal but with the opposite sign. As we will see below, from these plots we can understand if the final integrated effect is the result of a steady build-up along the crystal, or if it is the result of a more complex behavior, with consequences on the stability of the result with respect to the parameters variations.

In the following, we will present the results of the simulations of the two EOLs.

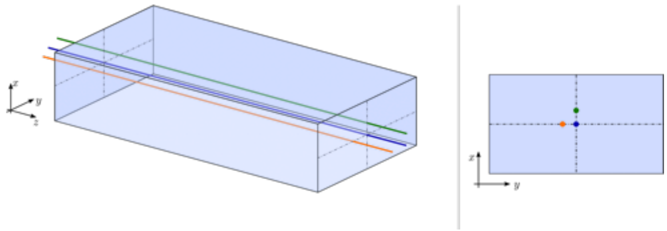

Figure 4.10: Lines where the OPL variation is calculated. The blue line crosses the center of the crystal and it is used as a reference. The orange and green lines have, respectively, an offset on y and x of $0.05cm$.

$\mathrm{EOL_{PD}}$

As explained above, the original concept of this adaptive optic element aims to emulate the effect of a spherical lens, necessitating an equivalent phase change (or OPL) along both transversal directions — namely, the x and y axes. The initial design featured the incorporation of N pair of electrodes [46], emulating the presence of N lenses. However, simulations unveiled that the final focal length does not change substantially according to the number of electrodes if one maintains the overall constraint that the optical path change must follow a spherical profile. For simplicity, we opted for a design featuring a single pair of electrodes. Simulations led us to identify the most straightforward geometry for the desired spherical behavior, which includes one flat side and one curved side, as shown in Figure 4.1. The curved side, positioned at the output of the EOL, is crucial for achieving the desired spherical behavior. On the other hand, the decision to keep the other side flat was based on simulation results indicating minimal differences between a curved and flat side. This choice simplifies the electrode manufacturing process. The parameters of these electrodes, then, are:

- Length (L_{el}): The dimension along the z-axis, indicating the size in the direction of optical propagation.
- Width (W_{el}): The dimension along the y-axis, representing the size in the horizontal plane.
- Thickness (H_{el}): The dimension along the x-axis, indicating the size perpendicular to both the y and z axes.
- Radius of Curvature (RoC): The curvature on the side aligned to the output face (on the left side in Figure 4.11) influences the optical characteristics.

The top view of the EOL with the dimensions of the electrode and the crystal is shown in Figure 4.11. In Table 4.12 are presented the optimal values of the parameters for the electrodes.

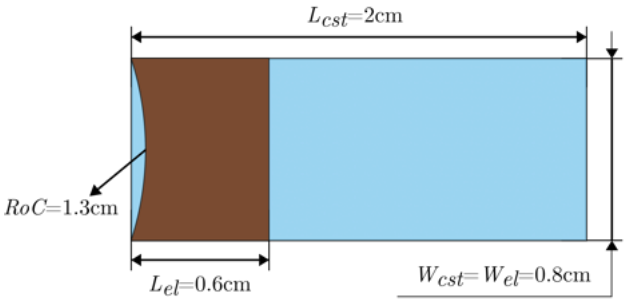

Figure 4.11: Top view of $\mathrm{EOL_{PD}}$ with the dimensions for the electrodes (brown) and the $LiNbO_3$ crystal (light blue).

Parameter	Value
L_{el}	0.6cm
W_{el}	0.8cm
H_{el}	0.05cm
RoC	1.3cm

Table 4.12: Optimal values for the electrodes (el) parameters.

Figure 4.13 shows the optical path on the two transversal axes obtained with the optimal parameters for the electrodes together with a zoom of the data on the x and y axes between 0.20 and 0.25cm. As said previously, to calculate the focal length we performed a quadratic fit of the data fixing the center of the parabola at 0.25cm. By using the fit values we calculated the focal length on both x and y obtaining $f_x = 1.51 \times 10^6$cm and $f_y = 1.58 \times 10^6$cm. Both curves have the same concavity and nearly equal focal length.

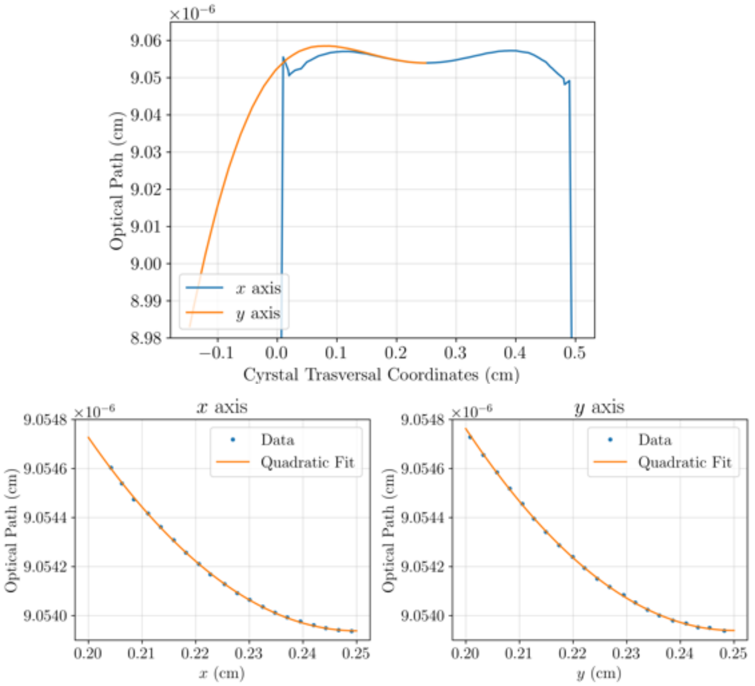

Figure 4.13: Simulation results of the OPL of EOL_{PD} along the x and y axes. The curves are plotted to have the center of the output face at 0.25 for both axes. It is important to note that, given the simulation covers only half of the crystal, the data is presented for only half of the y axis. Top: The blue curve represents the simulated data on the x axis, while the orange curve is on the y axis. The blue vertical lines are an artifact resulting from reaching the end of the crystal domain along the x-axis. Near the center, both the curves have the same curvature. Bottom: OPL simulated data (blue dots) in a region near the center of 0.05cm and quadratic fit (orange curves) on the two axes.

In Figure 4.14, we present the contour plot of the phase profile across the entire output face and a zoomed-in perspective of the central region.

It is crucial to emphasize that we were able to achieve the desired spherical behavior for nearly all the geometries studied. However, small changes in the geometric parameters can completely alter the outcome, introducing astigmatism. These small tolerances make implementing the ideal simulated results to real electrodes difficult. This problem arises from the fact that on one axis the resulting spherical effect is a subtle cumulative outcome arising from the difference between two larger effects that act in opposite directions. Consequently, even a small error in one of the initial effects can lead to a significantly different net result in percentage terms. To study this, we calculated the variation of OPL through two offset lines on the x and y axes, as explained in the previous section. Figure 4.15 shows the OPL variation along the crystal and its cumulative sum calculated with equation (4.9). It can be noted that the line with an offset along the y axis displays minimal variations along the crystal, while on the line with an

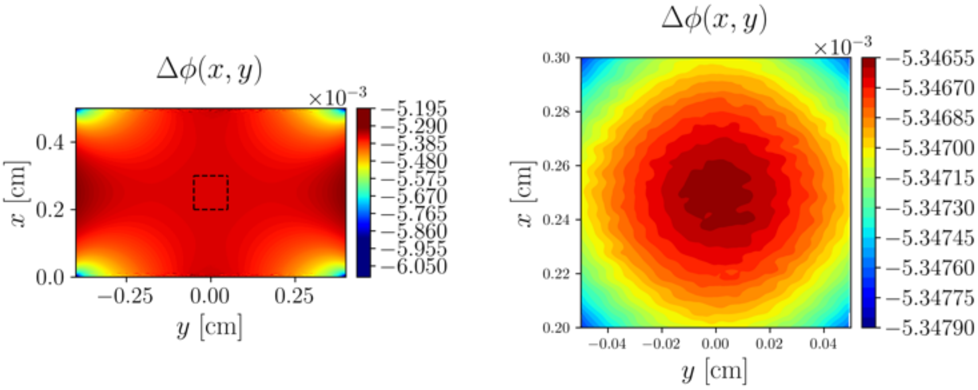

Figure 4.14: Phase profile on the output face of EOL$_{\text{PD}}$. Left: The whole output face is shown. Since the beam is centered and has a small waist inside the crystal, we are interested in the center part of the crystal, enclosed in the dotted box. Right: Zoom of the centered region of the output face. Apart from fluctuations due to the simulation mesh, we can see a clear spherical distribution of the phase profile.

offset along the x axis, substantial fluctuations are evident. From the cumulative sum of the variations shown in Figure 4.15 it is possible to see that, as expected, the cumulative effect yields the same value on both axes. However, on the y axis this effect is achieved by small contributions which all sum up in the same direction, while on the x axis the effect arises from canceling out significantly large contributions in opposite directions.

EOL$_{\text{FL}}$

The configuration for the EOL$_{\text{FL}}$ involves three longitudinal pairs of electrodes with alternating polarity. This creates an astigmatic lens in which the focal length on the two transversal axes is nearly equal, but with opposite signs. As we will see, this kind of configuration is more stable than the previous one, and therefore even small differences don't change noticeably the final effect. The parameters for the electrodes, whose values are shown in Table 4.16, are:

- Length (L^i_{el}): The dimension along the z-axis.
- Width (W_{el}): The dimension along the y-axis.
- Thickness (H_{el}): The dimension along the x-axis.
- Distance (Δy): The distance between two adjacent electrodes.

with $i = c, l$ depending if the electrode is the central or lateral one. As said in the previous section 4.1.1, the length of the central electrodes was adjusted to minimize the optical path change at the center of the crystal, i.e. to keep the average phase change as close as possible to

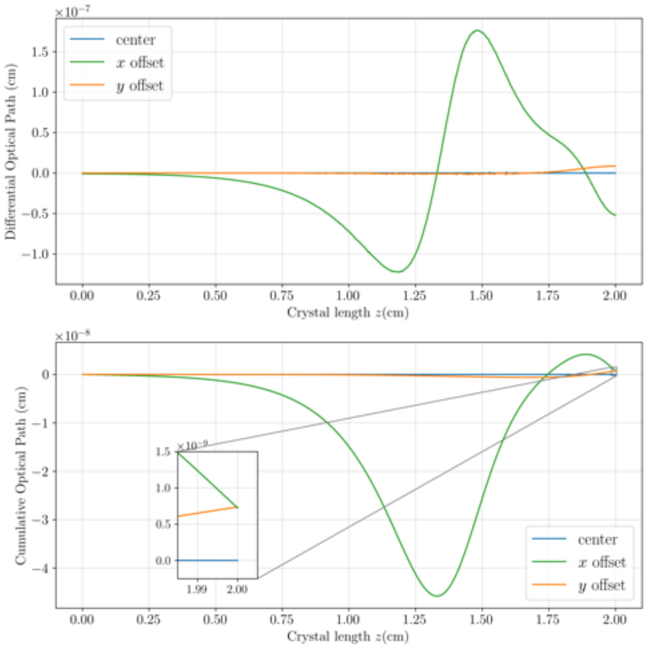

Figure 4.15: Top: differential OPL along the length of the crystal calculated between the offset axes on y and on x and the centered axis. Bottom: OPL variation along the length of the crystal. Zoomed in are the values at the end of the crystal. As expected, the cumulative values on the offset x and offset y tend to have the same value at the output, respectively $\Delta OPL_x = 7.2 \times 10^{-10}$cm and $\Delta OPL_y = 7.3 \times 10^{-10}$cm. However, it is clear that the effect in x is the result of the compensation of two much larger effects, and it is thus very sensitive to small relative variations in the two original contributions.

zero in order to inject the sidebands only on the LG_{01} mode. The top view of the EOL with the dimensions of the electrode and the crystal is shown in Figure 4.17.

Parameter	Value
L_{el}^{l}	$1[cm]$
L_{el}^{c}	$0.7[cm]$
W_{el}	$0.2[cm]$
H_{el}	$0.05[cm]$
Δy	$0.1[cm]$

Table 4.16: Optimal values for the parameters of the electrodes (el).

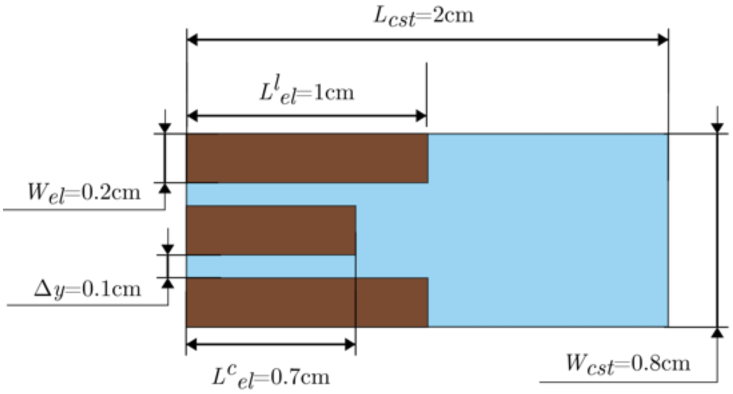

Figure 4.17: Top view of $\mathrm{EOL_{FL}}$ with the dimensions for the electrodes (brown) and the $LiNbO_3$ crystal (light blue).

Figure 4.18 illustrates the OPL along the two transversal axes calculated through the simulations where the electrodes have the optimal geometrical parameters of Table 4.16. The optical path exhibits nearly equal curvature but with opposite signs. Specifically, the obtained focal lengths are $f_x = -1.9 \times 10^3$cm and $f_y = 1.7 \times 10^3$cm. A contour plot of the phase profile across the entire output face and a zoomed-in view of the central region is depicted in Figure 4.19. In the zoomed plot is possible to see a clear saddle distribution of the phase profile.

Similarly to the study conducted with $\mathrm{EOL_{PD}}$, we computed the OPL variations along the three lines shown in Figure 4.10. As anticipated, the astigmatic case does not present the same complexities as the spherical configuration. Figure 4.20 shows that the OPL variations on both the line with the offset along x and the line with the offset along y, exhibit similar behavior. When calculating the cumulative sum of the OPL variation along the crystal, we observe contributions in the same directions on both lines without notable fluctuations, unlike what was seen in the $\mathrm{EOL_{PD}}$ case. This characteristic gives much more stability to the geometrical parameters, meaning that the effect remains approximately constant for small changes in the geometrical parameters. However, this can also be an issue. As we have seen the focal length of $\mathrm{EOL_{FL}}$ has about 10% of difference between the two axes. By changing the dimensions of

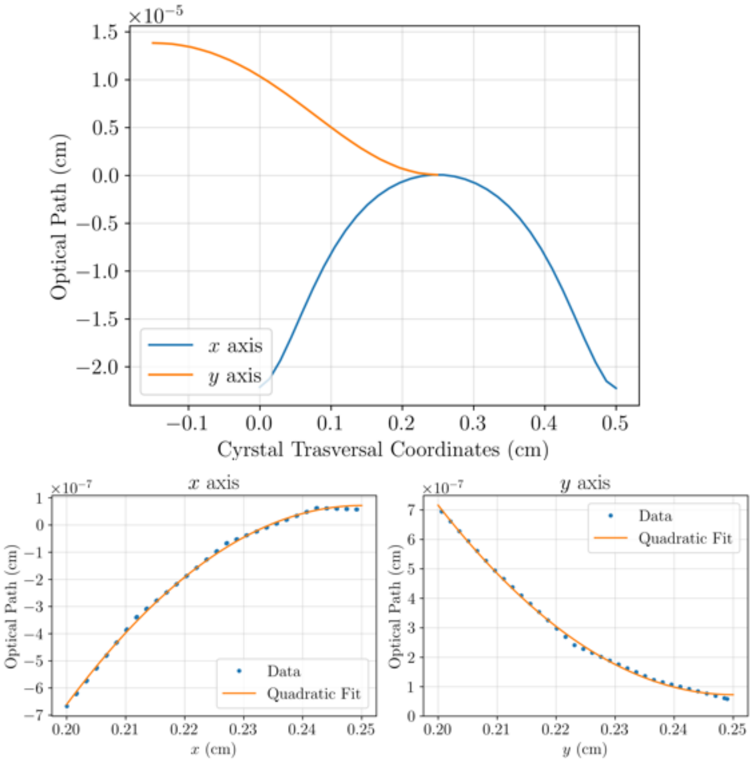

Figure 4.18: Simulation results of the OPL of $\mathrm{EOL}_{\mathrm{FL}}$ along the x and y axes. The curves are plotted to have the center of the output face at 0.25 for both axes. It is important to note that, given the simulation covers only half of the crystal, the data is presented for only half of the y axis. Top: The blue curve represents the simulated data on the x axis, while the orange curve is on the y axis. Near the center, both curves have the same curvature with opposite signs. Bottom: OPL simulated data (blue dots) in a region near the center of 0.05cm and quadratic fit (orange curves) on the two axes.

the electrodes within reasonable ranges we were not able to obtain exactly the same absolute value on both axes. However, given the low power of the lens, this difference is expected to have minimal impact on the overall outcome. Therefore we opted for this configuration as a preliminary prototype.

As stated before, all the simulations performed to optimize the design were conducted with the electrodes being symmetrically polarized with respect to the box held at ground potential. However, due to the limitation of having a single unipolar RF amplifier in the laboratory, we were forced to connect one group of electrodes to ground and another group to the amplifier providing an RF sinusoidal signal of amplitude $2V$ (this way, the voltage drop across the crystal is still $2V$, as in the case of the simulations with polarization $\pm V$). In the case of EOL_{PD}, one electrode is connected to the ground, and another is set at voltage $2V$. For EOL_{FL}, which features a total of 6 electrodes, 3 are set to the ground, and the remaining 3 are connected to $2V$, in such a way that one face has the side electrodes at ground, and the other face has the central one. This is shown in Figure 4.21. To check the impact of this change, we re-run the simulations

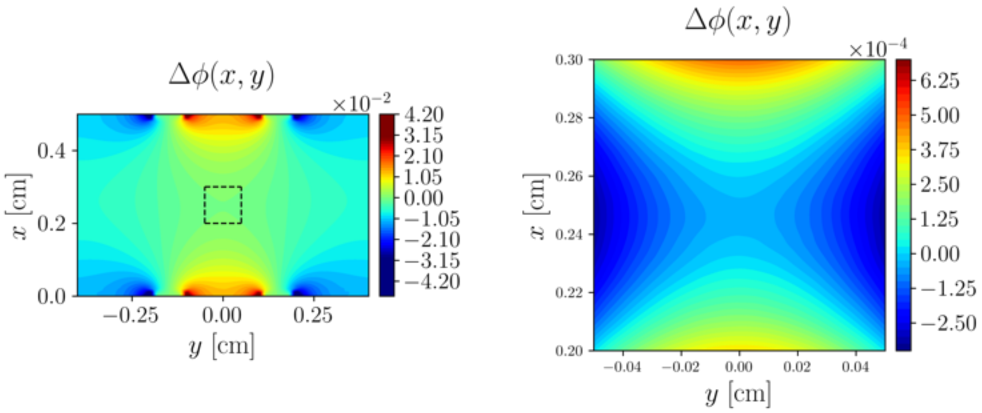

Figure 4.19: Phase profile on the output face of $\mathrm{EOL_{FL}}$. Left: The whole output face is shown. Since the beam is centered and has a small waist inside the crystal, we are interested in the center part of the crystal, enclosed in the dotted box. Right: Zoom of the centered region of the output face. We can see a clear saddle distribution of the phase profile.

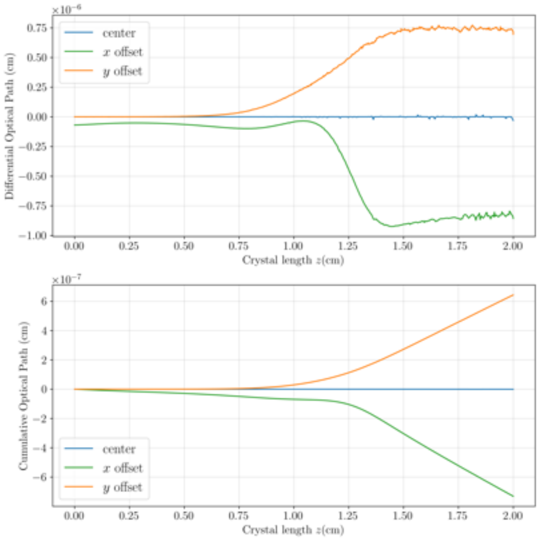

Figure 4.20: Top: OPL variation along the length of the crystal calculated between the offset axes on y and on x and the centered axis. Bottom: Cumulative OPL variation along the length of the crystal. The cumulative values on the offset y and offset x have nearly equal absolute value and opposite sign of $\Delta OPL_x = 6.4 \times 10^{-7}$cm and $\Delta OPL_y = -7.3 \times 10^{-7}$cm.

of the two final designs with the voltage configuration used in the laboratory, which we call "$(0-2V)$"; in addition, as a sanity check, we simulated the case in which the electrodes are all polarized at voltage "$(-V)$". Thanks to the superposition principle, in fact, the sum of these two cases should yield the same results as the case of symmetric electrode polarization, which we call "$(\pm V)$". Figures 4.22 and 4.24 show these results for $\mathrm{EOL_{PD}}$ and $\mathrm{EOL_{FL}}$ respectively. As it can be seen, the results are consistent (as expected), and the difference between the $(\pm V)$

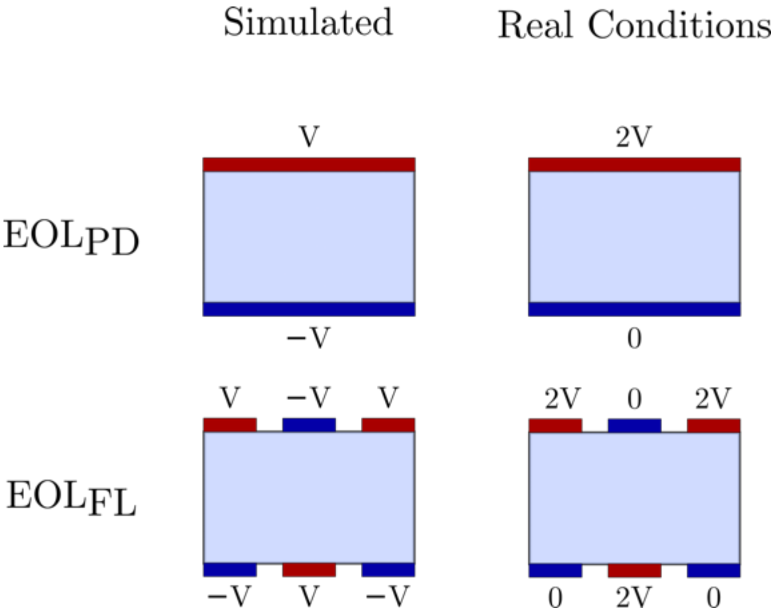

Figure 4.21: Polarization of the electrodes in the simulations versus in the real conditions. In the simulation case, we have the electrodes polarized with $\pm V$ while in the real conditions, we have $0 - 2V$.

case and the sum of the $(0 - 2V)$ and $(-V)$ cases is much smaller than the overall effect. On the other hand, it can be seen that the $(-V)$ case, which represents the difference between the ideal configuration used in the simulations to optimize the design and the one we were forced to use in the laboratory, is more impactful in the case of the $\mathrm{EOL_{PD}}$. This is due to the fact that the overall effect in the $(\pm V)$ case is about 3 orders of magnitude bigger than that of $\mathrm{EOL_{PD}}$, making the relative importance of the $(-V)$ case compared to the ideal $(\pm V)$ one, much smaller than in the case of $\mathrm{EOL_{PD}}$.

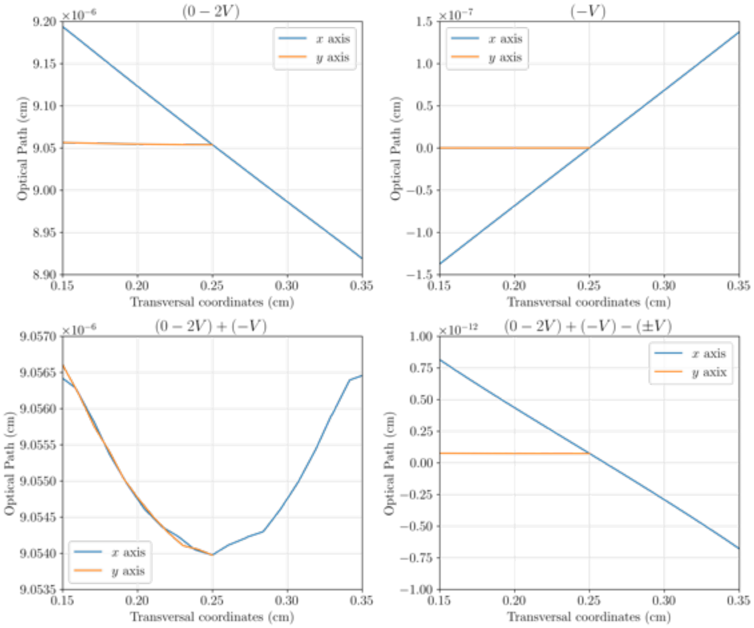

Figure 4.22: Optical path at different voltages for $\mathrm{EOL_{PD}}$. Top left: one electrode to the ground and one at 2V. Top right: both electrodes at -V. The OPL on the x axis is one order of magnitude smaller than in the previous case. Bottom left: sum of the previous configurations. Bottom right: the difference between the previous sum and the symmetric case $\pm V$ which is of the order of 10^{-12}cm.

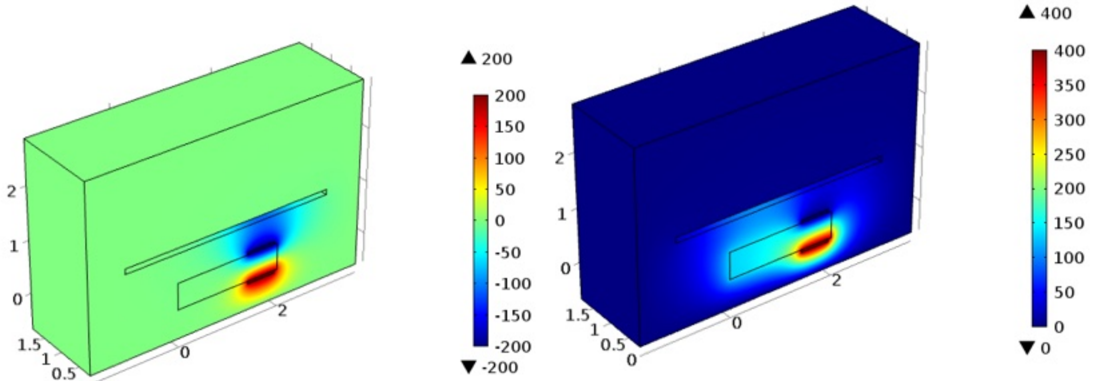

(a) Symmetric polarized electrodes at $\pm V$.

(b) One electrode connected to ground and one polarized at $2V$.

Figure 4.23: Simulated potential on the crystal for $\mathrm{EOL_{PD}}$ (only half geometry is shown) for different polarization of the electrodes.

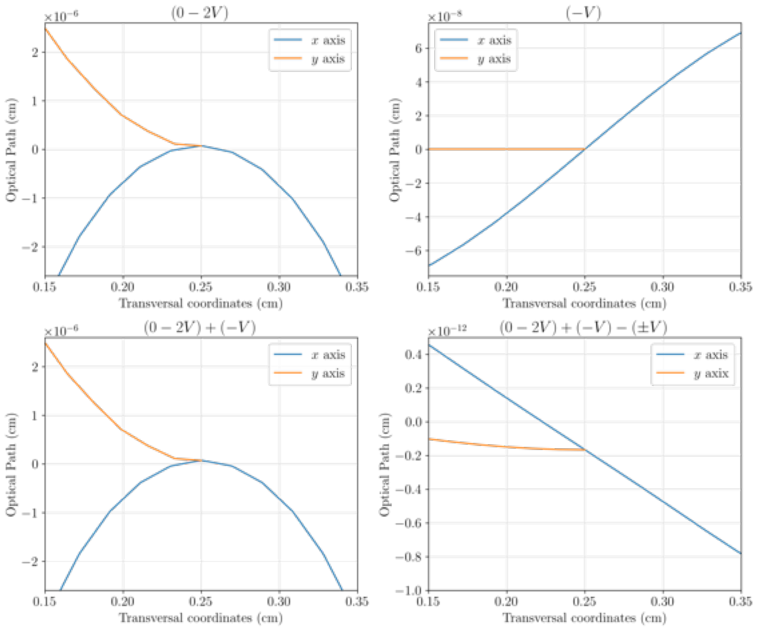

Figure 4.24: Optical path at different voltages for $\mathrm{EOL_{FL}}$. Top left: three electrodes to the ground and three at 2V. Top right: all electrodes at -V. The OPL on the x axis is two orders of magnitude smaller than in the previous case. Bottom left: sum of the previous configurations. Bottom right: the difference between the previous sum and the symmetric case $\pm V$ which is of the order of 10^{-12}V.

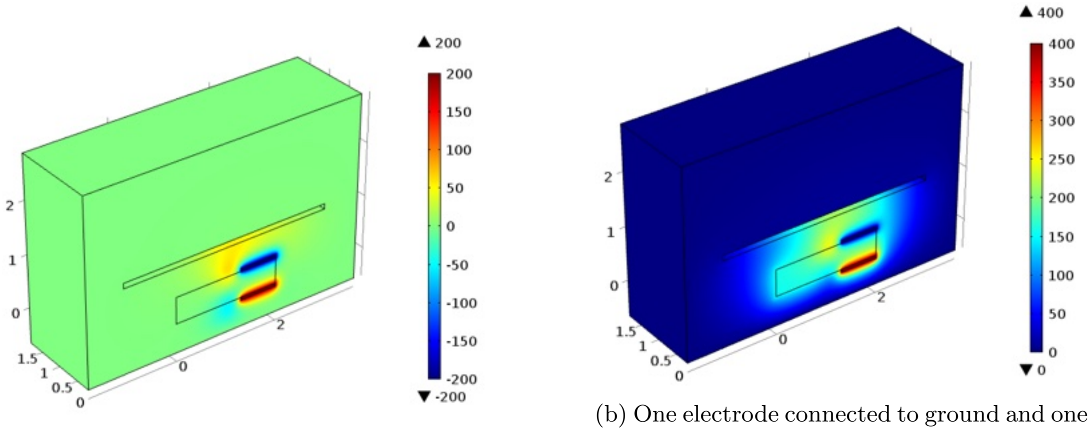

(a) Symmetric polarized electrodes at $\pm V$.

(b) One electrode connected to ground and one polarized at $2V$.

Figure 4.25: Simulated potential on the crystal for $\mathrm{EOL_{FL}}$ (only half geometry is shown) for different polarization of the electrodes.

4.2 Optical Setup

The optical setup to test the EOL is similar to the one described in [46]. In this setup we want to be able to test both designs, therefore in the area of the EOLs, we added an optical line parallel to the main one by using flip mirrors, in order to be able to operate them alternatively. Moreover, we needed to add the mode converter for the $\mathrm{EOL}_{\mathrm{FL}}$. As we take a closer look at the optical bench scheme in Figure 4.26, let's break it down by highlighting some of the essential components. These are the key optical elements that define how our experiment works.

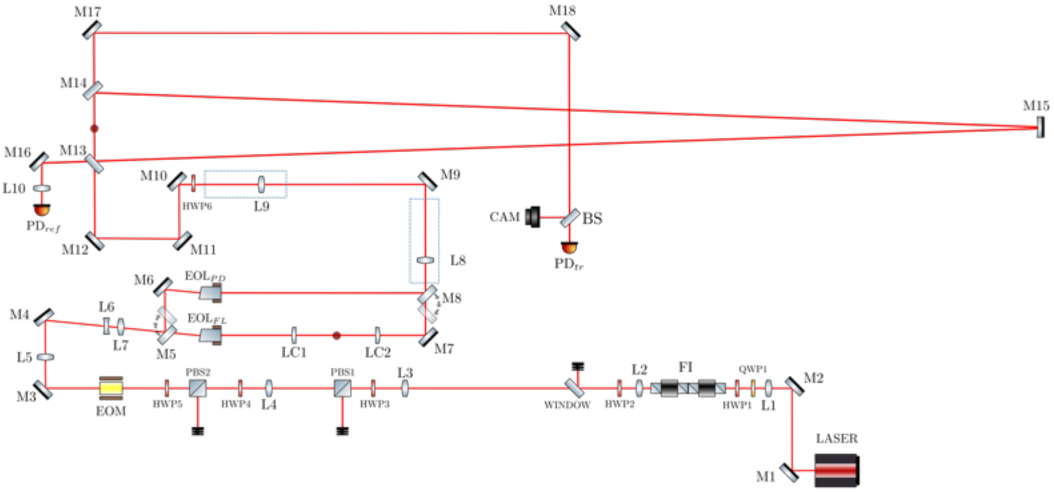

Figure 4.26: Experimental optical layout: the mode-converter telescope (MCT) for $\mathrm{EOL}_{\mathrm{FL}}$ is constituted by the cylindrical lenses LC1 and LC2, while the mode-matching telescope (MMT) consists of lenses L8 and L9. The optical cavity is made up of mirrors M13, M14, and M15. The red dots indicate the waist positions, which are required to be at the midpoint of both the MCT and the base of the cavity.

- The laser source employed is a Mephisto laser manufactured by Coherent. This laser system comprises a monolithic Nd:YAG crystal that emits light at a wavelength of 1064nm. The laser's frequency can be tuned using two actuators. One is a piezoelectric transducer (PZT), providing a swift response with a bandwidth of approximately 100kHz, but with a limited tuning range of about 200MHz. The second is a controller of the temperature of the crystal, which achieves a slower modulation with a bandwidth of 1Hz but offers a broader tuning range of about 30GHz. Both actuators are used for the feedback loop utilized in the Pound-Drever-Hall technique.
- We utilized Half-Wave-Plates (HWP) and Polarizing-Beam-Splitters (PBS) for creating pick-offs of the main optical line for other experiments. For the purpose of this experiment, HWP4 and PBS2 were used to adjust the power.

- To produce the sidebands for the PDH locking scheme, an EOM is used. It is the model 4003 produced by New Focus with a resonance frequency of 13.4MHz.

- Mirrors M5 and M8 are the flip mirrors used to switch the optical line between the two different EOLs.

- To restore the spherical behavior in the $\mathrm{EOL_{FL}}$ line, a mode-converter telescope (MCT), consisting of two cylindrical lenses LC1 and LC2, is employed, as explained in section 4.1. For our mode converter, we use cylindrical lenses of focal length $f_c = 113$mm. This means that we need to satisfy a value of waist $w_0^{MC} = 255\mu$m and of telescope length $l^{MC} = 15.98$cm. In order to control the position and dimension of the waist inside the MCT, we used a telescope before the EOL made up of two lenses, L6 and L7 in Figure 4.26, with focal lengths $f_6 = -113$mm and $f_7 = 113$mm, respectively. We decided to use these focal lengths in order to reduce the space used by this telescope. Figure 4.28 shows the beam scan after the MCT. The fit parameters are listed in Table 4.27 where we obtained that on the two axes, the q-parameters are nearly the same ($q_x \simeq q_y$), as required by a well-tuned MCT.

Parameter	$w_0\ x$	z_0
Fit Value x	$(253 \pm 2)\mu$m	$-(7.9 \pm 0.3)cm$
Fit Value x	$(251 \pm 3)\mu m$	$(-8.1 \pm 0.4)cm$

Table 4.27: Characterization of the beam after the MCT. The uncertainties of the values are the statistical errors.

- Lenses L8 and L9 are mounted on stages with a 4.5cm travel range to form a telescope called *mode-matching telescope*. As the name suggests, this telescope is used to adjust the

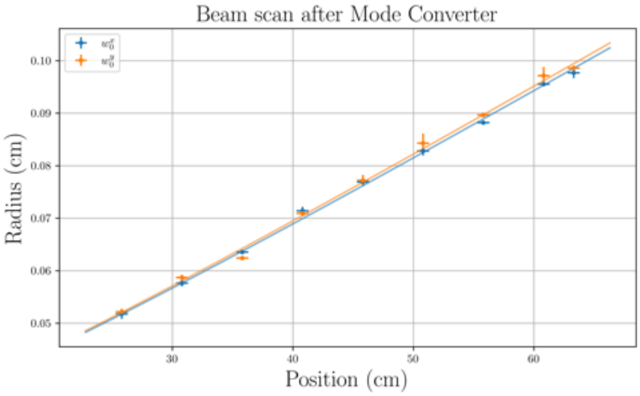

Figure 4.28: Beam scan after the MCT and Gaussian fit on both x and y axes. The zero is taken to be at the last lens of the MCT.

mismatch to the cavity. It is strategically designed to be able to study the error signals along the isolines of γ and β, showcasing the potential to decouple these two parameters. The details of the telescope's design and specifics are described in Section 4.2.1.

- A triangular optical cavity made up of the plane mirrors M13, M14 and the curved mirror M15 with a radius of curvature of 600cm. The cavity length is $L = 180$cm.
- Two photodiodes (PD), one in transmission (PD_{tr}) which serves as a control for the alignment and mismatch of the cavity, and one in reflection (PD_{ref}) which serves for both the PDH locking technique and the RFHM technique.

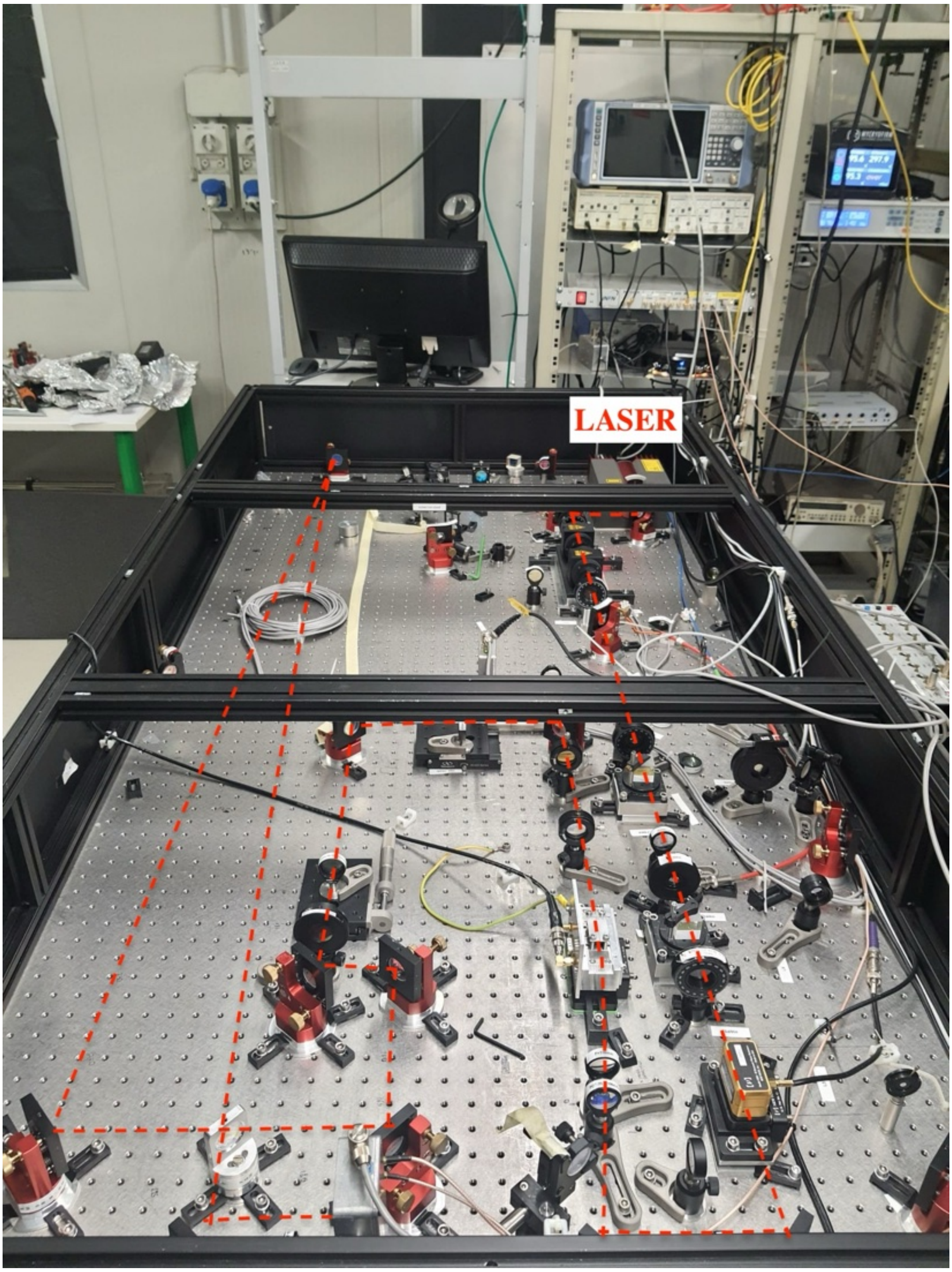

Figure 4.29: Picture of the optical bench. The dashed red line corresponds to the optical path of the laser starting from the laser source. In this picture only the $\mathrm{EOL_{FL}}$ line is present.

4.2.1 Mode-Matching Telescope

A mode-matching telescope (MMT) is generally needed to match the input beam to a cavity to the resonant mode of the cavity. In our case, it can also be intentionally detuned to test the mismatch sensing technique. To be suitable for this purpose, the telescope must be designed with some specific characteristics:

- Be able to explore both types of mismatch over a sufficient range, for both positive and negative values achieving the minimum mismatch at the midpoint of the lens travel range.
- Ensure that the β and γ mismatch parameters can be changed independently, especially near the minimum of mismatch.

Our setup is made up of two lenses, namely L8 and L9 in Figure 4.26 placed on stages with a 4.5cm travel range. The scheme of the telescope is shown in Figure 4.30. The first lens has a focal length of f_1 and is placed at distance d_1 from the reference position z_{in} of the input plane. The second lens, with focal length f_2, is placed at distance d_2 from the first lens and at distance d_3 from the reference position of the output plane. By using the ABCD matrices for the free space (M_{fs}) and the single lens (M_{sl}) listed in Table 2.5, we can obtain the matrix representation $\mathcal{M}$ of our setup as:

$$\mathcal{M} = M_{fs}(d_3) \times M_{sl}(f_2) \times M_{fs}(d_2) \times M_{sl}(f_1) \times M_{fs}(d_1) =$$
$$\begin{pmatrix} 1 - \frac{d_2}{f_1} + d_3\left(-\frac{1}{f_1} - \frac{1}{f_2} + \frac{d_2}{f_1 f_2}\right) & d_1 + d_2 - \frac{d_1 d_2}{f_1} + d3\left(1 - \frac{d_1}{f_1} - \frac{d_2}{f_2} - \frac{d_1}{f_2} + \frac{d_1 d_2}{f_1 f_2}\right) \\ -\frac{1}{f_1} - \frac{1}{f_2} + \frac{d_2}{f_1 f_2} & 1 - \frac{d_1}{f_1} - \frac{d_2}{f_2} - \frac{d_1}{f_2} + \frac{d_1 d_2}{f_1 f_2} \end{pmatrix} \tag{4.10}$$

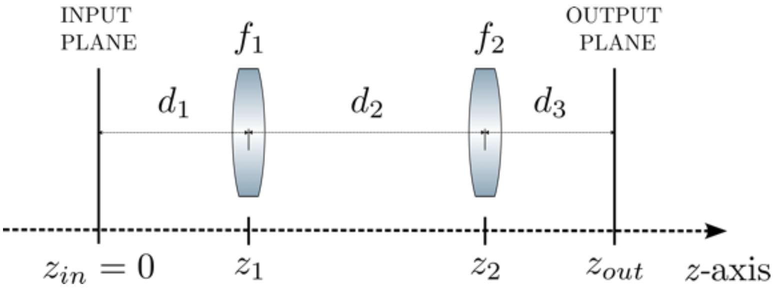

Figure 4.30: Scheme of the telescope design. The first lens has focal length f_1 and it is at distance d_1 from the input plane. The second lens, with focal length f_2, is at distance d_2 from the first lens and d_3 from the output plane.

We can then calculate the q-parameter of the output beam, q_2, as in equation (2.21). By setting the input plane on the waist position before the telescope, the q-parameter of the input is $q_1 = iz_{R1}$ and we can calculate the real and imaginary part q_2 as:

$$z_2 - z_{0_{q_2}} = \mathrm{Re}(q_2) = \frac{\mathcal{M}_{11}\mathcal{M}_{21}z_{R1}^2 + \mathcal{M}_{12}\mathcal{M}_{22}}{\mathcal{M}_{21}^2 z_{R1}^2 + \mathcal{M}_{22}^2} \tag{4.11}$$

$$z_{R2} = \mathrm{Im}(q_2) = \frac{(\mathcal{M}_{11}\mathcal{M}_{22} - \mathcal{M}_{12}\mathcal{M}_{21})z_{R1}}{\mathcal{M}_{21}^2 z_{R1}^2 + \mathcal{M}_{22}^2} \tag{4.12}$$

where $z_{0_{q_2}}$ and z_{R2} are, respectively, the position of the waist and the Rayleigh range after the telescope. We can write β and γ by using the definitions in equations (2.73) and (2.80):

$$\beta = \frac{1}{w_0^{cav}}\left(\sqrt{\frac{\mathrm{Im}(q_2)\lambda}{\pi}} - w_0^{cav}\right) \tag{4.13}$$

$$\gamma = \frac{(-\,\mathrm{Re}(q_2) + z_2) - z_0^{cav}}{2z_R^{cav}} \tag{4.14}$$

Where w_0^{cav}, z_0^{cav} and z_R^{cav} are, respectively, the waist size, position and Rayleigh range of the mode supported by the cavity. The output plane is taken to be the position of the supported waist inside the optical cavity, so $z_0^{cav} = d_1 + d_2 + d_3$. Since $\mathrm{Re}(q_2)$ and $\mathrm{Im}(q_2)$ depend on the positions of the lenses and their focal lengths, it is possible to calculate the total mismatch $MM = \gamma^2 + \beta^2$ as a function of these variables.

Our cavity has plane mirrors at the base and a curved mirror with a radius of curvature R at the opposite vertex, thus we can find the position and dimension of the supported waist as though it was a plano-concave cavity. In this case, the g-factor of the input mirror is $g_1 = 1$, while for the end mirror $g_2 = 1 - L/R$. Moreover, we can calculate the waist parameters inside the cavity from equations (2.40), (2.41) and (2.42). From the first equation we obtain that the waist needs to be at the input mirror, which in our case translates into the midpoint of the base, and with the last equation we get a waist size of $w_0^{cav} \simeq 965\mu$m. The MMT is placed right after the MCT, which means we need a telescope that magnifies the beam after the MCT, whose waist is $w_0^{mct} \simeq 252\mu$m, about 3.8 times. Moreover, we want to be able to move the lenses within the 4.5cm travel range of the stages. For these reasons, we decided to build a telescope with both lenses with positive focal length, in particular with the first lens $f_1 = 112$mm and the second $f_2 = 336$mm. We can now create the contour plots of the theoretical mismatch, β and γ as a function of the positions of the lenses, as shown in Figure 4.31. As it is possible to see, with this telescope configuration, we can effectively explore a broad range of mismatch values, on both sides of the minimum. Moreover, by looking at the plot for the γ and β isolines, we see that we can operate in a non-degenerate space. In practical terms, we can move the lenses in such a way as to produce a substantial change in one of the two parameters while leaving the other almost unchanged. The parameters of the cavity and of the mode-matching lenses used to calculate the ABCD matrix are in Table 4.32.

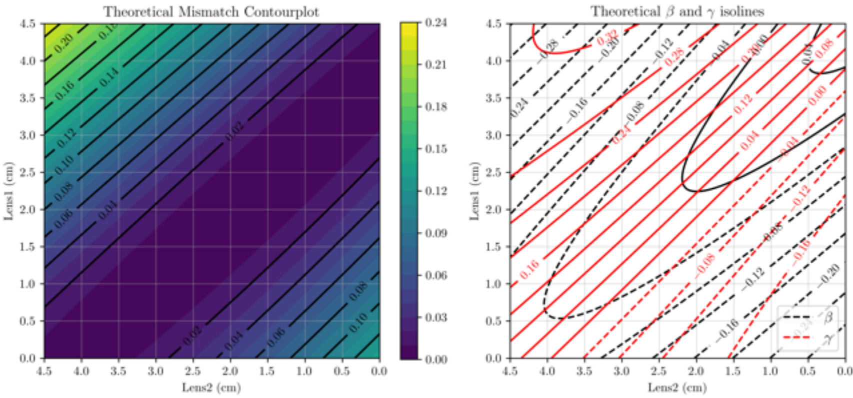

Figure 4.31: Left: Contour plot illustrating the theoretical mismatch for various positions of the telescope lenses. The lenses are positioned in translational stages which let us scan them over a range of 4.5cm. Right: Theoretical isolines for γ (red) and β (black). With this telescope design, we are able to explore a broad range of mismatch values with the minimum being at the midpoint of the lens travel range, and also we can change γ and β independently since the isolines are not parallel.

Parameter	Value
R_1	inf
R_2	600cm
L	180cm
g_1	1
g_2	0.7
w_0^{cav}	965.12μm
z_0^{cav}	131.2cm

Parameter	Value
f_1	112mm
f_2	336mm
z_1	(23.45 – 27.95)cm
z_2	(71.15 – 75.65)cm

Table 4.32: On the left, cavity parameter values. The value z_{0c} corresponds to the distance from the waist before the mode-matching telescope (input plane in Figure 4.30). On the right, mode-matching telescope parameter values. We scan the positions of the lenses z_1 and z_2 for a total increment of 4.5cm.

4.3 Electronic Scheme

In Figure 4.33, the electronic scheme for RF measurements is illustrated. We can divide this scheme into three parts: the modulation of the optics (red), the photodetectors (violet) and the I/Q demodulation (green). In order to explain the three groups let us see more in detail some of the elements shown.

- *Moku:Lab*: an adaptable hardware platform equipped with various instruments. Among these instruments is the Laser Lock Box, responsible for digitally generating the feedback signal for the PDH locking. The digital scheme for this process is illustrated in Figure 4.34. The Moku:Lab has two inputs and two outputs. The outputs serve to control both fast and slow controllers. Input 1 is designated for receiving the PDH error signal generated by the PD in reflection, which can undergo lowpass filtering and adjustable

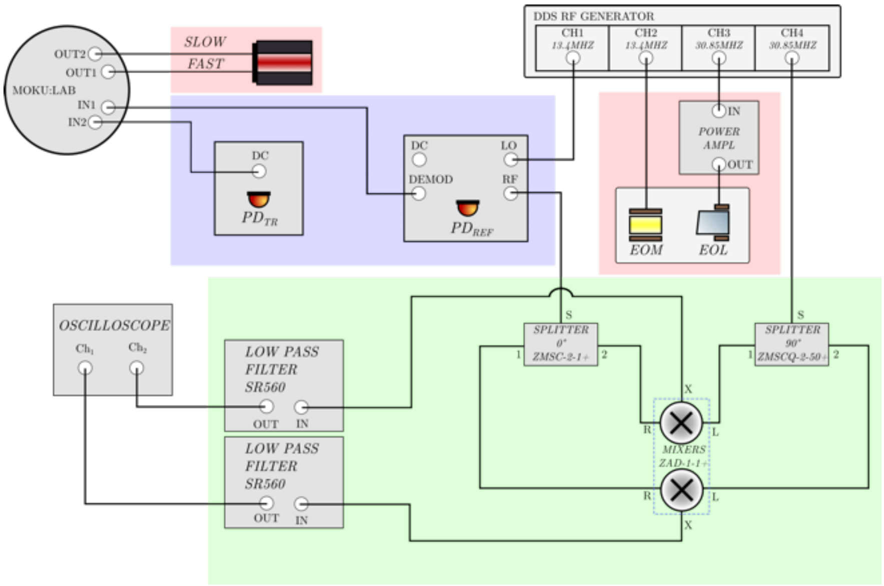

Figure 4.33: Electronic scheme, in the red boxes the modulated optics, in light blue the PDs and in green the I/Q demodulation chain.

offset. Subsequently, it is processed by two PID loops: the fast controller manages the PZT to adjust the laser's frequency, while the slow controller uses the signal generated by the fast controller to maintain the PZT offset equal to zero by changing the crystal temperature of the laser. The second input can be used as a monitor of the PD in the transmission of the cavity to identify the resonances when the cavity is being scanned by output 1.

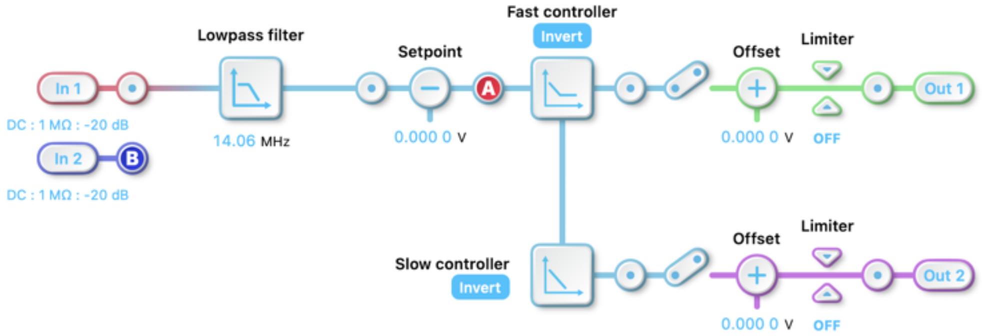

Figure 4.34: Moku:Lab digital scheme for PDH feedback loop.

- *Direct Digital Synthesizer* (DDS) RF generator: a four-channel RF generator. Two of the channels are dedicated to providing the LO (CH1) and the modulation signal (CH2) for the EOM at $13.4MHz$, while the remaining two channels are utilized for the modulation signal (CH3) and LO (CH4) for the EOL at $30.85MHz$. The signal sent to the EOL is amplified with a +50dB RF amplifier (ENI model 325LA). With the DDS we are able to change the frequency, the amplitude and the phase of each signal independently while sharing the same clock.

- *Photodetectors*: there are two single-element photodetectors in the setup. The first one operates in transmission and is employed to capture the cavity resonances during the laser's frequency scan. When the cavity is locked to the fundamental mode, the signal from this photodetector should remain at a constant maximum. The second photodetector is positioned in reflection and features one input (LO) and three outputs (DC, DEMOD, RF). This photodetector is specifically designed for demodulating the RF signal and generating the PDH error. The DEMOD output produces the PDH signal, which is then sent to input 1 of the Moku:Lab. The DC port can be used as an alternative to the DC port of the transmission photodetector. When the cavity is locked, the RF output contains the signal modulated by the EOL that is being reflected by the cavity. This means that with this technique we do not need additional PDs in order to obtain the EOL modulated signal.
- *Splitters*: to retrieve the I and Q signals, both the RF signal from the reflection PD and the LO signal from the DDS need to be split. Specifically, the RF signal is divided using a 0° power splitter (ZMSC-2-1+), ensuring that the outputs carry two signals of equal amplitude with a 0° phase relationship. In contrast, the LO signal undergoes a split with a 90° phase difference between the two outputs (ZMSCQ-2-50+). This phase difference is essential for achieving the I/Q demodulation.

The process for obtaining the mismatch signals is as follows. The reflected RF signal from the PD carries information about mismatch parameters. This signal is split, and its outputs are combined with the LO signal at the same frequency of the modulation of the EOL. One output is mixed with the in-phase LO, while the other is mixed with the quadrature LO. It's important to note that the terms "in-phase" and "quadrature" don't necessarily align with the RF signal components due to an unknown phase relationship, resulting in a mere rotation of the final signals. The mixer outputs are then directed to individual low-pass filters (SR560), with one filter for each mixer output. The filtered signals, referred to as Ch_1 and Ch_2, are subsequently read by an oscilloscope. As we will show in chapter 5.4 these channels are a linear combination of the γ and β signal we want to retrieve.

Chapter 5

Measurements

In this chapter, we will present the measurements conducted which show the first promising results to demonstrate the functionality of the RFHM technique. Starting from the characterization of the cavity and its locking, we will continue with the characterization of the mode-matching telescope. Then we will proceed by showing the first measurements proving that the EOL behaves as a lens modulating the LG_{01} peak through a slow lock-in method; finally, we will present the RF measurements demonstrating both the sensitivity to the absolute mismatch value as well as the ability to decouple the contributions due to waist size and position discrepancy.

5.1 Optical Cavity: experimental characterization

A fundamental aspect of our experiment revolves around the utilization of an optical cavity. For simplicity in extracting the reflected field, our optical cavity has a triangular configuration, featuring plane mirrors along the base and a curved mirror at the vertex, with a radius of curvature $R = 600$cm. From the length of the cavity, $2L = 355$cm, obtained by calculating the base, $b = 15$cm, and the height, $h = 170$cm, we can estimate the cavity parameters. However, a more precise determination is achieved through an analysis involving the cavity scan. This is made by sending a voltage ramp at a frequency of a few Hz (in our case 5 Hz) to the PZT of the laser to change its frequency and scan the resonances. By acquiring the signal in transmission, we can measure the FSR, the linewidth and the HOM spacing of the cavity. The FSR can be obtained directly from the frequency separation between consecutive peaks of the same order, typically two consecutive fundamental modes, and the linewidth is computed as the Full Width at Half Maximum (FWHM) of the fundamental mode resonance peak. Finally, the HOM spacing is measured as the separation between the fundamental mode and the 1st-order mode, which we can excite and recognize by slightly misaligning the cavity. To verify the correspondence between the mode and the resonance, an infrared camera is used. Since what we measure is the signal in transmission as a function of time, we need to calibrate the laser frequency scan rate in order to evaluate the transmission signal versus the laser frequency. This calibration is achieved by using the modulation for the PDH signal done via an EOM at a frequency of $f_{eom} = 13.4$MHz. The result is the generation of sidebands on the laser beam at frequency $\pm f_{eom}$, which are observable in the transmitted signal. By calculating the temporal separation between the two fundamental peaks and comparing it with the temporal gap between the fundamental peak and the ±13.4MHz sidebands, we can determine the FSR, the linewidth and the HOM spacing. To increase accuracy, we acquire multiple scans of the resonances. This allows us to compute averages and calculate the error associated with the standard error of the mean. Moreover, from the FSR and linewidth values, we can derive the length (eq. (2.55)) and the finesse of the cavity ($FSR/FWHM$), while with the HOM we can compute the g parameter (eq. (2.56)). Table 5.1 reports the calculated parameters of the cavity.

Parameter	Value
FSR$^{\mathrm{a}}$	84.3 ± 0.7MHz
L^{b}	177.9 ± 0.7cm
FWHM$^{\mathrm{a}}$	506 ± 5kHz
$\mathcal{F}^{\mathrm{c}}$	166 ± 3
HOM$^{\mathrm{a}}$	$15.41MHz$
g^{d}	0.71 ± 0.01

Table 5.1: Parameters of the cavity calculated from the signal in transmission. The values are calculated with: $^{\mathrm{a}}$ the cavity scan, $^{\mathrm{b}}$ the FSR, $^{\mathrm{c}}$ the FSR and the FWHM, $^{\mathrm{d}}$ the HOM spacing.

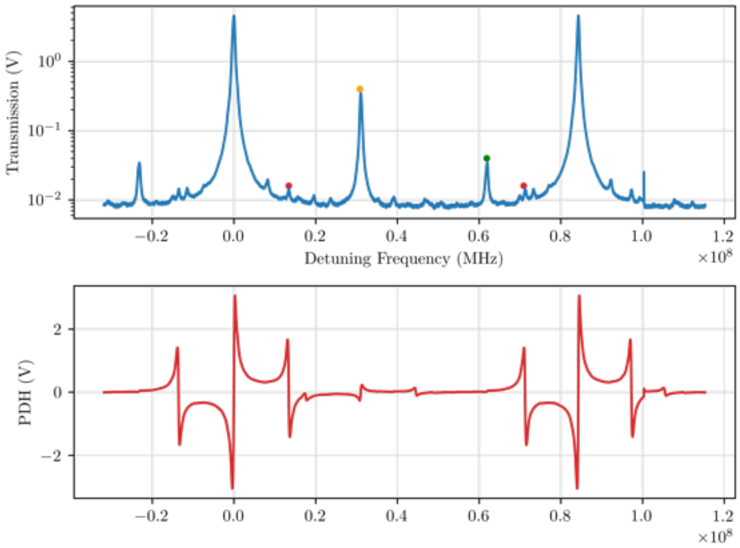

Figure 5.2: Transmitted signal (top) and PDH signal of the optical cavity (bottom) as a function of the detuning frequency from an arbitrary fundamental resonance peak. The ordinates of the transmitted signal are in logarithmic scale for easier visualization of the resonances present between two fundamental modes. It is possible to observe three main peaks: the yellow dot marks the LG_{01} peak, the green dot the LG_{02} and the red dots the 13.4MHz sidebands.

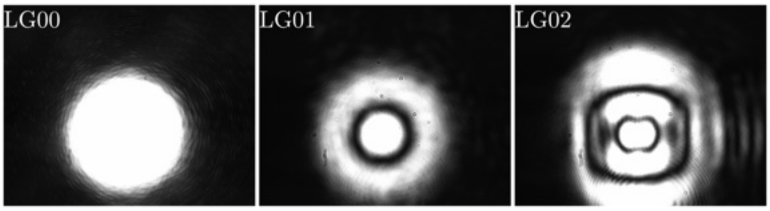

Figure 5.3: Intensity patterns of the LG_{00}, LG_{01} and LG_{02} modes.

In Figure 5.2, the PDH, generated by the PD in reflection, and the transmitted signals are displayed during a cavity scan in a range greater than an FSR. The transmitted signal, showing various resonating modes, is depicted on the ordinate axis using a logarithmic scale for enhanced visualization. Between the fundamental resonances at 0MHz and 84.3MHz (where the frequency is expressed as a detuning from the first fundamental mode in the scan), there are two main peaks which are the LG_{01} and the LG_{02} peaks. Identifying these modes is straightforward by examining their respective frequencies, which fall at 2HOM= 30.32MHz and 4HOM=60.64MHz. Additionally, their presence can be observed visually through a camera, as shown in Figure 5.3. Furthermore, there is a third peak at 13.4MHz, representing the sideband generated through the EOM modulation for the PDH signal. Its resonant frequency aligns precisely with the PDH signal illustrated in the PDH plot of Figure 5.2, where these three higher-order modes are marked for easier recognition.

Since the FSR of our cavity is 83.74MHz and the laser piezo has a tuning coefficient of 3MHz/V, we need to send to the piezo a ramp with an amplitude of about $30V$ to be able to see a full FSR, for which we used an amplifier (E-413.6, PI); however, when locking the cavity we noticed that this amplifier introduces on the error signal a wide resonance at 20kHz and others narrower starting from $50kHz$, making the locking highly unstable. For this reason, we opted to not use the amplifier and send to the piezo a $2V$ ramp while using the temperature control to center the fundamental resonance. Figure 5.4 shows the amplitude spectral density of both the error signal with and without the amplifier. We obtained the best error signal by changing the PID parameters to minimize the resonances seen in the spectral density following a similar process as in [47]. Even though with the amplifier at low frequency we can reach lower values of the spectral density, at high frequency it is clear that it introduces more noise which we could not eliminate by adjusting the PID parameters. In Figure 5.5 the error signal versus time is presented for both cases, along with a histogram of the recorded values. From these plots, we can see two main differences: in the case without the amplifier, the noise follows a Gaussian distribution with zero mean and standard deviation 0.1kHz, while with the amplifier the noise oscillates and thus has a multimodal distribution with the lateral values more likely than the center one. Moreover, in the latter case, we have a distribution width about one order of magnitude larger the the Gaussian case.

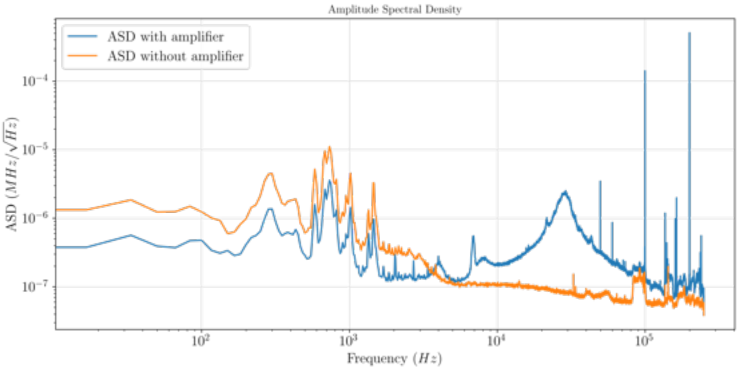

Figure 5.4: Amplitude spectral density of the cavity with (blue) and without (orange) the amplifier. In the former scenario, the error signal exhibits a broad resonance at 20kHz, along with several narrower resonances emerging from 50kHz, which are not present without the amplifier. Additionally, a cluster of resonances around 700Hz is observed, attributed to the mechanical resonances of the holders. The same cluster was observed in another experiment within the same laboratory that used the same type of holders, as reported in [55].

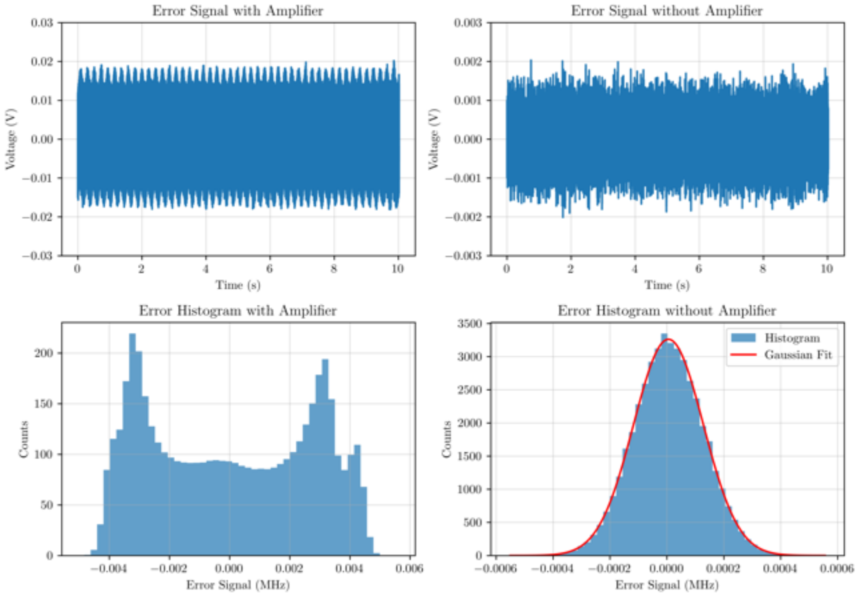

Figure 5.5: Error signal from the cavity with (left) and without (right) the amplifier. The signal with the amplifier oscillates following a multimodal distribution, while without the amplifier we obtain a Gaussian noise with zero mean and standard deviation about one order of magnitude smaller.

5.2 Mode-Matching Telescope Calibration

In Section 4.2.1, we discussed the design process of the mode-matching telescope. However, precisely measuring the exact relative locations of the lenses, the cavity and the input beam waist is not trivial; therefore, to test the RF mismatch sensing technique, it is crucial to calibrate the telescope model to measured data, to have a reliable quantitative prediction of the expected values of β and γ as a function of the position of the lenses. To achieve this calibration, we compared the theoretical predictions of mismatch presented in Figure 4.31 with the measured ones at different positions of the lenses as shown in Figure 5.6. More precisely, we performed a fit of the model to the measured values of the mismatch. Experimental values for the mismatch were obtained by scanning the cavity and calculating the ratio between the amplitudes of the first-order Laguerre-Gaussian peak P_{01} and the fundamental peak P_{00}:

$$MM^{exp} = \frac{P_{01}}{P_{00}} \tag{5.1}$$

The experimental mismatch measurements align qualitatively well with the theoretical expectations.

It is important to note that our model relies on the first-order Taylor expansion in the mismatch parameters. As the magnitude of mismatch increases, considering only the first-order expansion becomes inadequate, with higher-order terms assuming greater significance. Consequently, when faced with high mismatch values, deviations between the model's predictions and the measured values are expected. Importantly, this constraint does not hinder the technique's primary objective, which is to extract information from scenarios characterized by low mismatch values. Even more so, the technique is meant to be used in a feedback control scenario, where the most important thing is that the error signal is bipolar and goes to zero when the mismatch does. To account for potential discrepancies, an error was applied to the fit data, corresponding to 10% of the experimental mismatch value for $MM^{exp} < 0.15$ and 15% for $MM^{exp} > 0.15$.

The fitting procedure involved holding constant the model parameters we felt more confident about while leaving as free parameters the ones that were more difficult to precisely determine independently, in order to avoid overfitting. The model parameters are the focal lengths of the lenses and their positions, the waist size and position of the input beam (which is the beam after the MCT) and the waist size and position of the output beam, i.e. the cavity supported beam. We decided to fix the focal lengths and the relative distance between the two lenses. Since we characterized the waist size inside the cavity as shown in the previous section, the procedure should also involve fixing this parameter and taking its position as the origin. We also know the parameters of the input beam from the beam scan shown in Figure 4.28, but since we were able to perform the beam scan only in the far field, we probably have bigger uncertainties and therefore less precise values for the waist size and position. Therefore, from

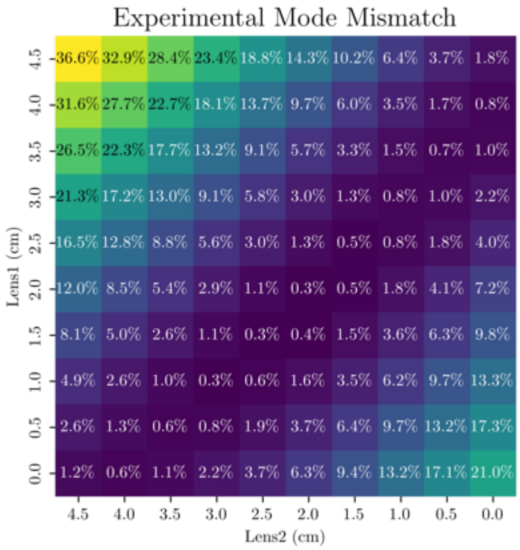

Lens1 (cm) \ Lens2 (cm)	4.5	4.0	3.5	3.0	2.5	2.0	1.5	1.0	0.5	0.0
4.5	36.6%	32.9%	28.4%	23.4%	18.8%	14.3%	10.2%	6.4%	3.7%	1.8%
4.0	31.6%	27.7%	22.7%	18.1%	13.7%	9.7%	6.0%	3.5%	1.7%	0.8%
3.5	26.5%	22.3%	17.7%	13.2%	9.1%	5.7%	3.3%	1.5%	0.7%	1.0%
3.0	21.3%	17.2%	13.0%	9.1%	5.8%	3.0%	1.3%	0.8%	1.0%	2.2%
2.5	16.5%	12.8%	8.8%	5.6%	3.0%	1.3%	0.5%	0.8%	1.8%	4.0%
2.0	12.0%	8.5%	5.4%	2.9%	1.1%	0.3%	0.5%	1.8%	4.1%	7.2%
1.5	8.1%	5.0%	2.6%	1.1%	0.3%	0.4%	1.5%	3.6%	6.3%	9.8%
1.0	4.9%	2.6%	1.0%	0.3%	0.6%	1.6%	3.5%	6.2%	9.7%	13.3%
0.5	2.6%	1.3%	0.6%	0.8%	1.9%	3.7%	6.4%	9.7%	13.2%	17.3%
0.0	1.2%	0.6%	1.1%	2.2%	3.7%	6.3%	9.4%	13.2%	17.1%	21.0%

Figure 5.6: Heatmap of experimental mismatch values obtained by moving the mode-matching lenses positions.

the fit, we wanted to obtain the parameters of the input beam and a global offset for the position of the lenses. We were unable to obtain values for the input beam that were consistent with the model and the expected values therefore, due to time constraints, we decided to attempt a more phenomenological method by fixing the input beam and fitting the values of the output beam, obtaining results that align with the model. Even though we are aware of potential discrepancies in subsequent measurements due to the physical weakness and lower accuracy of this model compared to the other, we decided to use it while remaining conscious of the associated challenges. In this case, the origin was set to the position of the input beam and the fixed and fitted parameters were:

Fixed Parameters:

- Focal lengths of the telescope's lenses $f_1 = 112$cm and $f_2 = 336$cm.
- The separation $dl = 47.7$cm between the telescope's lenses when positioned at corresponding points within their scanning range.
- Waist size of the input beam $w_0^{in} = 252\mu$m.

Fitted Parameters:

- A global offset on the lenses position δz_t with respect to the origin
- The cavity waist position z_0^{cav} with respect to the origin
- The cavity waist size w_0^{cav}

It is important to note that the cavity waist position z_0^{cav} does not represent the location of the waist inside the cavity; instead, it denotes the position of the entire cavity relative to the origin.

In Table 5.7 it is possible to see the theoretical and fitted values for these three parameters. The errors for the fitted values are calculated as the standard deviation from the covariance matrix of the fit. Figure 5.8 illustrates the fit residuals contour plot, calculated as the difference between the fitted data and the experimental ones, showcasing the effectiveness of the fit in the region of minimum mismatch. However, as anticipated, the fit diverges more from the theoretical values at higher mismatch values.

Parameter	Theoretical Value	Fitted Value
δz_t	0cm	(5.55 ± 0.16)cm
δz_0^{cav}	135.5cm	(130.2 ± 0.8)cm
w_0^{cav}	$970 \pm 12\mu$m	$(1052 \pm 14)\mu$m

Table 5.7: Fit values for the global offsets and the waist.

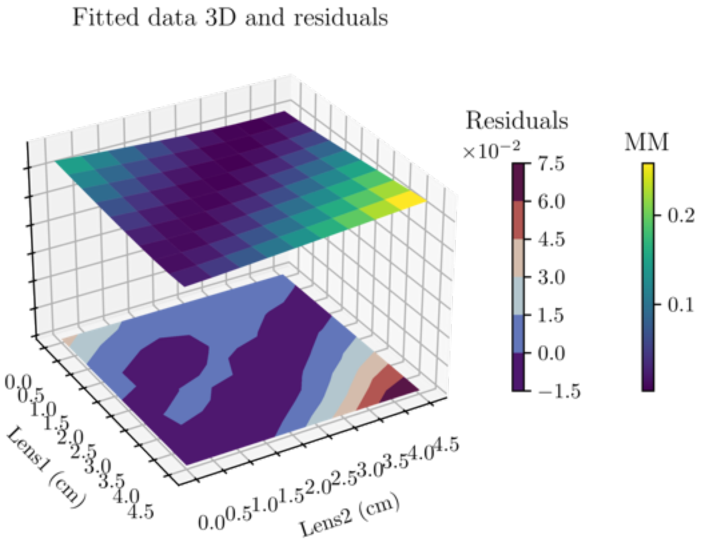

Figure 5.8: Plot of the fitted mode mismatch together with the residuals. As anticipated, deviations from theoretical values become more pronounced at higher mismatch positions.

To enhance the comparison between the fitted and experimental mismatches visually, Figure 5.9 includes both the fitted contour plot with its isolines and the isolines for the experimental mismatch. Notably, a close alignment between the isolines of the fit and the experimental data is observed, particularly in the central region where the minimum mismatch occurs. In Figure

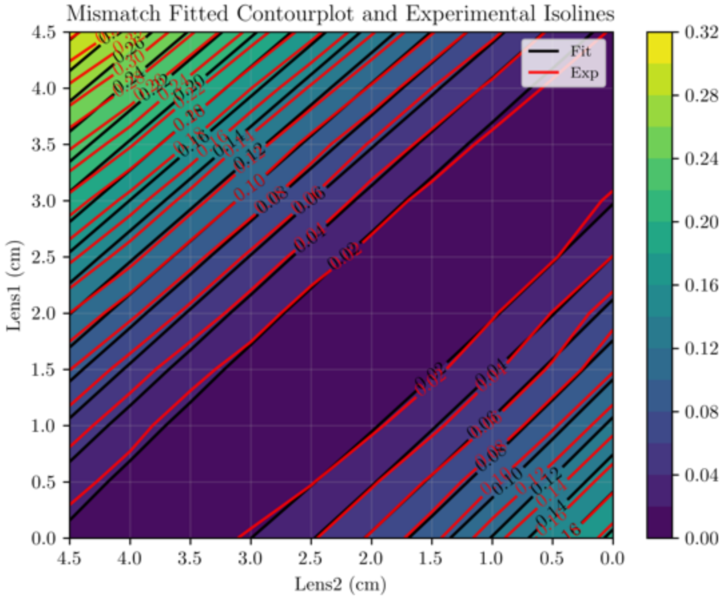

Figure 5.9: Mismatch contour map obtained through the fit with the experimental isolines (in red) overlapping.

5.10 we present the difference in mismatch at different values of the lenses with and without the EOL. This plot was obtained by calculating the effect in the mismatch when we add a lens with a focal length of $f = 1.8 \times 10^3 cm$ (as the simulated $\mathrm{EOL_{FL}}$ focal length) in correspondence of the position of the EOL on our optical bench. As we can see, we have a change in the mismatch that depends on the mode matching telescope positions with a general order of magnitude of 10^{-3}. It is important to note that with this technique we do not aim at correcting the mismatch actively, but rather at sensing the mismatch to retrieve an error signal which can be used as a feedback signal for dedicated actuators. In the next section, we will describe a slow lock-in measurement to observe the difference in the LG_{01} peak with and without the lens and we will present how this difference has the same order of magnitude as the calculated one using the simulated value of the lens focal length.

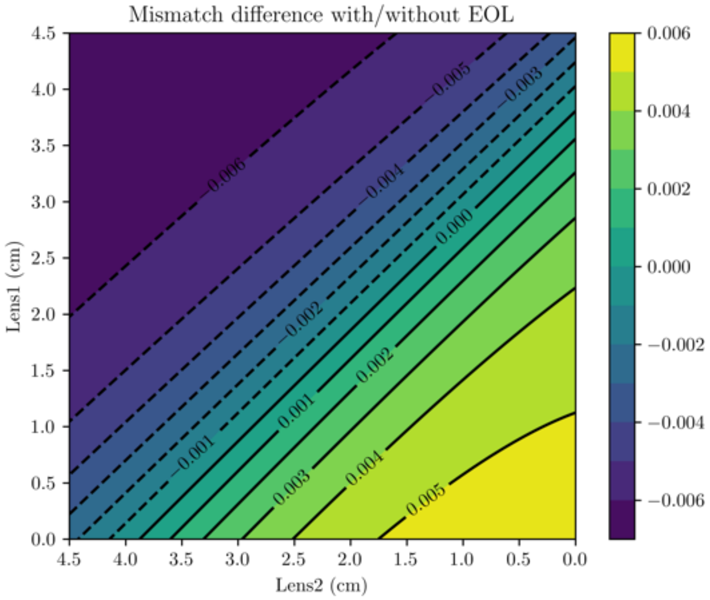

Figure 5.10: Contourplot of the difference in mismatch with and without the EOL.

5.3 Slow Lock-In Measurements

As we have seen in section 4.1.2 both EOLs act as a lens. While the theoretical design and specifications provide a foundation for its expected behavior, practical verification is essential to ensure that the EOLs operate as intended in a real-world optical system. The first test we can conduct is a slow lock-in measurement [46]. By sending to the EOL electrodes a high-voltage, slow-frequency square wave we can mimic an ON/OFF behavior of the lens. We expect a difference in the amplitudes of the LG_{01} peaks between the ON and OFF cases. However, our experiment is in air and exposed to several environmental disturbances, thus the height of the peaks tends to be noisy; to determine whether this difference is due to random fluctuations or if it reflects a consistent pattern, we acquired multiple scans and calculated the average. We scanned the cavity by sending a ramp to the piezo of the laser and we collected the cavity transmission signal over 30 seconds. In addition to prove the effectiveness of the EOL, this measurement is also used to align the EOL with respect to the laser beam by adjusting the screws on its support and maximizing the effect on the LG_{01} modulation. We conducted this test for both EOLs.

To carry out this process, we utilize the Moku:Lab. This allows us to generate the modulation square waves with a frequency of 0.5 Hz, as well as the ramp wave with a frequency of 5 Hz for scanning the cavity. It is important to note that the ramp has a higher frequency than the square wave, in this way for each ON and OFF we can measure multiple peaks. The DataLogger application in Moku:Lab is used for both generating and acquiring the square and ramp signals, along with the input signal, representing the transmission from the cavity. Us-

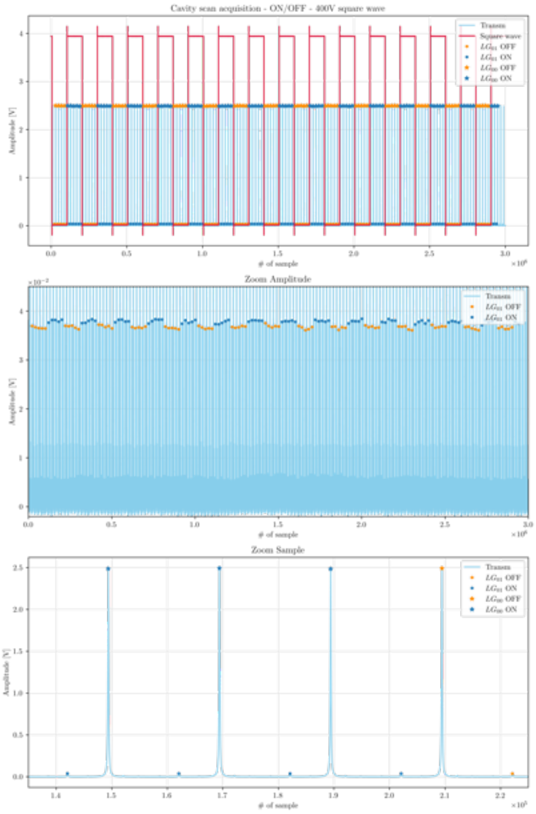

Figure 5.11: Cavity scan acquisition over 30 seconds while modulating the EOL ON/OFF at 0.5 Hz. In the top plot, the red curve represents the square wave sent to the electrodes after being amplified with a gain of 100, resulting in a range of $0-400V$. The light blue curve represents the signal from cavity transmission, where LG_{00} peaks are marked with star symbols and LG_{10} peaks with dots. Markers associated with the high values of the square wave are colored in blue, while those linked to low values are represented in orange. The center plot provides a zoomed view along the y axis, enhancing the visualization of modulation on LG_{01} peaks. The bottom plot zooms in on the x axis, showing the detected peaks over a few FSRs.

ing the same device for both signal generation and acquisition allows easy synchronization, enabling us to discern the peaks acquired with the EOL ON and OFF. The code designed for analyzing ON/OFF behavior involves peak recognition of the LG_{00} and LG_{01} modes by peak power falling in a given range and grouping in ON and OFF sets as shown in Figure 5.11. For every peak, 800 samples preceding and following the peak's maximum are collected to entirely reconstruct the resonance. By aligning every peak acquired during the ON state and those acquired during the OFF state, we produce an average profile for each of the two groups, along with the corresponding standard deviation. The same analysis is repeated for LG_{01} and LG_{00}, followed by the calculation of the mode mismatch through equation (5.1). The results of this test on both EOLs are presented below.

Modulation of the EOL_{PD}

Figure 5.12 shows the data taken with the EOL_{PD} polarized with a square wave of 0-400V. The effectiveness of the modulation is demonstrated in two ways: by comparing the two populations of individual maxima collected for the ON and OFF positions, which show separated distributions and by comparing the mean reconstructed peaks for the ON and OFF positions, which differ in their maximum value by several standard deviations. Figure 5.12 also shows two control tests: an analysis of the LG_{01} peak applied by grouping peaks randomly rather than based on the ON-OFF state of the EOL, and the proper ON-OFF analysis applied to the LG_{00} peak. None of the two tests shows meaningful differences, confirming that the observed effect is a genuine LG_{01} modulation due to the polarization of the EOL. However, we note that the average peak shape does not resemble perfectly a Lorentzian function and presents a distortion. The other resonances did not present this characteristic, and it cannot be attributed to the effect of the EOL since it is visible both with the lens turned on and off. One possible expla-

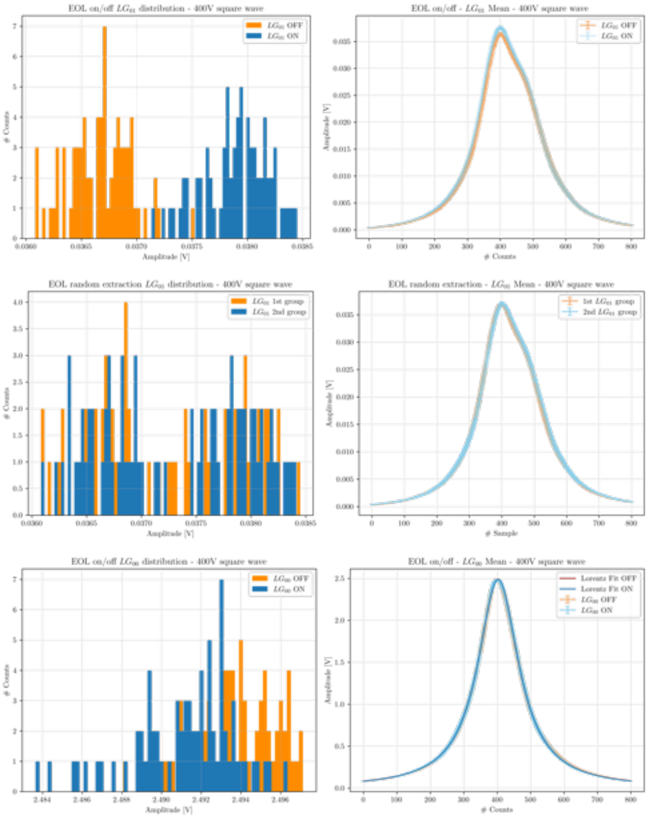

Figure 5.12: Data with square wave $0 - 400\text{V}$ for EOL_{PD}. Top: the dataset is segmented into two groups: ON (blue) and OFF (orange). Reported are the histograms of the amplitudes of each LG_{01} peak found in the 30s data acquisition (left) along with the averaged peaks of the mode in the two scenarios (right). Center: the control test where instead of dividing the data in ON and OFF, we divided them into two groups with randomly selected peaks. Bottom: the same ON-OFF analysis but for the LG_{00} peak in which we do not see modulation nor the distortion present in the LG_{01} peaks.

nation could be astigmatism introduced by the triangular cavity, causing the two higher-order modes HG02 and HG20 to resonate at slightly different frequencies.

The mismatch values, calculated with equation (5.1), in the ON-OFF cases are listed in Table 5.13. We measured a mismatch difference between the two cases of 0.04%, while according to the simulations we were expecting a mismatch difference two orders of magnitude smaller. As we have seen, however, $\mathrm{EOL}_{\mathrm{PD}}$ is very sensitive to geometrical parameters, and without a direct measurement of the wavefront we cannot be sure that it acts correctly as a spherical lens with a focal length equal to the one obtained through simulations; indeed, we note that by only measuring the modulation in the power of the peak at twice the HOM spacing, we are actually measuring an effect on the second-order modes (i.e. HG_{02}, HG_{20} or their rotated versions), and not necessarily LG_{10}. From the simulations, we know that any construction imperfection will make the $\mathrm{EOL}_{\mathrm{PD}}$ produce an effect that is non-spherical, and in general larger than the spherical one. A deeper study of the effect of $\mathrm{EOL}_{\mathrm{PD}}$, using for example a Shack-Hartmann sensor able to directly measure the full wavefront distortion with enough sensitivity, would be needed to fully investigate this discrepancy.

MM_{OFF}	$(1.47 \pm 0.05)\%$
MM_{ON}	$(1.51 \pm 0.05)\%$
$MM_{OFF} - MM_{ON}$	$(0.04)\%$

Table 5.13: Data of the mismatch values in the ON and OFF scenarios by modulating $\mathrm{EOL}_{\mathrm{PD}}$

Modulation of the $\mathrm{EOL}_{\mathrm{FL}}$

Similarly to the analysis conducted above, in Figure 5.14 it is possible to see the modulation of the LG_{01} and the LG_{00} peaks due to the $\mathrm{EOL}_{\mathrm{FL}}$, by sending to its electrodes a square wave of 0-400V. In this case, we can observe that the averaged LG_{01} peak has a Lorentzian shape without the same distortion seen in the case of the $\mathrm{EOL}_{\mathrm{PD}}$. The reason could be attributed to the fact that between the two measurements, we modified the cavity making it slightly longer and repeating the alignment. This may have reduced astigmatism making the second-order modes so close that their individual resonances are not distinguishable. We omit to show the control test on the randomized group since the modulating effect on the LG_{01} resonance is even more evident than it is with the $\mathrm{EOL}_{\mathrm{PD}}$. With this EOL we confirmed that the modulation is proportional to the amplitude of the square wave by modulating the EOL also with an amplitude of 0-200V. The mismatch values for the 0-400V and 0-200V measurements are presented in Table 5.15. In the former, the discrepancy between the mismatch in the ON and OFF states is quantified as $MM_{OFF} - MM_{ON} = 0.12\%$, whereas in the latter, with a voltage range of 0-200V, the difference is approximately halved, resulting in $MM_{OFF} - MM_{ON} = 0.05\%$. In the previous section, we have calculated the expected difference of mismatch between the ON

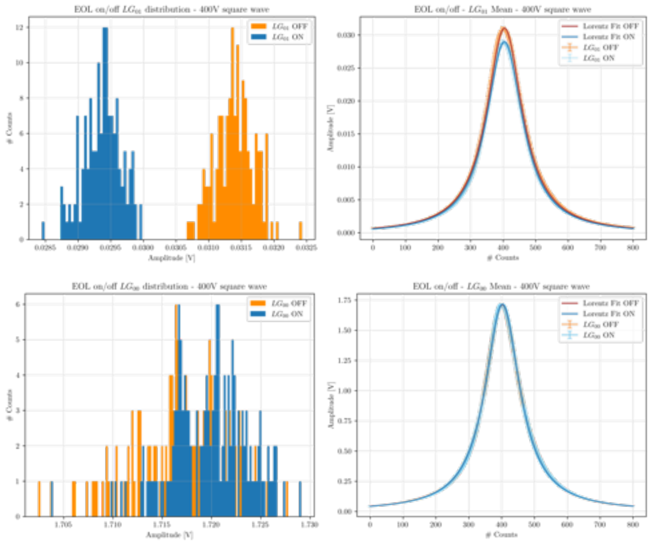

Figure 5.14: Data with square wave $0-400$V and 30s of acquisition. The dataset is segmented into two groups: ON (blue) and OFF (orange). We report the histograms of the amplitudes of each LG_{01} and LG_{00} (left) and their averaged peaks (right).

and OFF cases, shown in Figure 5.10, and we have seen that it depends on the position of the telescope. In this case, where the mismatch in the OFF case is 1.8%, the difference has the same order of magnitude as the expected one.

	$0-400V$	$0-200V$
MM_{OFF}	$(1.82 \pm 0.02)\%$	$(1.82 \pm 0.02)\%$
MM_{ON}	$(1.70 \pm 0.02)\%$	(1.77 ± 0.02)
$MM_{OFF} - MM_{ON}$	0.12%	0.05%

Table 5.15: Data of the mismatch values in the ON and OFF scenarios by modulating EOL_{FL} with two different voltages.

5.4 RF Measurements

In this section, we will present the results that attest to the effectiveness of the RF mode-mismatch sensing technique. We conducted the tests for both EOLs, however we obtained positive outcomes only for EOL_{FL}. For this reason in this section, we will report only the data obtained with this prototype. It is important also to note that, despite the successful demonstration, ongoing efforts are required to enhance the precision and sensitivity of the technique for its application in the field of gravitational waves. The need for further refinement is motivated by the goal to achieve accurate sensing of mismatches at values below 1%. Despite these challenges, the current demonstration serves as a foundational step, and we will elaborate on these aspects in the subsequent discussion.

5.4.1 Electronic Calibration

As explained in Section 3.1.1, our experimental procedure involves sending a sine wave at a frequency corresponding to twice the HOM spacing frequency to the EOL. With the cavity locked on the fundamental mode, we acquire the RF signal from the photodiode in reflection. This signal contains the beating between the LG_{01} sidebands and the LG_{01} carrier. Since the modulation frequency for the EOL corresponds to twice the HOMs of the cavity, the sidebands are not equally reflected, and therefore we obtain an error signal sensitive to both mismatches degrees of freedom. We then send this signal to the I/Q demodulation chain to obtain the demodulated quadratures, denoted as Ch_1 and Ch_2, from which we extract the information regarding the mismatch parameters. In Figure 5.16, the demodulation chain configuration is illustrated, comprising two power splitters (at 0° and 90°), two mixers, and two low-pass filters. Both the signal to the EOL and the LO for the demodulation are generated by the DDS to ensure precise frequency synchronization.

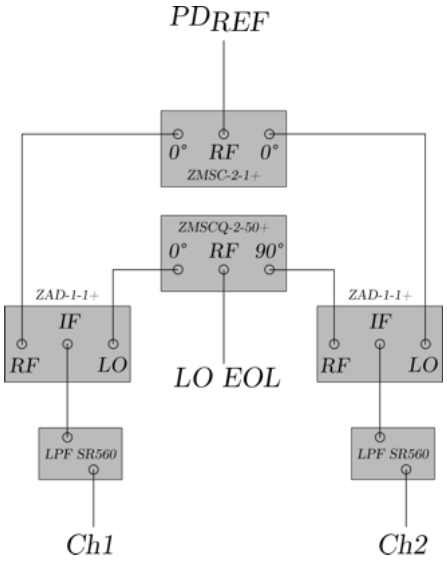

Figure 5.16: Scheme of the demodulation chain. The signal from the PD in reflection is split through a 0° power splitter (Mini-Circuit ZSMC-2-1+), while the LO for the demodulation is split with a 90° power splitter (Mini-Circuit ZSMCQ-2-50+) to obtain the I and Q signals. Each split output is sent then to a mixer (Mini-Circuit ZAD-1-1+), to mix the EOL signal once with the 0° LO and once with the 90° LO. The mixed signals (IF) are then low-passed (SRS SR560) to obtain the so-called Ch_1 and Ch_2

The DDS sine wave achieves a maximum amplitude of 7 dBm. The mixer is categorized as a level 7 mixer which means it has a drive power requirement of 7 dBm. However, due to the power splitting of the DDS signal, a 4 dBm signal is obtained. It's worth noting that the Mini-Circuit mixers can operate within a LO power range of ±3 dB from the 7 dBm value. We verified that the mixer's behavior remained in fact consistent when using both an LO of 7 dBm and an LO of 4 dBm, as shown in Figure 5.17. Within the RF input signal, there is a linear region observed between -30dBm and -7dBm, while the signal generated from the LG_{01} beating has a power range between -40dBm and -20dBm. Despite a portion of our signal extending beyond the linear range, the behavior of the mixers does not deviate significantly.

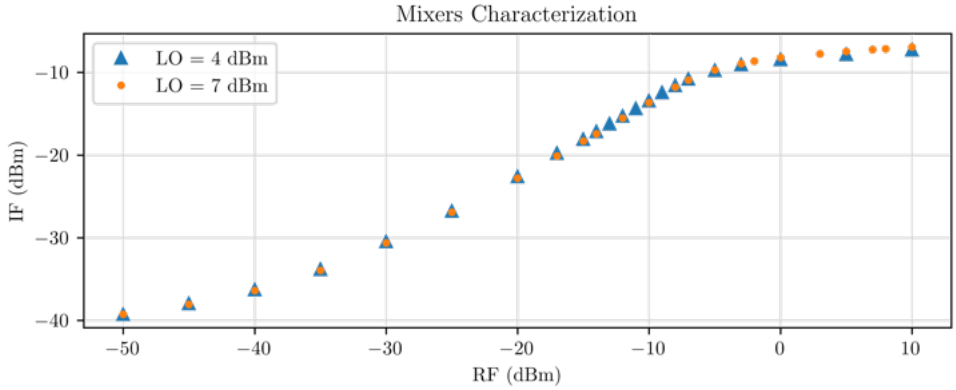

Figure 5.17: Characterization of the mixer ZAD-1-1+ with LO 7dBm (blue) and 4dBm (orange). The plot shows the output of the mixer (IF) as a function of the input signal at 30MHz for two values of the local oscillator amplitude. The behavior is consistent in the two cases, and almost linear in the input signal range between -30dBm and -7dBm.

As we have seen in chapter 3.1.3, the channels are a linear combination of the mismatch parameters, specifically they are derived through a rotation and a rescaling as:

$$\begin{pmatrix} Ch_1 \\ Ch_2 \end{pmatrix} = \begin{pmatrix} c_1 & 0 \\ 0 & c_2 \end{pmatrix} \begin{pmatrix} \cos(\theta) & -\sin(\theta) \\ \sin(\theta+\delta\phi) & \cos(\theta+\delta\phi) \end{pmatrix} \begin{pmatrix} \beta \\ \gamma \end{pmatrix} \tag{5.2}$$

In the expression, c_1 and c_2 represent the gains of the two demodulation chains. The variable θ is made up of an electronic phase, which depends on the demodulation chain, and two optic phases associated with the EOL's position relative to the cavity and the beam's characteristics inside the EOL. Furthermore, the term $\delta\phi$ takes into account potential variations in the demodulation phases between the two LOs. This problem could arise in case of an incorrect splitting of the 90° splitter.

In order to calibrate the gains and the relative angle between the LOs, we shifted the LO frequency for demodulation by approximately $0.2Hz$. Consequently, the phase rotates with this same frequency and we are able to extract the information we need. Suppose we have a signal $y(t) = A\sin\omega t$ which is being demodulated with $LO_1(t) = c_1\sin(\omega' t)$ and $LO_2(t) = c_2\cos(\omega' t)$, then we obtain two signals with the form:

$$d_1(t) = Ac_1\cos((\omega'-\omega)t) \qquad d_2(t) = Ac_2\sin((\omega'-\omega)t) \tag{5.3}$$

where we omit the part at the sum of the frequencies by supposing that the difference between them is small enough that we can low-pass filter the demodulated signals. By measuring the amplitude ratio and the phase difference between these two signals, we are able to calibrate the gain and also confirm that the 90° splitter works as intended. This is shown in Figure 5.18 for two different values of mismatch. In the upper plot, we observe signals corresponding to a mismatch of approximately 0.14, whereas in the lower plot, the mismatch is around 0.07. As expected, changing the mismatch value directly influences the circle's radius. In this instance, the bottom circle exhibits a radius approximately half that of the top circle, consistent with our expectations. The parameters of the two sinusoidal fits for both mismatch values are specified in tables 5.19 and 5.20. In particular, the phase difference $\phi_1 - \phi_2$ between the two sinusoidal fits is $\simeq 90°$ for both mismatch values, demonstrating that the 90° splitters work as intended, which means we can set $\delta\phi = 0$. Moreover, we have a relative gain between the channels of about $\frac{c_2}{c_1} = 1.05$.

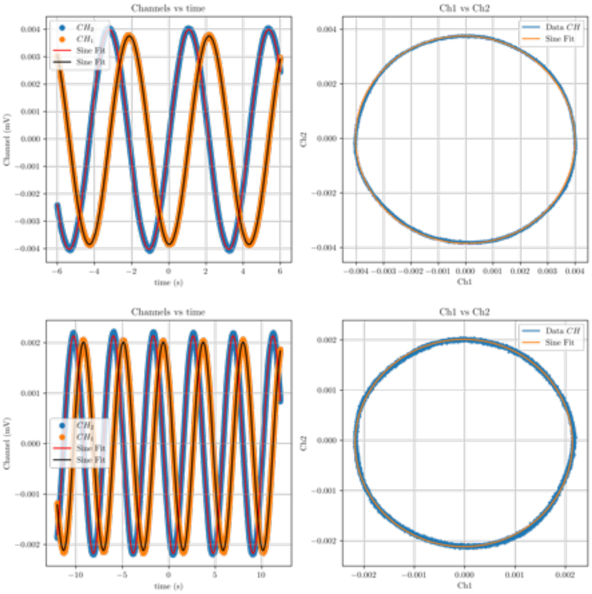

Figure 5.18: Sinusoidal behavior of the channels when the LO has a 0.2Hz difference in the frequency with respect to the modulation frequency. The top graph illustrates the data acquired with a total mismatch of 0.14, while the lower part displays the data with a mismatch of 0.07. The amplitudes of the sinusoidal signals in the former case are double those in the latter, confirming that the channels contain the mismatch information.

$$MM = 0.14$$

	Ch_1	Ch_2
Amplitude V	$3.8 \times 10^{-3} mV$	$4 \times 10^{-3} mV$
Frequency f	$0.23 Hz$	$0.23 Hz$
Phase ϕ	$89.1°$	$-1.7°$
Offset q	$-1.8 \times 10^{-5} mV$	$-4.7 \times 10^{-5} mV$

Table 5.19: Parameters of the sinusoidal fit of the channels obtained when the frequency of the LO has a small difference with respect to the frequency of modulation and the mismatch is $MM = 0.14$.

$$MM = 0.07$$

	Ch_1	Ch_2
Amplitude V	$2.06 \times 10^{-3} mV$	$2.16 \times 10^{-3} mV$
Frequency f	$0.23 Hz$	$0.23 Hz$
Phase ϕ	$-39.8°$	$50.2°$
Offset q	$-2 \times 10^{-5} mV$	$-5.2 \times 10^{-5} mV$

Table 5.20: Parameters of the sinusoidal fit of the channels obtained when the frequency of the LO has a small difference with respect to the frequency of modulation and the mismatch is $MM = 0.07$.

5.4.2 Channels Decoupling

To validate the technique, we measured the mismatch through the cavity scan and simultaneously we acquired the values of Ch_1 and Ch_2 for different positions of the lenses of the mode-matching telescope. In particular, the channels are filtered at 0.03Hz to retrieve only the DC part of the I/Q demodulation, and acquired for about 30 seconds with an oscilloscope to calculate the average and the standard deviation.

As we have seen in the previous section, the channels contain the signal from the EOL modulation, therefore the sum of their squared values needs to be proportional to the measured mismatch. This is shown in Figure 5.21, however, the signal tends to behave more quadratically since for mismatch over 10% we start losing the expected linear behavior.

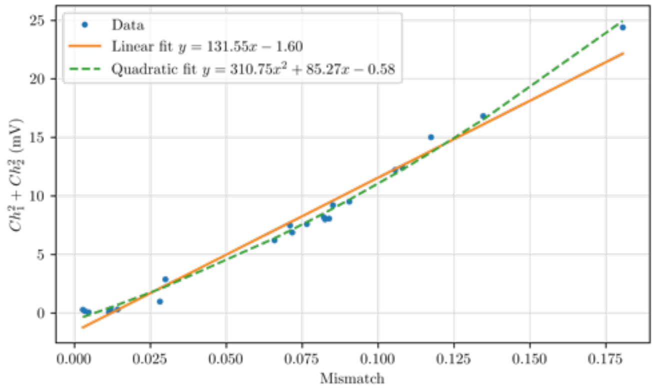

Figure 5.21: Linearity between $Ch_1^2 + Ch_2^2$ and the experimental mismatch calculated as the ratio between the amplitudes of the LG_{01} and the $LG00$ peaks through the cavity scan. The quadratic behavior can be explained loss of linearity above 10% of mismatch.

Despite the quadratic behavior, it is clear that the channels contain the mismatch information; we must now prove that we can decouple the γ and β contributions from the measurement of Ch_1 and Ch_2.

To do this, we opted to study the channel signals by adjusting the telescope lenses in two ways: along the isolines defined by β and γ, as determined through the mismatch fit detailed in Section 5.2, and along arbitrary values of mismatch obtained by moving the lenses of the telescope by regular steps without attempting to follow the specific pattern of the isolines. From the first set of measurements, it is easy to obtain the overall rotation angle between the Ch_1/Ch_2 and β/γ axis that makes them two parallel; from the second measurements, we can obtain a more general check of the reconstructed values of β and γ starting from Ch_1 and Ch_2.

We acquired the channel values by moving the lenses in the positions where $\gamma = 0.265$ and $\beta = -0.13$, as shown in Figure 5.22. We decided to work on those isolines in order to maximize the signals since for higher values of mismatch we have a greater effect. At the same time, we wanted to acquire the data where the linear assumptions on the model are valid. To determine the optimal rotation for decoupling the channels, we plotted Ch_1 versus Ch_2 for each isoline

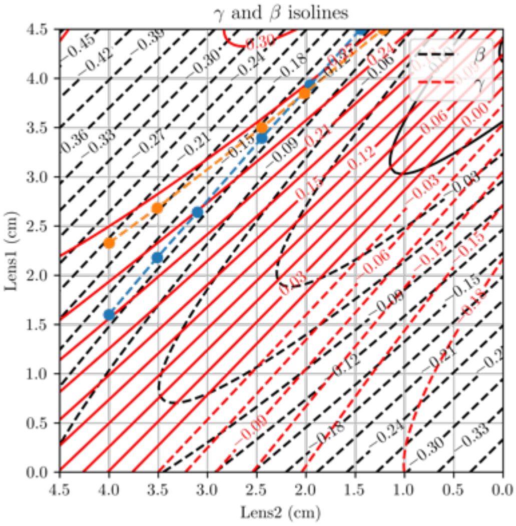

Figure 5.22: Map of the γ and β isolines at different positions of the lenses. The points in blue and orange identify the positions of the lenses where the isolines are $\gamma = 0.265$ (orange) and $\beta = -0.13$ (blue).

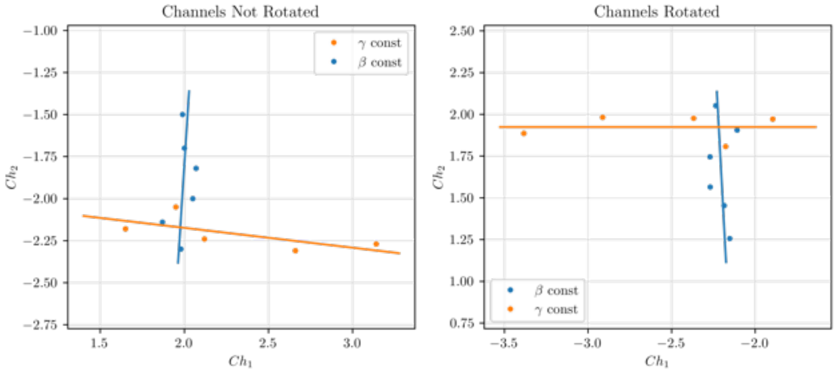

Figure 5.23: On the left Ch_1 vs Ch_2 not rotated, while on the right the channels rotated of θ. The lines correspond to the linear fits. The relative angle between the lines is 87° ± 1°.

as depicted in Figure 5.23 and performed linear fits for both datasets. The two linear fits are almost perfectly orthogonal, as expected, with an angle between them measuring $\phi = (87° \pm 1°)$. To align the channels with the space of the mismatch parameters, we need to apply a rotation of 173° as shown in the right plot of Figure 5.23. The scaling factors between the channels and the mismatch parameters were found by comparing Ch_1 and Ch_2 with the theoretical values of γ and β, obtained through the fitted contour map, and minimizing the residuals between the experimental data and the theoretical data. The overall transformation we apply has the form:

$$\begin{pmatrix} \beta^* \\ \gamma^* \end{pmatrix} = \begin{pmatrix} \cos(\theta) & \sin(\theta) \\ -\sin(\theta) & \cos(\theta) \end{pmatrix} \begin{pmatrix} c_1 & 0 \\ 0 & c_2 \end{pmatrix} \begin{pmatrix} Ch_1 \\ Ch_2 \end{pmatrix} \tag{5.4}$$

and since $c_2/c_1 = 1.05$, we can use the same angle found to align the channels on the isolines on the γ-β space, that is $\theta = 173°$. Figure 5.24 shows the data as a function of the experimental mismatch. In particular, the top plot shows the raw values of the channels without any transformation. In the center and bottom plots, we present the transformed data γ^* and β^* and the theoretical values of γ and β. The behavior of γ^* and β^* aligns with the expected theoretical behavior having one transformed channel constant at β constant while the other changes and vice versa at γ constant. However, we see a discrepancy in the values of the transformed data with respect to the theoretical ones.

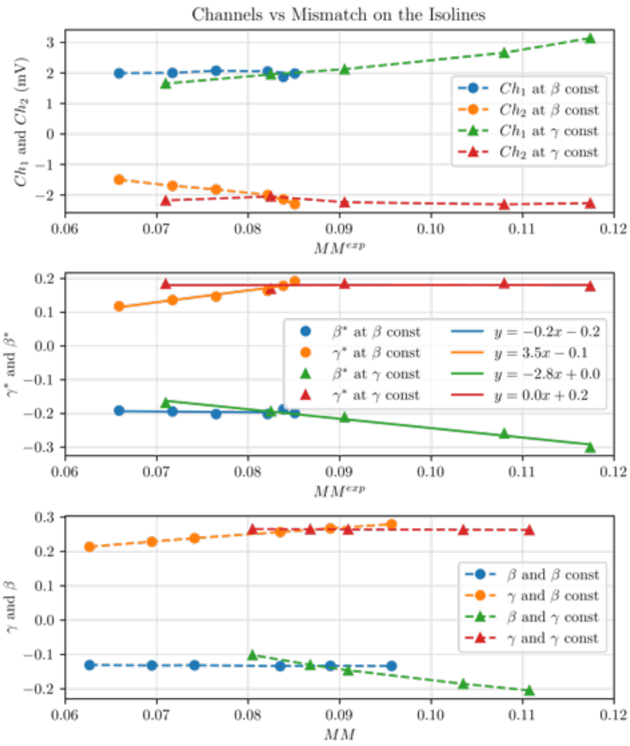

Figure 5.24: Channels vs Mismatch on the isolines $\gamma = 0.265$ and $\beta = -0.13$. Top: Channels not rotated vs experimental Mismatch. Center: Channels rotated by $\theta = 173°$ vs experimental mismatch. Bottom: Theoretical values of γ and β vs theoretical mismatch.

This problem is also shown when using the same parameters ($\theta = 173°$ and $c_1/c_2 = 1.05$) to obtain β^* and γ^* from Ch_1 and Ch_2 at arbitrary mismatch values; this is shown in Figure 5.25 where measured values are depicted in blue, while theoretical data are in red. Specifically, the top left graph illustrates β^* and γ^* and β vs γ. On the right, the square sum of the channels $\beta^{*2} + \gamma^{*2}$ is plotted against the experimental mismatch. The bottom section includes β^* vs experimental mismatch alongside β vs theoretical mismatch, and the same goes for γ^* and γ. As it is possible to see, while the general behavior seems to be well reconstructed, we don't have a good quantitative agreement between experimental and theoretical values, especially for larger values of both parameters.

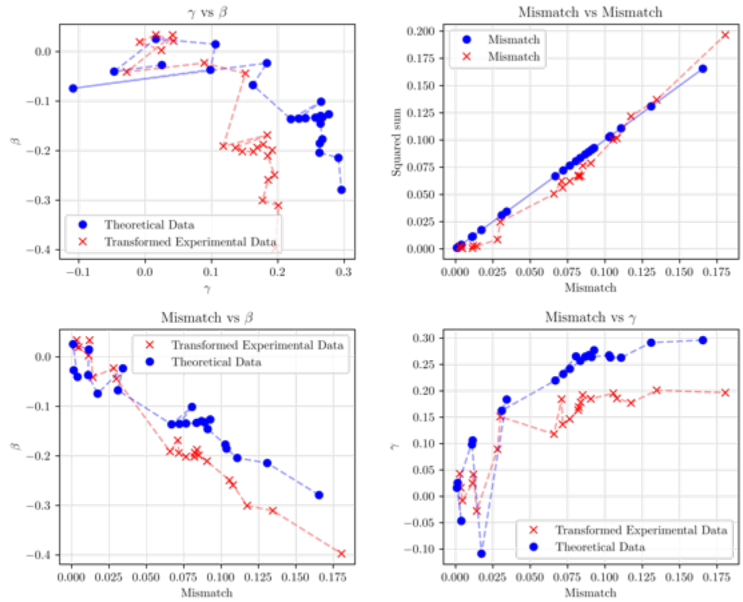

Figure 5.25: These plots consider the transformation of the channels using parameters obtained from the calibration of the demodulation chain. Top left: Ch_1 vs Ch_2 (transformed) in red and β vs γ in blue. Top right: $Ch_1^2 + Ch_2^2$ (transformed) vs Mismatch in red, and Mismatch vs Mismatch in blue. Bottom left: Ch_1 (transformed) vs experimental mismatch in red, β vs theoretical mismatch in blue. Bottom right: Ch_2 (transformed) vs experimental mismatch in red, γ vs theoretical mismatch in blue.

To address this issue, we can introduce more degrees of freedom in our analysis. This involves not constraining the scaling factors and therefore also the angle. Fitting all three parameters yields a better alignment between experimental measurements and theoretical predictions, as shown in Figure 5.27. However, we lose part of the orthogonality between the isolines obtaining an angle between the isolines of about 80°. Moreover, the resulting c_1/c_2 ratio is 1.8, as indicated in table 5.26, significantly deviating from the calibration-derived ratio of 1.05.

	θ	c_1	c_2	ϕ
With calibration	173°	0.088	0.092	87°
Without calibration	181°	0.068	0.122	80°

Table 5.26: Parameters of rotation and rescaling with and without using the calibration of the demodulation chain.

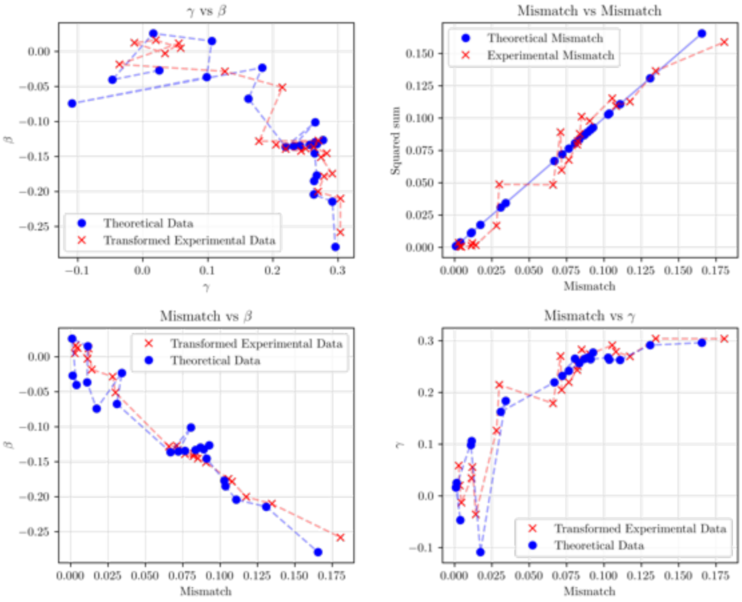

Figure 5.27: These plots consider the transformation of the channels using parameters obtained without the calibration of the demodulation chain. Top left: Ch_1 vs Ch_2 (transformed) in red and β vs γ in blue. Top right: $Ch_1^2 + Ch_2^2$ (transformed) vs Mismatch in red, and Mismatch vs Mismatch in blue. Bottom left: Ch_1 (transformed) vs experimental mismatch in red, β vs theoretical mismatch in blue. Bottom right: Ch_2 (transformed) vs experimental mismatch in red, γ vs theoretical mismatch in blue.

We hypothesized that this disparity may stem from an imbalance between the two low-pass filters when we change the cut-off frequency: when acquiring the data with the shift of 0.2Hz in the LO frequency, we set the filter cut-off at 0.3Hz, but when we acquire the channels to transform them in γ and β, the cut-off is at 0.03Hz in order to take only the DC component of the demodulation. However, we verified the behavior of the filters, obtaining consistent results between the two cut-off frequency settings. To do this test, we demodulated a clean signal at frequency $f_{LO} + 0.02Hz$ and we acquired the demodulated data with a cut-off on the low-pass filter of $0.3Hz$ and $0.03Hz$. The demodulated signals are shown in Figure 5.28. The amplitude at $0.03Hz$ is smaller than the one at $0.3Hz$, as expected. However, the ratio $r = c_2/c_1$ between the amplitudes of Ch_2 and Ch_1 is nearly the same, being $r_{0.03Hz} = 1.05$ and $r_{0.3Hz} = 1.03$.

Another possible explanation is that, due to our calibration procedure, our theoretical map of γ and β could still be inaccurate. Using the fitting method described in the previous section, where the waist is fitted at the input instead of the output, may offer a potential solution to this issue. However, we do not have an easy way of checking this, since our calibration and our independent controls are all based on the overall mismatch, and not on β and γ, which we haven't measured independently.

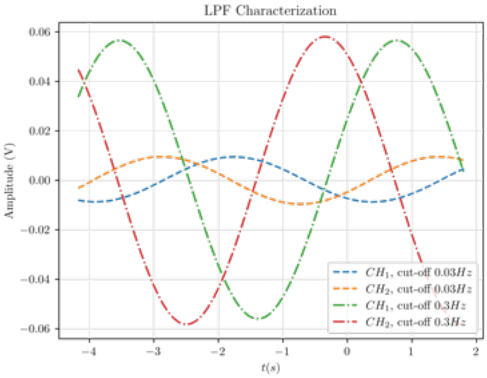

Figure 5.28: Characterization of the low-pass filters gain between the cut-off of $0.03Hz$ (blue and orange curves) and $0.3Hz$ (red and green curves). The ratio between the amplitudes in both cases is approximately equal, having $r_{0.03Hz} = 1.05$ and $r_{0.3Hz} = 1.03$

While our RF sensing technique successfully demonstrated the presence of mismatch parameters in the acquired signals and showcased the ability to decouple signals into corresponding β and γ values along isolines, challenges persist in determining the scaling factor for an accurate translation of signals into mismatch parameters. Even though our results are not entirely conclusive, we proved to have developed a functional prototype of an electro-optical lens and performed a successful proof of principle of the technique. By modulating the beam, this adaptive lens allows us to extract information about the mismatch, using only the single element photodiode already present for the PDH locking, pointing towards promising possibilities for further improvement of an innovative and relatively straightforward method implementing closed loop mode mismatch in optical cavities.

Chapter 6

Conclusions

Gravitational wave detectors face a critical sensitivity limitation imposed by quantum noise. To address this challenge, a filter cavity to generate squeezing broadband is employed. While this technique proves effective in mitigating quantum noise, potential losses can degrade the squeezing level. One of the main optical losses is mode mismatch, which refers to the discrepancy between the waist size and position of the input beam and the resonant mode supported by an optical cavity. Currently, there are a few techniques proposed for sensing mode mismatch, such as heterodyne detection with bullseye photodiodes, the generation of sidebands through an optical cavity, and the use of a mode converter and quadrant photodiodes. In this thesis, we demonstrated the working principle of an alternative online sensing method based on the RF higher-order modulation using an electro-optical lens (EOL) to generate sidebands on the Laguerre-Gauss first-order mode, similar to the already present technique for the alignment sensing through RF jitter modulation [48]. One of the strengths of this technique is the possibility to use the same sensing hardware already present, without adding any photodiode or gouy-phase telescope. The price of this is the addition of a modulation device, which however can serve two cavities in series at once.

The basic design of the EOL is composed of a lithium niobate crystal sandwiched with suitable copper electrodes in order to exploit the electro-optical effect to create the lens behavior and generate sidebands on the first Laguerre-Gauss mode, LG_{01}, which arises from the mismatch between a beam and an optical cavity. In particular, we studied, both with simulations and experimentally, two different prototypes of EOL. One, $\mathrm{EOL_{PD}}$ acts as a spherical lens, while the other, $\mathrm{EOL_{FL}}$, behaves as a particular astigmatic lens, with opposite focal length on the two transversal axes, and needs to be paired with a mode-converter telescope to retrieve the spherical behavior. We proved with simulation and verified experimentally that, despite the slightly more complex design due to the presence of the telescope, the $\mathrm{EOL_{FL}}$ yields a much bigger effect for the same applied voltage, and is much more tolerant with respect to deviations from the ideal construction parameters.

By testing the two prototypes through a slow lock-in measurement, we found that both were modulating the LG_{01} amplitude, however while the modulation of the $\mathrm{EOL_{FL}}$ is in accordance with simulations, the modulation due to the $\mathrm{EOL_{PD}}$ was 2 order of magnitude greater than the one simulated. One possible explanation for this discrepancy could be that the $\mathrm{EOL_{PD}}$ does not behave as a spherical lens as designed, and therefore it is injecting the wrong mode content of the sidebands. This problem could be solved by using a wavefront sensor to study the effect of the $\mathrm{EOL_{PD}}$ and adjust the geometric parameters.

Encouraged by the promising initial outcomes of the $\mathrm{EOL_{FL}}$, we used it to implement the RF mode-matching technique. To decouple the two error signals (Ch_1, Ch_2) obtained after the I/Q demodulation, into the γ and β parameters we decided to move the mode-matching telescope, placed before the cavity, in two specific ways: by following the positions that identify the isolines of γ and β, and by moving on arbitrary values of mismatch. From the data collected, we were able to obtain a signal monotonic with the overall mismatch (and linear with it for small values), and we successfully found the rotation angle to decouple the signals to obtain two errors proportional to the mismatch parameters. However, we were not able to obtain the correct scaling factors to translate completely the channel values in the corresponding mismatch parameters.

We envision several improvements to both the demonstration setup to the technique itself to help demonstrate its suitability for high-precision mode-mismatch sensing. For instance, incorporating a mode cleaner at the beginning of the setup to obtain a pure fundamental mode and utilizing digital electronics for the demodulation process, can significantly enhance the precision and reliability of the technique. It is also crucial to accurately characterize the contour plot of the mode-matching telescope. This precision is necessary to closely approximate the γ and β spaces to their actual values, and therefore to be able to precisely characterize the channel values. Furthermore, using a highly sensitive wavefront sensor to characterize the wavefront distortion of both EOL prototypes would certainly help highlight deviations from the intended effect that can contribute to explain the current limitations of the technique; with this information, the design of the EOL could be further improved, ultimately improving the precision and reliability of the RFHM technique.

Although some work is still needed before its application real-world gravitational wave detectors and other high-precision experiments, we have demonstrated the potential and effectiveness of a new technique for mode-mismatch sensing characterized by particularly modest requirements for the sensing hardware. We hope this technique will prove to be an useful tool to be applied in scenarios in which other available technique may be harder to implement.

Appendix A

Pound-Drever-Hall Stabilisation Technique

The Pound-Drever-Hall (PDH) locking technique stabilizes a laser's frequency by utilizing the sidebands produced by an EOM and measuring the laser's frequency against a reference cavity. It was named after Robert V. Pound, Ronald Drever, and John L. Hall, and it was first described by Drever et al. in 1983 [56].

Suppose we want to stabilize a laser frequency and we have an optical cavity with a known FSR and a given linewidth. Recalling what we have seen in the previous chapter, the cavity acts as a filter, allowing only specific frequencies to resonate within it. In general, the beam reflected by a cavity is composed of the promptly reflected beam, which never enters inside the cavity, and the leakage beam, which is part of the resonant field which escapes from the cavity. When the laser's frequency is exactly a multiple of the FSR, then the two components of the reflected beam are 180° out of phase and they canceled out. However, if there is a slightly change from the resonance frequency, these components partially constructively interfere.

Suppose we have a lossless Fabry-Pérot cavity with reflectivity of the mirrors r, for simplicity. As we have seen in section 2.2.2, we can write the complex reflection coefficient $F_{lp}(\omega)$ of the cavity of a mode LG_{lp} is:

$$F_{lp}(\omega) = \frac{E_{ref}(t)}{E_{in}(t)} = \frac{r(e^{-i\left(\frac{\omega}{FSR}-(N+1)\chi_{cav}\right)}-1)}{1-r^2 e^{-i\left(\frac{\omega}{FSR}-(N+1)\chi_{cav}\right)}} \tag{A.1}$$

where $N = 2p + |l|$. For the purposes of the PDH discussion we will alway refer to the fundamental mode, hence we will write $F(\omega) = F_{00}(\omega)$. The plots of the intensity and phase of the complex reflection coefficient for the fundamental mode are shown Figure A.1. When the laser's frequency is far from the resonance condition, all the incident light is reflected from the cavity and the phase shift is either ±180°, depending on whether the laser's frequency is below or above the resonance frequency. As we approach the resonance frequency, a portion of the incident light begins to form a standing wave inside the cavity, causing the phase shift to tend towards ±90°. When the laser's frequency precisely matches a multiple of the FSR, the intensity of the reflected light drops to zero, and the phase shift reaches ±90°. While the reflected intensity indicates our proximity to resonance, it alone cannot specify whether we are below or above resonance since it is symmetric around the minimum. In contrast, the phase is anti-symmetric and contains the information we need. To extract this information, we introduce frequency (or phase) modulation to the laser beam and observe how the reflected intensity reacts. Modulating the laser's frequency generates sidebands in the beam. By choosing a modulation frequency that is significantly different from the cavity's resonance, the sidebands are always reflected with a reflection coefficient close to 1 and largely independent on their exact position. As there is a well-defined phase relationship between the resonating main signal (carrier) and the sidebands, any deviation of the carrier from resonance results in a beatnote between the sidebands and the reflected carrier. This beatnote provides the information needed to determine our position relative to resonance, ultimately yielding an error signal.

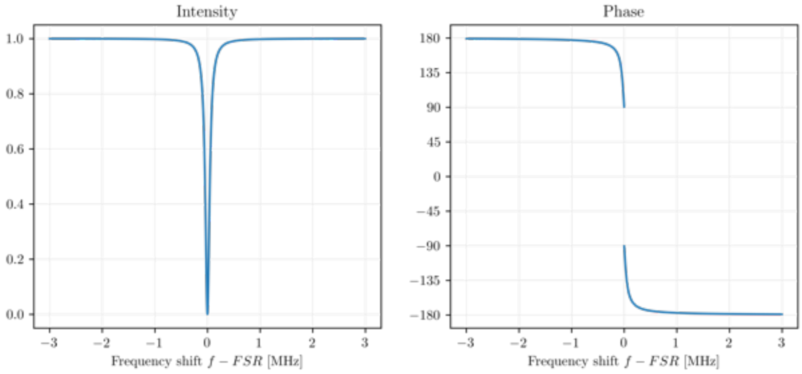

Figure A.1: Intensity and phase of the complex reflection coefficient of the cavity as a function of the frequency shift from the FSR value. When the beam resonates inside the cavity the intensity goes to zero and, consequently, there is a discontinuity in the phase.

In Figure A.2 the basic scheme for the PDH locking technique. A laser of frequency ω pass through an EOM which is controlled by an RF generator, acting as a local oscillator (LO), to introduce sidebands at frequency $\omega \pm \Omega$ onto the laser beam. Then it goes inside an optical cavity: the sidebands and part of the carrier slightly off-resonance are reflected and the beatnote is acquired by a photodetector (PD). The PD's output is compared with the local oscillator's signal using a mixer. Subsequently, the mixer's output undergoes low-pass filtering and is fed into a Proportional-Integral-Derivative (PID) controller to maintain laser frequency stability. Let us see now how to obtain the error signal. Taking equation (3.64), at first order the incident beam can be written as:

$$u_{inc}(x,t) = u_0(x)[J_0(m)e^{i\omega t} + J_1(m)e^{i(\omega-\Omega)t} - J_1(m)e^{i(\omega+\Omega)t}] \tag{A.2}$$

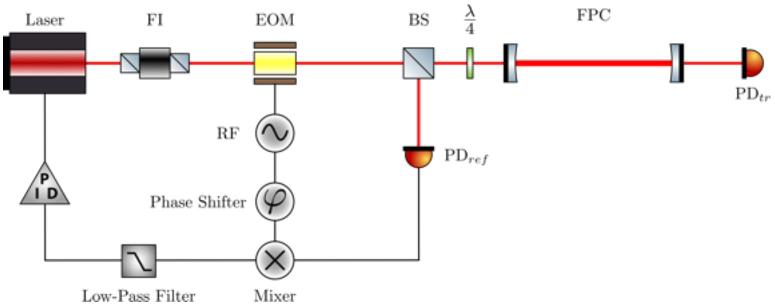

Figure A.2: Optical setup for Pound-Drever-Hall (PDH) laser locking to the cavity. The Faraday Isolator (FI) is needed to prevent the reflected beam from going back into the laser source. The beam splitter (BS) and the quarte wave plate (QWP, $\lambda/4$) serve as an optical isolator in the case of a linear cavity to send the beam to the PD in reflection.

where m is the modulation depth of the EOM. Taking into account the complex reflection coefficient of equation (A.1), the reflected field will be the convolution of the incident field with the complex reflection coefficient of the cavity. In the Fourier transform space, using the convolution theorem, this reduces simply to the product between the transformed components:

$$u_{ref} = u_0(x)[F(\omega)J_0(m)e^{i\omega t} + F(\omega+\Omega)J_1(m)e^{i(\omega-\Omega)t} - F(\omega-\Omega)J_1(m)e^{i(\omega+\Omega)t}] \tag{A.3}$$

Because the PD read the power of the beam, we have to calculate the modulus squared $P_{ref} = |u_{ref}|^2$. We define the total power $P_0 = |u_0(x)|^2$, then we have the carrier power $P_c = J_0(m)^2 P_0$ and the sidebands power $P_s = J_1(m)^2 P_0$, so that $P_c + 2P_s \simeq P_0$. Then we can write:

$$\begin{aligned} P_{ref} =& P_c|F(\omega)|^2 + P_s\Big[|F(\omega+\Omega)|^2 + |F(\omega-\Omega)|^2\Big] \\ &+ 2\sqrt{P_cP_s}\Big[\,\mathrm{Re}\big\{F(\omega)F^*(\omega+\Omega) - F^*(\omega)F(\omega-\Omega)\big\}\cos\Omega t \\ &- \mathrm{Im}\big\{F(\omega)F^*(\omega+\Omega) - F^*(\omega)F(\omega-\Omega)\big\}\sin\Omega t\Big] + (2\Omega\text{terms}) \end{aligned} \tag{A.4}$$

We want to extract the terms oscillating at frequency Ω since they contain the information on the phase of the carrier. Since the modulation frequency Ω is high enough that near resonance the sidebands are completely reflected by the cavity, we can assume that $F(\omega\pm\Omega) \simeq 1$, therefore the cosine term cancels out and only the sine term remain. This signal is then mixed back with the LO and, by adjusting its phase and sending it to a low pass filter to isolate only the DC terms we obtain the signal error ϵ_{PDH}:

$$\epsilon_{PDH} = -\sqrt{P_cP_s}\,\mathrm{Im}\big\{F(\omega)F^*(\omega+\Omega) - F^*(\omega)F(\omega-\Omega)\big\} \tag{A.5}$$

In Figure the plot of the PDH error. Moreover, near the resonance region we can approximate the error. In this region the sidebands are totally reflected, therefore we can write:

$$\mathrm{Im}\big\{F(\omega)F^*(\omega+\Omega) - F^*(\omega)F(\omega-\Omega)\big\} = \mathrm{Im}\big\{F(\omega)\big\} \tag{A.6}$$

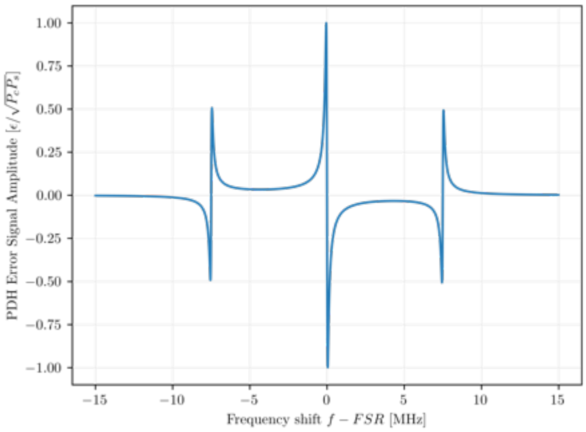

Figure A.3: Normalized PDH error signal vs frequency shift from the FSR. In this plot the modulation frequency Ω is 5% of the FSR.

By expanding at first order in ω the carrier complex reflaction coefficient and recalling that at high finesse we can use equation (2.59), we have:

$$\epsilon_{PDH} = -4\frac{\sqrt{P_c P_s}}{\delta\nu}\delta f \tag{A.7}$$

where δf is the shift of the laser's frequency to the resonance and $\delta\nu$ is the linewidth of the cavity. From this equation we see that near the resonance, where $\delta f \ll \delta\nu$, the behaviour of the error signal is directly proportional to the shift in frequency. The proportionality constant $D = 4\sqrt{P_c P_s}/\delta\nu$ is called the frequency discriminant.

Bibliography

[1] Christian Marchal. Henri poincaré et la physique. *Sciences*, 4(4e), 2004.

[2] Albert Einstein. *Die grundlage der allgemeinen relativitätstheorie*, volume 49. JA Barth, 1922.

[3] Albert Einstein. Über gravitationswellen. *Sitzungsberichte der Königlich Preussischen Akademie der Wissenschaften*, pages 154–167, 1918.

[4] Joseph Weber. Detection and generation of gravitational waves. *Physical Review*, 117(1):306, 1960.

[5] R Weiss. Quarterly progress report of rle. *MIT*, 105:54, 1971.

[6] GE Moss, LR Miller, and RL Forward. Photon-noise-limited laser transducer for gravitational antenna. *Applied Optics*, 10(11):2495–2498, 1971.

[7] Russell A Hulse and Joseph H Taylor. Discovery of a pulsar in a binary system. *The Astrophysical Journal*, 195:L51–L53, 1975.

[8] Benjamin P Abbott, Richard Abbott, TDe Abbott, MR Abernathy, Fausto Acernese, Kendall Ackley, Carl Adams, Thomas Adams, Paolo Addesso, RX Adhikari, et al. Observation of gravitational waves from a binary black hole merger. *Physical review letters*, 116(6):061102, 2016.

[9] Michele Maggiore. *Gravitational waves: Volume 1: Theory and experiments.* OUP Oxford, 2007.

[10] Jolien DE Creighton and Warren G Anderson. *Gravitational-wave physics and astronomy: An introduction to theory, experiment and data analysis.* John Wiley & Sons, 2012.

[11] Magdalena Sieniawska and Michał Bejger. Continuous gravitational waves from neutron stars: current status and prospects. *Universe*, 5(11):217, 2019.

[12] Stuart L Shapiro and Saul A Teukolsky. *Black holes, white dwarfs, and neutron stars: The physics of compact objects.* John Wiley & Sons, 2008.

[13] Vincent Roma, Jade Powell, Ik Siong Heng, and Raymond Frey. Astrophysics with core-collapse supernova gravitational wave signals in the next generation of gravitational wave detectors. *Physical Review D*, 99(6):063018, 2019.

[14] Benjamin P Abbott, Richard Abbott, TD Abbott, F Acernese, K Ackley, C Adams, T Adams, P Addesso, Rana X Adhikari, Vaishali B Adya, et al. Gw170814: a three-detector observation of gravitational waves from a binary black hole coalescence. *Physical review letters*, 119(14):141101, 2017.

[15] Benjamin P Abbott, Rich Abbott, TDea Abbott, Fausto Acernese, Kendall Ackley, Carl Adams, Thomas Adams, Paolo Addesso, RX Adhikari, Vaishali B Adya, et al. Gw170817: observation of gravitational waves from a binary neutron star inspiral. *Physical review letters*, 119(16):161101, 2017.

[16] Stefan Hild, Hartmut Grote, Jerome Degallaix, Szczepan Chelkowski, Karsten Danzmann, Andreas Freise, Martin Hewitson, J Hough, Harald Lück, M Prijatelj, et al. Dc-readout of a signal-recycled gravitational wave detector. *Classical and Quantum Gravity*, 26(5):055012, 2009.

[17] VirgoCollaboration. Advanced virgo plus phase i - design report. *Virgo-Technical Documentation System, Report No. VIR-0596A-19, 2019.*

[18] Massimo Bassan et al. Advanced interferometers and the search for gravitational waves. *Astrophysics and Space Science Library*, 404:275–290, 2014.

[19] Jun Mizuno, Kenneth A Strain, PG Nelson, JM Chen, Roland Schilling, Albrecht Rüdiger, Walter Winkler, and Karsten Danzmann. Resonant sideband extraction: a new configuration for interferometric gravitational wave detectors. *Physics Letters A*, 175(5):273–276, 1993.

[20] Peter R Saulson. Terrestrial gravitational noise on a gravitational wave antenna. *Physical Review D*, 30(4):732, 1984.

[21] Fausto Acernese, P Amico, N Arnaud, D Babusci, R Barillé, Fabrizio Barone, L Barsotti, M Barsuglia, F Beauville, MA Bizouard, et al. Properties of seismic noise at the virgo site. *Classical and Quantum Gravity*, 21(5):S433, 2004.

[22] Jan Harms, Luca Naticchioni, Enrico Calloni, Rosario De Rosa, Fulvio Ricci, and Domenico D'Urso. A lower limit for newtonian-noise models of the einstein telescope. *The European Physical Journal Plus*, 137(6):687, 2022.

[23] Herbert B Callen and Theodore A Welton. Irreversibility and generalized noise. *Physical Review*, 83(1):34, 1951.

[24] VB Braginsky, VP Mitrofanov, and KV Tokmakov. Energy dissipation in the pendulum mode of the test mass suspension of a gravitational wave antenna. *Physics Letters A*, 218(3-6):164–166, 1996.

[25] Yu Levin. Internal thermal noise in the ligo test masses: A direct approach. *Physical Review D*, 57(2):659, 1998.

[26] Carlton M Caves. Quantum-mechanical radiation-pressure fluctuations in an interferometer. *Physical Review Letters*, 45(2):75, 1980.

[27] Carlton M Caves. Quantum-mechanical noise in an interferometer. *Physical Review D*, 23(8):1693, 1981.

[28] F. Sorrentino and J.-P. Zendri. *Squeezing and QM Techniques in GW Interferometers.* Springer Nature, 2020.

[29] M Mehmet and H Vahlbruch. High-efficiency squeezed light generation for gravitational wave detectors. *Classical and Quantum Gravity*, 36(1):015014, 2018.

[30] H Jeff Kimble, Yuri Levin, Andrey B Matsko, Kip S Thorne, and Sergey P Vyatchanin. Conversion of conventional gravitational-wave interferometers into quantum nondemolition interferometers by modifying their input and/or output optics. *Physical Review D*, 65(2):022002, 2001.

[31] Simon Chelkowski. Squeezed light and laser interferometric gravitational wave detectors. 2007.

[32] Hans-A Bachor and Timothy C Ralph. *A guide to experiments in quantum optics.* John Wiley & Sons, 2019.

[33] L McCuller, SE Dwyer, AC Green, Haocun Yu, K Kuns, L Barsotti, CD Blair, DD Brown, A Effler, M Evans, et al. Ligo's quantum response to squeezed states. *Physical Review D*, 104(6):062006, 2021.

[34] Guido Mueller, Qi-ze Shu, Rana Adhikari, DB Tanner, David Reitze, Daniel Sigg, Nergis Mavalvala, and Jordan Camp. Determination and optimization of mode matching into optical cavities by heterodyne detection. *Optics letters*, 25(4):266–268, 2000.

[35] Alexei A Ciobanu, Daniel David Brown, Peter J Veitch, and David J Ottaway. Mode matching error signals using radio-frequency beam shape modulation. *Applied Optics*, 59(31):9884–9895, 2020.

[36] Fabian Magana-Sandoval, Thomas Vo, Daniel Vander-Hyde, JR Sanders, and Stefan W Ballmer. Sensing optical cavity mismatch with a mode-converter and quadrant photodiode. *Physical Review D*, 100(10):102001, 2019.

[37] Marco W Beijersbergen, Les Allen, HELO Van der Veen, and JP Woerdman. Astigmatic laser mode converters and transfer of orbital angular momentum. *Optics Communications*, 96(1-3):123–132, 1993.

[38] Anthony E Siegman. *Lasers*. University science books, 1986.

[39] Herwig Kogelnik and Tingye Li. Laser beams and resonators. *Applied optics*, 5(10):1550–1567, 1966.

[40] Anthony A Tovar and Lee W Casperson. Generalized sylvester theorems for periodic applications in matrix optics. *JOSA A*, 12(3):578–590, 1995.

[41] M Fatih Erden and Haldun M Ozaktas. Accumulated gouy phase shift in gaussian beam propagation through first-order optical systems. *JOSA A*, 14(9):2190–2194, 1997.

[42] Koji Arai. On the accumulated round-trip gouy phase shift for a general optical cavity. *LIGO Technical Note*, 1300189:1–11, 2013.

[43] Haoyu Wang, Miguel Dovale-Álvarez, Christopher Collins, Daniel David Brown, Mengyao Wang, Conor M Mow-Lowry, Sen Han, and Andreas Freise. Feasibility of near-unstable cavities for future gravitational wave detectors. *Physical Review D*, 97(2):022001, 2018.

[44] M Möller, LM Hoffer, GL Lippi, T Ackemann, A Gahl, and W Lange. Fabry-pérot and ring cavity configurations and transverse optical patterns. *Journal of Modern Optics*, 45(9):1913–1926, 1998.

[45] Dana Z Anderson. Alignment of resonant optical cavities. *Applied Optics*, 23(17):2944–2949, 1984.

[46] Nicolò Pisani. Sviluppo di una lente elettro-ottica per misure di accoppiamento laser in cavità a radiofrequenza.

[47] Giacomo Ciani, Matteo Carlassara, and Marco Bazzan. A novel technique for laser mode-matching in gravitational wave detectors.

[48] P Fulda, D Voss, C Mueller, LF Ortega, G Ciani, G Mueller, and DB Tanner. Alignment sensing for optical cavities using radio-frequency jitter modulation. *Applied Optics*, 56(13):3879–3888, 2017.

[49] F. Pockels. *Abhandl. Gesell. Wiss. Gottingen*, 39(1), 1984.

[50] John Kerr. Xl. a new relation between electricity and light: Dielectrified media birefringent. *The London, Edinburgh, and Dublin Philosophical Magazine and Journal of Science*, 50(332):337–348, 1875.

[51] Amnon Yariv and Pochi Yeh. *Photonics: optical electronics in modern communications.* Oxford university press, 2007.

[52] RS Weis and TK Gaylord. Lithium niobate: Summary of physical properties and crystal structure. *Applied Physics A*, 37:191–203, 1985.

[53] M. Diaz-Ortiz and P. Fulda. An electro-optic lens concept for mode mismatch sensing. *LVK meeting September*, 2020.

[54] Liu Tao, Paul Fulda, and Anna C Green. Misalignment and mode mismatch error signals for higher-order hermite-gauss modes from two sensing schemes. *Physical Review D*, 108(6):062001, 2023.

[55] Andrea Grimaldi et al. Mode matching sensing in frequency dependent squeezing source for advanced virgo plus. 2023.

[56] Ronald WP Drever, John L Hall, Frank V Kowalski, James Hough, GM Ford, AJ Munley, and H Ward. Laser phase and frequency stabilization using an optical resonator. *Applied Physics B*, 31:97–105, 1983.